João Pedro Estiveira Campos Silva

Controller Implementation For A SSVEP-Based BCI With Resource To Non-Volitional Neurofeedback

Supervisors:

Prof. Dr. Miguel Sá Sousa Castelo Branco (FMUC & ICNAS)
Ernesto Saias Soares, PhD (ICBR Researcher)

Submitted to the University of Coimbra for the degree of
Master in Biomedical Engineering

FACULDADE DE
CIÊNCIAS E TECNOLOGIA
UNIVERSIDADE D
COIMBRA

2019

Work developed in collaboration with:

Resumo

Nesta tese, foram estudados *steady-state visual evoked potentials* (*SSVEP*) com o objectivo de implementar um protótipo de controlo através de uma interface cérebro-computador (*BCI*), de modo a estabilizar oscilações da actividade cerebral induzidas a uma frequência específica e medidas com equipamento encefalográfico (*EEG*), que estão potencialmente relacionadas com activação de sinapses e com dinâmicas de sincronização na região cerebral do córtex visual primário. Com este propósito, foram calculados modelos matemáticos da resposta *SSVEP* cerebral, de modo a realizar simulações de sistemas de controlo e reunir resultados que suportem experiências em humanos. Foi alcançado um controlo marginal das variáveis de potência dos modelos *SSVEP* em diversos valores de referência de controlo para 9 modelos cerebrais, suportando assim o desenvolvimento de um protótipo. A configuração do protótipo é mostrada, funcionando com equipamento de *EEG*. A hipótese biológica diz que a potência instantânea a uma dada frequência está relacionada com a activação de sinapses e sincronização entre elas. Esta hipótese é proposta de acordo com as evidências fornecidas pela literatura consultada. Em futuras experiências é pretendido estabilizar *SSVEPs* em humanos.

Abstract

In this thesis, brain's steady-state visual evoked potentials (SSVEP) were studied to implement a BCI control system prototype to stabilize frequency specific induced oscillations in electroencephalogram (EEG) measured brain signals, which may be related to synapse activation and synchronization dynamics happening in the primary visual cortex. For this purpose, brain SSVEP mathematical models were estimated to perform control system simulations and collect results to support the development of prototype to use in human experiences. Marginal control in specific control reference values was accomplished for 9 human brain SSVEP models, supporting the BCI controller prototype implementation. The prototype setup is demonstrated and tested, functioning with EEG equipment in loop. The biological hypothesis states that the frequency specific instantaneous power is related with synapse activation and synchronization between activated synapses. This hypothesis is proposed according to evidence given by the reviewed literature. In future experiments is intended to stabilize SSVEP responses in humans.

List of Figures

List of Tables

List of Equations

List of Abbreviations

BCI – Brain-computer Interfaces
BCM – Bienenstock-Cooper-Munro
BSDS – Brain Spikes Dependent Stimulation
CC – Correlation Coefficient
CCA – Canonical Correlation Analysis
CNS – Central Nervous System
EEG – Electroencephalography
ERP – Event-related Potentials
ES – Experimental Subject
FES – Functional Electrical Stimulation
FSP – Filtered Smith-predictor
IV – Instrumental Variables
LEADD – Linear Extrapolation Algorithm Defined Delay
LFP – Local Field Potentials
LGN – Lateral Geniculate Nucleus
LTI – Linear & Time-invariant
MC – Magnocellular Pathway
NLLSA – Non-linear Least Squares Algorithm
PAS – Paired Associative Stimulation
PC – Parvocellular Pathway
PID – Proportional-Integrative-Derivative
PTB3 – Psychophysics Toolboox 3
SEP – Sensory-evoked potentials
SISO – Single-input Single-output
SSVEP – Steady-state Visual Evoked Potentials
STDP – Spike Timing-dependent Plasticity
TBF – Time Best Fit
TMS – Transcranial Magnetic Stimulation
VEP – Visual Evoked Potentials

Acknowledgements

Aos meus pais, os maiores responsáveis pela criança que fui e pelo Homem que me tornei. Obrigado pelo esforço diário, por vezes exaustivo, dos últimos 23 anos para que eu e o Gonçalo tivéssemos tudo. Esta é mais uma etapa de uma caminhada que também é vossa. Orgulho! Ao futuro médico dentista, cujos gritos de revolta e murros na mesa às duas da manhã me deram uma motivação extra para continuar. Antes brincava com carrinhos na tua cabeça e agora já aprendo coisas contigo. Sempre juntos, a perseguir o nosso futuro maninho Gonçalo. À Mariana. Foste tu que mais aturaste as azias e depressões provocadas por todo este processo. És tu que, para além dos milhões de preocupações que já tens (sem contar com as peripécias da medonha FDUC), tens sempre tempo para te preocupares com os outros. Mereces este mundo e o outro. Estarei sempre cá para não caíres, e se caíres, estarei cá para te levantar. À Filipa, que tem sempre histórias para alegrar o dia à malta. Sem dúvida que a tua presença me animou durante este longo ano. Serás a próxima a conseguir o feito de acabar este curso. Estarei presente para o jantar comemorativo.

A toda a minha família. A todos os verdadeiros amigos.

Ao Gang: míticos jantares; cartadas em horas de aula; discussões filosóficas; discussões de arbitragens; lutas de galos; azias; risos; histórias. Levo comigo um bocadinho de cada um de vocês.

Um agradecimento especial ao Ernesto Soares (ICBR). Sem a tua ajuda este trabalho não teria sido possível. Obrigado por todas as horas que perdeste a aturar-me, ensinar-me e ajudar-me, pela atitude descontraída e mente aberta. Ao Professor Miguel Castelo Branco (ICNAS), pela ajuda e disponibilidade em momentos de maior aperto. Ao Professor Urbano Nunes (DEEEC e ISR), pela disponibilidade incondicional mostrada em assuntos mais técnicos deste trabalho e por todo o material e recursos disponibilizados para garantir o sucesso do mesmo. Ao João Perdiz (ISR) por estar sempre disponível para as minhas dúvidas e por ter tornado a minha estadia no ISR muito mais fácil. Ao Professor Gabriel Pires (ISR) por toda a disponibilidade e auxílio. Ao Professor César Teixeira (DEI) e à Doutora Teresa Sousa (ICNAS) pelas correcções finais.

"We can know only that we know nothing. And that is the highest degree of human wisdom." L.T.

Para o Dêde.

List of Contents

Chapter 1:

Introduction

The way in that complex structures of atoms and molecules interact to form neural networks whose dynamics originate consciousness, learning and memories can be overwhelming for our understanding. That's why the Human brain is one of the most remarkable biological structures in the known universe. Although the brain's anatomy and constitution are relatively well identified, the roles of structure, functions and connectivity between neural circuits are still not fully understood. Some hypotheses state that the anatomic structure has a major role in neuronal networks, but the overall functional connectivity of neuronal circuits in the brain cannot be explained solely by its anatomy [1] [2] [3] [4]. Elements like timing and spatial resolutions between excitatory and inhibitory 'avalanches' of action potentials considerably influence the functional and structural connectivity of brain areas [5]. Discoveries like these give insight into the complexity of dealing with brain dynamics. The human brain is composed by networks of neurons which generate neural oscillations that can be described as the change of field potentials in the extracellular region, promoted by the action potentials of synchronized neurons. These neural oscillations can be recorded into brain signals by non-invasive methods like Electroencephalography (EEG), thus facilitating the study of brain dynamics, mechanisms and the implementation of brain signal applications [6]. Delimited local regions of the brain can present oscillations at various frequencies, with each frequency being originated by several synchronized neurons. Phase synchronization of neural oscillations originating from short-range and long-range neural networks support the hypothesis that synchronization is of major importance in neuronal mechanisms involved in cognition, memory and motor function [6] [7] [8] [9]. Unbalanced synchronization patterns and lack of time precision in local network

firing within brain circuits and between specific interdependent brain regions can trigger several neuropsychiatric and neuro-motor pathologies such as epilepsy, dementia, schizophrenia and Parkinson's. [9] [10] [11] [12] [13] [14]. Having the ability to induce oscillations and consequently phase synchronization could be a potential approach to mitigate the consequences of neuropsychological diseases and even to enhance some physiological features of the human brain. The limitation is that brain's dynamics are still not fully understood and documented. It's not yet fully understood which amplitudes and oscillatory frequencies influence which brain mechanisms neither is the influence of synchronization dynamics in the neurophysiological and neuropsychological mechanisms. There is still a long way to go to accomplish such outstanding achievements. Besides, is necessary to prove if neural oscillations and specific synchronization related EEG signals features can be induced and controlled, and to document the implications of such procedures.

1.1 Background Research

In previous research conducted by *Soares et al* [15], the delivery of visual stimulation based on steady-state visual evoked potentials (SSVEP) was used to influence a frequency domain EEG variable recorded in the visual cortex region (occipital region of the scalp). This variable of interest corresponds to a specific frequency instantaneous power calculated at the stimulation frequency and can be interpreted, in biological terms, as a complex measurement of two important physiological parameters: the number of synapses activated at the stimulation frequency; and the degree of synchronization between those specifically activated synapses [16] [17]. In the experiments it was possible to induce oscillations in the instantaneous power with frequency of ~1 Hz, in counter phase with the stimulation onset. This showed promising evidence that it is possible to influence, in a non-fully controlled way, the amplitude of neural oscillations recorded above the primary visual cortex using non-invasive techniques both to induce and to record brain potentials.

1.2 Contextualization

In the world of Brain-Computer Interfaces (BCI), the majority of applications focus on recording brain signals containing information about the subject's intentions or mental state. Common definitions state that BCIs measure the brain activity, isolate raw signal features or event-related potentials (ERP), use the information to bypass physiological pathways of peripheral nerves, and interact directly with external devices through brain signals [18] [19] [20]. Common applications are normally dependent upon subject's intentions and aim to restore alternative motor capabilities to disabled individuals with unharmed brain function [21] [22].

On the other hand, there is a need to develop clinical applications to restore or enhance neural function in patients with neurophysiological diseases. The understanding that neurological patients may present a small chance for improvement of functional neurological conditions turned some attentions to the rehabilitation potentialities of BCIs, where most solutions resort to subject's learning to change brain activity with help of neurofeedback indications by real-time BCI applications [19] [23] [24].

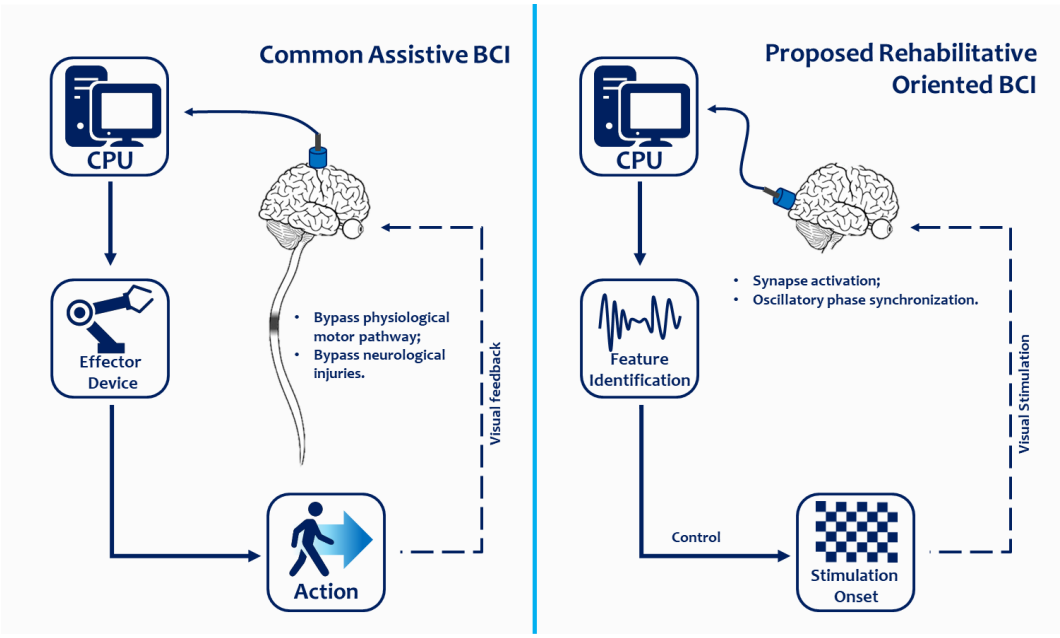

Figure 1.1) Assistive vs rehabilitative oriented BCIs. Two potential fields of application for BCI systems: the most conventional assistive approach, where specific brain signals and/or features encode instructions of external devices to bypass physiological motor action (left); and rehabilitation oriented approach, where brain signal recordings are used in algorithms in order to perform brain activity dependent stimulation with therapeutic goals (right). Adapted from: *Krucoff et al* [25].

This project proposes following research in the field of rehabilitative BCIs, as it is intended not to encode brain information to hardware commands, but rather to record real time brain activity and use extracted information to induce alterations in the oscillatory patterns of specific brain regions (in the case of this study, the primary visual cortex). The pharmacological difficulty in finding solutions to neurophysiologic and neuropsychiatric injuries/conditions, combined with the development of computational processing capacities and electrophysiological recording techniques turned the attention of researchers to the possibility of using BCIs as tools to improve patient's conditions [19]. Ultimately, it is intended to make a statement that neural oscillation and synchronization can be induced and marginally controlled using visual stimulation techniques. These objectives diverge from the majority of rehabilitative BCI also, because it requires no voluntary action or training from the subject who is interfaced with the system. In opposition to studies where brain stimulation is supported by the patients efforts to perform a task, the line that this project tries to draw is to create incentives and provide proof that it is possible to develop rehabilitative and/or function enhancing solutions that require no voluntary efforts from the patient. If this project shows successful, there is hope that similar researches can follow on the work developed.

1.3 Objectives

In continuance of *Soares et al* research [15], the project's objective is to develop a BCI control system to manipulate a periodic visual stimulus onset and offset, in order to stabilize the amplitude of induced neural oscillations at the stimulation frequency recorded in the scalp through EEG. In other words, the EEG data recorded in the brain will be continuously processed and used as feedback to a control system that commands the stimulation, with the goal of stabilizing a specific oscillatory instantaneous power component at the output of the EEG. First, SSVEP mathematical models based on averages of previously obtained experimental EEG data will be calculated. The models are expected to reproduce brain responses to the specific type of stimuli delivered. Then, a control system to stabilize frequency-specific

oscillation's amplitude of those models will be implemented and tested. Simulation results will evaluate concept performance and will justify if the system can be adapted to perform real-time closed-loop experimental tests. The final objective is to develop a working BCI prototype in humans. In this approach the neurofeedback is to be non-voluntary, meaning the Experimental Subject (ES) only has to gaze at the center of the stimulation screen. The work developed is meant to serve as proof of concept, stating that it is possible to control brain oscillations measured through EEG using a simple non-invasive feedback control loop. In this thesis, all the simulations, software and hardware frameworks used to implement a functioning BCI setup will be exposed. Experimental trials using the systems implemented will be performed in future work. It is expected that, if proven successful after experimental trials, this approach can be discussion opener and an incentive for future studies in the area of non-invasive induced synchronization, which ultimately can be used to improve communication dynamics in target brain networks and/or the introduction of novel neuro-therapeutic strategies.

1.4 Basic Concepts and Definitions

In this section some basic definitions of concepts that will be considered during the course of the thesis are introduced.

Neurons:

Neurons are electrically excitable cells [26] that compose the nervous tissue, communicating and transmitting nervous pulses through synapses.

Action Potentials:

Action potentials in neurons are characterized by rapid depolarizations followed by repolarization in specific locations of the cell's membrane, giving rise to nerve impulses along the axon's membrane [27].

Synapses:

Synapses are structures of communication between individual pre- synaptic neuron(s) and one or more post- synaptic neuron(s). These can be chemical (neurotransmitters) or electrical and are the 'bridge' that enables the transmission of

nerve pulses. Also these structures can be excitatory or inhibitory, respectively promoting or demoting spike trains depending on the specific functions or characteristics of those spike trains.

Neural Circuit/Network:

Neural circuits are composed by interconnected, function specific neurons. Several low-range and long-range neural circuits connect by means of interneurons to exchange distributed information and to form larger networks [28].

Event-Related Potentials (ERP):

Electrical activity recorded in the brain as a result of cognitive/motor defined events or sensory inputs. ERPs are characterized in terms of amplitude and time delay between the 'event' and the recording of the related brain response [29]. These 'events' are characterized by being isolated, giving enough time for the brain system to resume a 'homeostatic state' before the next stimulus is presented [30]. ERPs can be easily estimated through averages of events present in EEG's single trial data, in the case of this study, averages of the periods in which the stimulation is ON/OFF.

Steady-State Visual Evoked Potentials (SSVEP):

Brain potentials that can be measured with EEG equipment in the occipital region of the scalp. These potentials are associated to long periods of continuous stimulation, originating potentials than are correspondent in frequency and phase with the visual stimulation presented [30].

Brain-Computer Interface (BCI):

Computational systems that bypass conventional efferent physiological pathways through the recording of brain signals directly from the scalp (non-invasive methods) or from implanted electrodes (invasive methods). The recorded brain signals possess information about subject's intentions, attention, neurophysiological states or pathology related features [19].

Control Systems:

A closed-loop control system is characterized by the determination of system's inputs based on the outputs of that same system, in order to stabilize the system's response in desired and calculated values. These systems often recur to feedback from sensors or system state estimators to fulfill their purpose [31].

1.5 Thesis Outline

In Chapter 2, an introduction to some basics regarding the mechanisms involved in brain functioning and in neural oscillations will be made, with the objective of building a better understanding about the complexity and dynamics of the brain. Some of the content justifies decisions and system components along the way. An introduction to brain-computer interfaces (BCI), steady-state visual evoked potentials (SSVEP), programs and functionalities used, calculations, control theory and control strategies will also be made. Subsequently, selected research and state of the art rehabilitative BCI related frameworks will be exposed, in order to perform comparisons and establish differences between existing approaches and the goal of this project. In Chapter 3, the methods used are explained in a chronological way, pointing out problems faced during the course of the project and solutions encountered to work around them. Failed results will be pointed out in order to justify the search for alternative solutions to the specific problems encountered during conception and implementation of simulation systems. This chapter includes brain SSVEPs computational modeling strategies, validation of the computed models, for purposes of brevity model selection will be made according to correlation results with experimental data and implementation and testing of several prototypical control designs. In Chapter 4, the selected models are embedded in the control prototypes that showed the best results in Chapter 3. The results obtained with every model are analyzed and compared. Their discussion will be performed to justify the development of a real-time framework to undergo experimental trials. In Chapter 5, a real-time BCI prototype will be presented, developed with the goal of performing real-world validation of the neurofeedback system described in the previous chapter, the difficulties encountered during conception and limitations. In the final Chapter 6, some conclusions about the work developed will be exposed, limitations, comparisons to other approaches and suggestions for the future work in this field.

Chapter 2:

Fundaments & Literature

Understanding physiological dynamic systems allied with hardware and software knowledge is of maximum importance to implement systems that interact with biological networks. In this chapter, biological and technical concepts, related with the implementation of the proposed solution, are exposed in order to build a better understanding about mechanisms involved in such solutions. Some brain dynamic concepts are discussed in relation to available scientific literature, since some derive from theories and couldn't be proven till the present day due to the difficulties involved in the study of the human brain.

2.1 Neurophysiologic Fundamentals

2.1.1 Introductory Description

Neurons in the brain function within networks, in which one neuron is influenced by multiple pre- and post- synaptic connections to neighbor neurons, forming circuits that fire in synchronized rates. The synchronization phenomenon presupposes the existence of an excitatory and/or inhibitory coordination between neurons present in the same network, leading to the generation of Local Field Potentials (LFP) that can be measured in the scalp with EEG techniques [32]. Excitatory synapses induce action potentials in the post-synaptic neurons that in turn generate electrical activity. The synaptic interaction between neurons within a small volume of nervous tissue gives rise to coordinated patterns of neuron's activity. This coordination causes the neurons to fire in synchronized patterns, with each individual neuron producing electrical activity with millisecond scale differences between action potentials. The electrical potentials from individual neurons interact

in constructive ways (constructive interference) originating electrical fluctuations with greater amplitudes, commonly referred as neural oscillations [33]. As a result of synchronized firing patterns, neural oscillations in one network can act as input to nearby cortical areas, following the same principle of constructive interference and giving place to oscillations with even greater amplitude, the LFPs. These principles reflect that scalp electrodes do not measure electrical activity of single neurons, neither the activity of individualized neural networks, but rather the summed activity of synchronized networks that are composed by millions of individual nervous cells [34]. The totality of individual neurons present in networks of cortical regions (where specific frequency neural oscillations are recorded) do not necessarily present the same frequency firing patterns, given that individualized neurons are often activated under specific physiological conditions and that networks in common cortical areas can be synchronized in different ways [35]. Such findings support the conclusion that brain activity measured with scalp electrodes can be characterized by the sum of endogenous electrical fluctuations (due to excitatory and/or inhibitory connections between local neurons) and in particular Sensory Evoked Potentials (SEP), represented as fluctuations in LFPs due to the stimulation of sensory organs that send pulses to the brain via efferent pathways [36] [37]. LFPs recorded in localized regions of the scalp presenting spectral power (frequency domain of the EEG signal) at a wide range of frequencies is supporting evidence that the EEG brain activity measured is due to several simultaneously occurring phenomena.

2.1.2 Neural Plasticity

Oscillations in the brain's electrical activity are based on spatial and temporal relations of connectivity between networks, relations which are constantly changed due to sensory inputs and feedbacks from engaged networks. These dynamic relations induce modifications mainly in the functional connectivity of the brain networks, reinforcing or undermining the specific connection's strength based on individual neurons 'firing' timings. This principle is referred to as Spike-Timing-Dependent Plasticity (STDP), which explains the strengthening of synaptic

connections to potentiate 'communication' of active networks, characterized by time-based patterns of pre- and post- synaptic action potentials in the neurons of interconnected regions [25] [38] [39].

As stated by Donald Hebb [40]:

"Let us assume that the persistence or repetition of an activity tends to induce lasting cellular changes that add to its stability."

Dr. Hebb introduced the concept of STDP, which led to further studies about the subject, reporting that synaptic connections are strengthened based on repeated post- synaptic induced activity in intervals of 0 to ~50 ms after pre- synaptic firing. The STDP model shows promise in very simplistic *in vitro* conditions, however fails to perform in more complex and reality-close environments [39]. The Bienenstock-Cooper-Munro (BCM) model [41] defends that neural plasticity is not only post-synaptic firing dependent but also relies on a non-linear selectivity of post- synaptic neurons to drive specific pulses, model which show contradictory results against the STDP, even in simple conditions [39]. The lack of consensus, variable explicatory mechanisms and the existence of numerous theories with contradictory results are a glimpse to the complexity involving functional plasticity. Plasticity can occur structurally and functionally. Since structural plasticity relates to neuron 'wiring' and genesis of synaptic structures in maturation stages of the brain neurons [42], the focus of most studies is on functional plasticity. Functional plasticity can incorporate modifications in synaptic connections, strengths and changes in neuron intracellular properties, creating adaptive and/or maladaptive changes in the highly structured dynamic networks of the brain [42] [43] [44]. Maladaptation can be one of the bigger obstacles to rehabilitative efforts since it can induce unwanted modifications in the dynamics of target networks. Nevertheless, correctly induced plasticity can be a gateway to recover or improve function in patients who've experienced neurological injuries, given that the Central Nervous System (CNS) promotes adaptation and increases possibility for synaptic strengthening in the aftermath of injury [44] [45]. Plasticity is not a mechanism by itself, but rather a consequence/finality of several coordinated mechanisms that are involved in the physiological dynamics of the brain (see Figure 2.1 in section *2.1.4) The Role of Phase Synchronization*).

2.1.3 Neural Synchronization

The definition of 'neural synchronization' depends on the context in which the expression is used. At microscopic scale (individual neurons), 'neural synchronization' refers to the time sensitive induction of post-synaptic action potentials, in order to synchronize pre- and post-synaptic firing patterns [6] [38]. At mesoscopic scale (local neuron's networks), 'neural synchronization' is used to describe oscillation phase relations between neural circuits in local cortical areas. Translating into EEG recordings, refers to an enhanced EEG power at a specific frequency in one cortical region, power which varies depending on the number of synapses activated and on the degree of phase synchronization between the neurons involved in the generation of such frequency specific oscillations [6] [38] [46]. At macroscopic scale (cortex regions), 'neural synchronization' refers to matching oscillatory phase in the LFPs of distant cortical regions, phenomenon that is facilitated by the strengthening of synaptic pathways and repetitive communication [6] [38].

Different stimuli can have different representations in synchronization patterns, ultimately increasing or decreasing the amplitude of specific frequency oscillations, a phenomenon described as event-related synchronization and event-related desynchronization, respectively [6].

2.1.4 The Role of Phase Synchronization

Several studies defend that the overall brain functioning is based on information sharing through several long-range cortical regions, based on the fact that random samples of neurons in the cortex contain motor information [25] [47] [48] [49]. One can infer that the brain may function as a distributed system, where specific networks interact to perform specific tasks, being the structural and functional communication between those networks one of the keys for normal system performance. The synchronization of oscillations originated from different networks assumes a major role in driving communication between active brain zones by supporting the coordinated arrival of inputs at post-synaptic neurons [50].

Synchronization drives the overall communication between brain regions, acting as the link between networks of a distributed system, enabling each network to send and receive feedback from phase matched networks and providing information integration [51]. Normal motor control, for example, depends on precise long-range communication that is achieved through oscillatory synchronization between the brain's regions involved in generating specific movements [9]. Moreover, a dynamic time-precise relation between synchronization and desynchronization of different short- and long-range networks is likely fundamental to the development and maintenance of cognitive function [52].

In terms of pathological significance, abnormalities in synchronization/ desynchronization patterns can cause failures in neurophysiological performance. Neuropsychiatric conditions have been associated with defects on brain synchronizations, ultimately resulting in tremors, seizures and difficulties in motor action [9], with studies showing that alterations in normal oscillatory and synchronization patterns in neurons within the basal ganglia associated with defective long-range network communication are key aspects in the pathophysiology of patients with Parkinson's disease [53].

Phase synchronization has also been acknowledged as important to induce functional plasticity [6] [9] [54]. The repeated synchronization of firing rates in interconnected regions enables the maintenance of individual neurons potential near the threshold, making these more likely to fire and facilitating the repeated excitability pathway, leading to the plasticity characteristic strengthening of synaptic connections that are often excitatory, in opposition to the deterioration of connections that aren't so often excitatory [45].

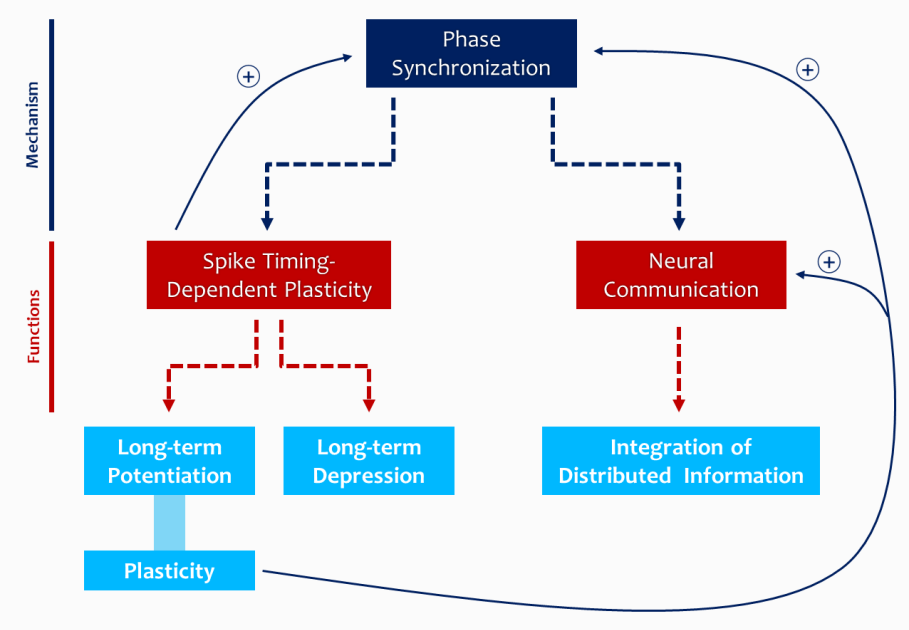

Figure 2.1) Brain dynamics schematic representation. Simple schematic representation of brain dynamic's related with phase synchronization of network firing patterns. It is consensual in several studies that phase synchronization is related to synaptic strengthening and communication between cortical regions. Adapted from: *Fell et al* [6].

Some studies postulate that plastic changes strongly rely on the specific latency between pre- and post- synaptic firing [39] [55], providing more supporting evidence that neural synchronization driven communication and coordination mechanisms are important in the induction of neural plasticity.

2.1.5 Visual Pathways

We perceive the world thanks to the light that is reflected or refracted from surrounding objects. The human eye contains approximately 125 million photoreceptors. These photoreceptors are nervous cells specialized in converting visible light (electromagnetic waves within the visual spectrum of the human eye) into electrical signals that can be transmitted through neurons' action potentials [56] [57]. The retina is the eye structure where the photoreceptors are found, making it the fundamental entity of photo transduction. When light stimuli are formed in the retina, the photoreceptors generate electric pulses that travel to the brain via the optic nerve [56]. These structures form the half of the visual pathway that is located outside the Central Nervous System (CNS). The optic nerve transmits the impulses generated in the retina to the Lateral Geniculate Nucleus (LGN), a thalamic structure

present in both hemispheres, directly connected to the primary visual cortex. The LGN receives sensory inputs directly from the retina, sending and receiving feedback information from the visual cortex, being defined as an interconnection center between the eyes and the brain structures that perceive sight [58].

The visual system possesses several parallel processing pathways, where multiple stimulus characteristics such as bright, contrast or depth are transmitted and processed (see Figure 2.1). The LGN acts as a re-transmission center to direct the characteristic-specific pulses to the respective pathway. The primary visual region of the cerebral cortex is the sensory pulse final destination, where the visual information will be processed [57].

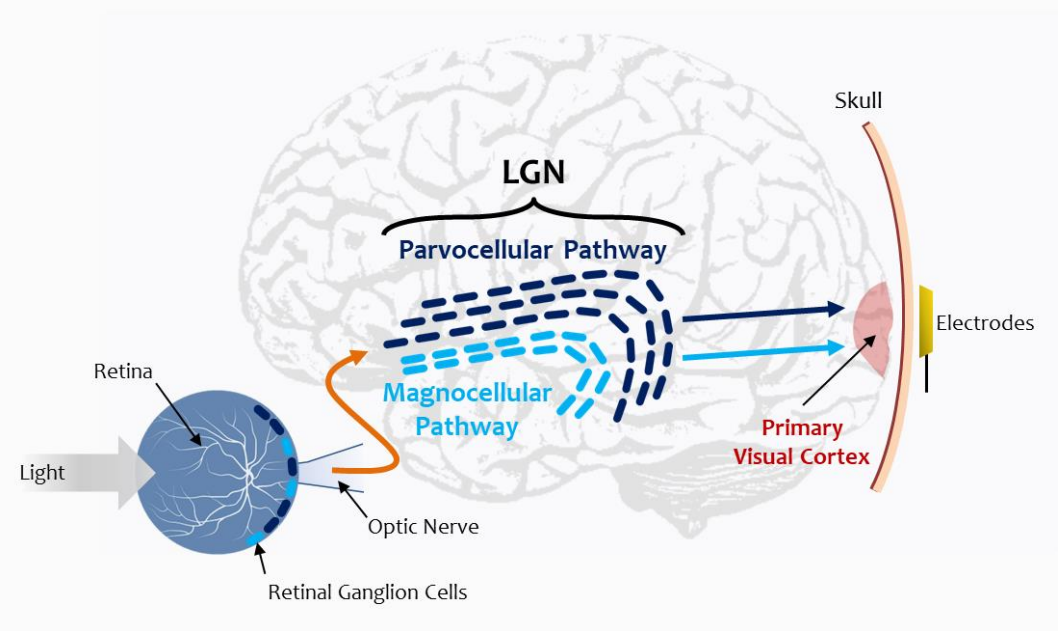

Figure 2.2) Visual pathways schematic representation. Simplified schematic representation of the visual pathway starting with the absorption of light by the photoreceptors in the retina, followed by generation of impulses (action potentials), transmission through the optic nerve to the LGN, relay of visual information in the LGN through the parvocellular and magnocellular pathways and information processing in the primary visual cortex. Adapted from: *Cotrina et al* [57].

The magnocellular pathway (MC) is responsible for motion and depth perceptions, preferably driving color-neutral and high temporal frequency reverse contrast information, while the parvocellular pathway (PC) is responsible for color distinction and spatial contrasts, preferably carrying color, spatial luminance and low temporal frequency reverse contrast information [37].

The electrical responses of the occipital region of the scalp due to light stimulation are called Visual Evoked Potentials (VEP) and can be measured using

non-invasive techniques such as EEG. VEPs are due to the synchronized firing of several neural networks in the V1 cortex region, being characterized by low amplitudes and difficulty in being isolated from the background EEG [16] [17].

In previous research, after performing EEG recordings in the occipital region of the scalp, it was estimated that the visual pathway introduces a physiological retina-visual cortical transmission delay, since the stimuli onset and the initial corresponding EEG feature were separated by a delay of approximately 55 milliseconds [15]. Additionally, the possibility of refractive repercussions in the cases where experimental subjects present weak visual acuity must be considered. Lack of visual acuity can lead to noisy and delayed VEP readings and correspondences [57].

2.2 Recording and Modulating Brain Signals

2.2.1 Electroencephalography

Electroencephalography is a non-invasive technique to record real-time electrophysiological brain potentials. The EEG equipment possesses electrodes that are positioned on the intended scalp regions. EEG electrodes capture not the action potentials of individualized neurons, but rather the summed activity of neurophysiological processes (such as neural firing). It is thought that scalp electrodes mainly represent postsynaptic potentials [59]. The EEG techniques are characterized by having high temporal resolution but very poor spatial resolution, so during recording it cannot be assumed that the source of the signal is directly below the recording region but rather that the output signal is a combination of desired events and background brain activity, considered as noise [59]. For the purposes of this project, the high temporal resolution is very important, given that the BCI system to be developed strongly depends on time precision. The spatial resolution is the major issue. The brain signals recorded originate from various constructive interferences of several LFPs, so the relation between the target potentials and the target brain dynamics can turn out to be not so direct. Still, given that the microscopic brain dynamics are very poorly understood, the marginal control of potentials can be advantageous for future studies.

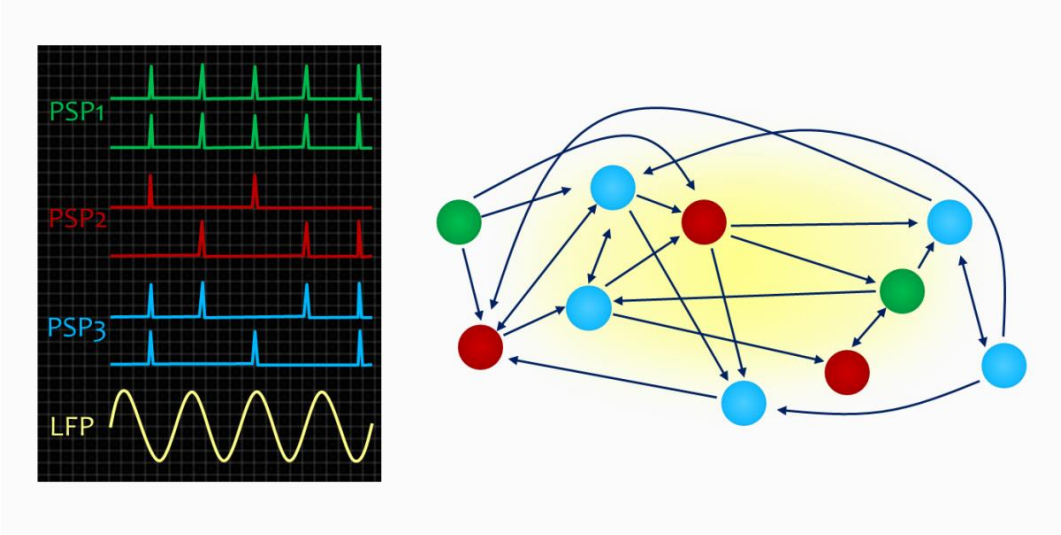

Figure 2.3) LFPs origin schematic representation. Example of different post- synaptic potentials (PSP) synchronization in a local cortical network. The network is characterized in EEG recordings by its local filed potentials (LFP) and not by the activity of single neurons. Adapted from: *Schnitzler et al* [9].

The raw EEG data can be interpreted as a measurement of sinusoidal waves combination that are individually generated by large populations neurons, so a spectral decomposition and frequency analysis are pertinent to perform studies and extract features. EEG has a large range of applications in BCIs due to the advantages of having good temporal resolution and being non-invasive, facilitating prototype implementation. It has often been used in spellers [21], motor recovery/assistive studies from controlling the movement of wheelchairs [60] to robotic limbs [61] and in environment control systems [62].

2.2.2 The Steady-State Visual Evoked Potentials

When implementing BCIs, the brain signals recorded can present transient responses (ERPs), associated to single events that can be delivered in stimulation trains or by isolated stimulus; or steady-state responses, associated to continuous stimulation during long periods of time, originating potentials that are correspondent in frequency and phase with the delivered stimulus [30]. The brain electrophysiological recordings used in this study will be steady-state visual evoked potentials (SSVEP), characterized by the frequency and phase correspondence with the visual stimulation flicker that originated those same potentials, maintaining its parameters constant for relatively long periods of time when analyzed in the

frequency domain. The recorded potentials possess power at the fundamental frequency and also at the respective harmonics, so if the frequency of a flickering stimulus is 10 Hz, the SSVEP responses will have powers at 10 Hz (fundamental frequency/first harmonic), 20 Hz (second harmonic), 30 Hz (third harmonic) and so on. The SSVEP responses present excellent signal-to-noise ratio in comparison with transient visual evoked potentials (VEP), are very resistant to recording artifacts and are also possible to measure with EEG, making the use of these potentials very tailored for real-time BCI applications. Drawbacks of this technique include habituation to the stimulus induced and subject's visual and attention fatigue. In terms of system implementation and simulation, the SSVEP can be challenging because the visual stimulus has to be converted to an electrical signal that can be used as input for computer modulated brain systems. The frequency range of SSVEPs can go from 3 to 50 Hz [63]. If the frequency of the flicker is higher than 10 Hz, the SSVEPs recorded are sinusoidal, being described as external induced oscillations in the local-field potentials (LFP) [64]. This corroborates the hypothesis that SSVEPs can drive synchronization, consequently originating sinusoidal like neural oscillations in the LFP. The SSVEP can be induced through several methods: flashing lights, which shows great variability across subjects; pattern reversal, which presents the lowest variability in delays and waveforms; pattern onset/offset, which shows a little more variability than the previous [37]. The origin and distribution of visually evoked responses are not yet completely understood. In the review of *Vialatte et al* [37] are exposed theories that try to explain the generation and propagation of the SSVEP responses. According to these theories the SSVEPs are generated in the primary visual cortex and then transmitted or propagated to neighboring networks. The potentials' propagation implies that the involved regions are connected and communicate. If the potentials' communication and propagation is made through phase synchronization of interconnected neural networks oscillations as explained earlier then, in theory, it's possible to induce inputs into several brain regions through the induction of controlled potentials in the visual primary cortex (see Figure 2.4).

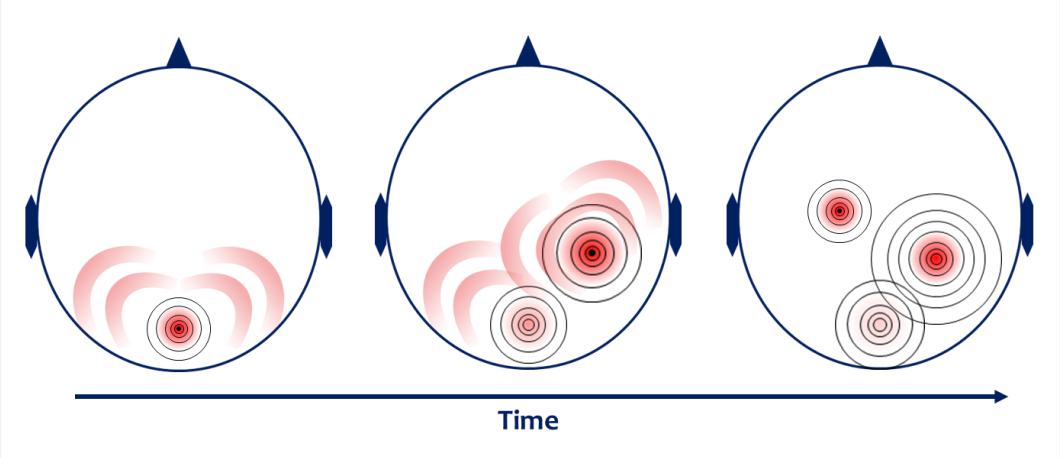

Figure 2.4) SSVEPs propagation in the brain. Schematic representation of the propagation of the SSVEPs after generation in the primary visual cortex. Adapted from: *Vialatte et al* [37].

The only conclusion that might be taken from the existence of propagation theories and from the difficult comprehension of the SSVEP potentials dynamics within the brain networks is that these processes are driven by non-linear mechanisms, as are all major brain dynamics.

Potentialities and applications of SSVEP range from the very common spellers, [21] study of cognitive mechanisms such as visual attention [65] and working memory [66], to neuropsychiatric studies of social cognition [67].

2.2.3 Brain-Computer Interfaces & Neurofeedback

Neurofeedback BCI system components encompass electrophysiological signals recording, signal processing and feature extraction, feedback signals generation and subject's adaptive training to interpret real-time feedback signals, working in a 'symbiotic' way between subject's efforts and machine recordings and processes. Approaches like these are found in visual attention studies, where repeated sessions of learning aim to give patients the control over own-brain activity through feedback signals visualization. It has been reported that these approaches induce network plasticity after several training sessions and ultimately improve subject's attention [42]. The opinions about neurofeedback approaches are divided among researchers. Some critics defend that studies conducting neurofeedback BCIs use very controlled

conditions and low number of samples to support their conclusions, while others criticize the experimental setups and experimental designs [19]. These evidences show that there is still a long way to go to have conclusive and acceptable results regarding induction of biological functional changes through neurofeedback approaches. There should be more investment in this type of research and in different attempts to induce neurophysiological changes, starting by the more basic mechanisms and building the way to the most complex.

2.3 Dynamic Systems and Control

This section covers some definitions and methods used in computational models calculation, control theories and strategies. The purpose is to provide a very basic understanding about the concepts involving the systems to be implemented further in this thesis (*Chapter 3: Methods & Control Designs*).

2.3.1 Linear & Time-Invariant (LTI) Systems

Linear & time-invariant (LTI) systems are defined by their linearity and time invariance properties. System's linearity is characterized by homogenous and addictive properties, defined in continuous time by the following representations (Equations 2.1 and 2.2):

$$If\ \ x(t) \rightarrow y(t), \qquad then\ \ \alpha x(t) \rightarrow \alpha y(t) \quad (homogeneity) \quad (2.1)$$

$$If\ \ x_1(t) \rightarrow y_1(t)\ \ and\ \ x_2(t) \rightarrow y_2(t),$$

$$then\ \ x_1(t) + x_2(t) \rightarrow y_1(t) + y_2(t) \quad (additivity) \quad (2.2)$$

System's time invariance is characterized by the ability of the system in giving a specific response to a specific input independently of the time T in which the input enters the system (Equation 2.3).

$$If\ \ x(t) \rightarrow y(t), \qquad then\ \ x(t-T) \rightarrow y(t-T) \quad (time\ invariance) \quad (2.3)$$

LTI systems are more amenable to perform analysis. That is why non-linear systems can be often approximated to LTI systems to implement complex control systems for real life applications.

2.3.1.1 Transfer Function Systems [68]

LTI systems represented as transfer functions use a polynomial ratio to describe relationships between system's input signal(s) and respective output(s). The transfer function parameters are the poles (roots of the denominator), the zeros (roots of the numerator), transport delay and noise factor. In continuous time, the system's output is given by the convolution between the system's impulse response and the system's input (see Equation 2.4):

$$y(t) = h(t) * x(t) \quad (2.4)$$

where $x(t)$ is the input, $y(t)$ is the output and $h(t)$ is the impulse response of the system. This is the most simplistic way of representing the relations between dynamic system's inputs and outputs. The transfer function in continuous time domain $H(s)$ can be obtained by rearranging the previous equation variables and performing Laplace Transforms to the input and output signals (see Equation 2.5):

$$y(t) = h(t) * x(t) \quad (=) \quad h(t) = \frac{y(t)}{x(t)} \quad (=) \quad \mathcal{L}\{h(t)\} = \frac{\mathcal{L}\{y(t)\}}{\mathcal{L}\{x(t)\}}$$

$$(=) \quad H(s) = \frac{Y(s)}{X(s)} \quad (2.5)$$

where $X(s)$ and $Y(s)$ are the Laplace transforms of the input, output and noise factor, respectively. The system's order is defined by the transfer function's order of the denominator polynomial.

2.3.1.2 System/Model Identification

With resource to the *System Identification Toolbox*™ application from *Matlab*™, it is possible to obtain identified linear & time-invariant (LTI) system models using measured input and output signals in the real process. The resulting models/systems are represented by continuous time transfer functions. Number of poles, number of zeros, delay and initialization method parameters are defined accordingly to the desired model outcome (see Figure 2.5).

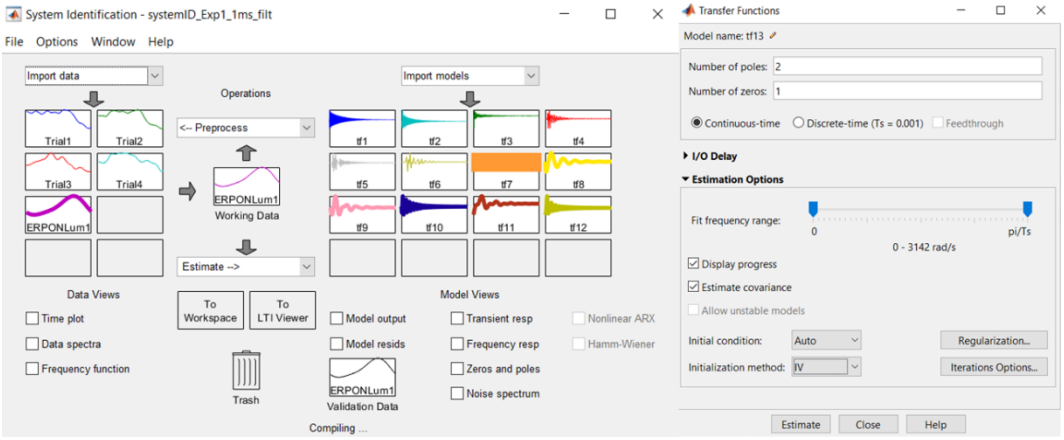

Figure 2.5) ***System Identification Toolbox*™ application interface**. The blocks on the left (Trial1, Trial2, …, ERPONLum1) represent the uploaded input and output measured data for different experiments/trials. The blocks on the right (tf1, …, tf12) represent the estimated models, each generated with different parameter specifications and, consequently, possessing different percentage fittings to the measured output data.

The *Instrumental Variables* (IV) initialization method is used for the estimation of initial conditions of single-input single-output (SISO) LTI transfer function models that have a non-identified type of noise.

2.3.2 Control Theory

Control theory resorts to mathematical operations to deal with dynamic systems management, in order to come up with strategies to control outputs of such systems in desired ways. These strategies must ensure the stability of the system, prevent overshooting and work around the existence of delays that might occur in some system components or are inherent to the real process.

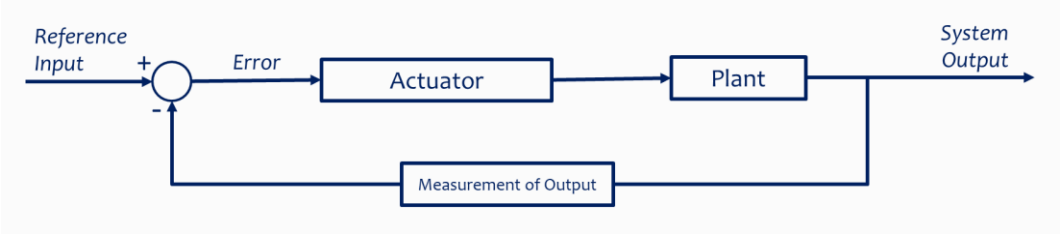

Figure 2.6) Controller example. Schematic representation of an actuator (normally a controller) and a plant (process which output is to be controlled) in a closed-loop system design.

A closed-loop system is characterized by the inputs determination based on output responses of the system, given by sensors or system state estimators feedback measurements (see Figure 2.6). Control designs are used to accomplish reduced errors and satisfactory dynamic responses for systems comprising continuous and time sampled signals. The "regulator approach" to control systems aims at stabilizing a physical variable with disturbances (in the case of neurophysiological systems: measurement noise and non-desired sensory evoked potentials that influence the interest features) in a desired value [31].

2.3.2.1 PID Controller [69]

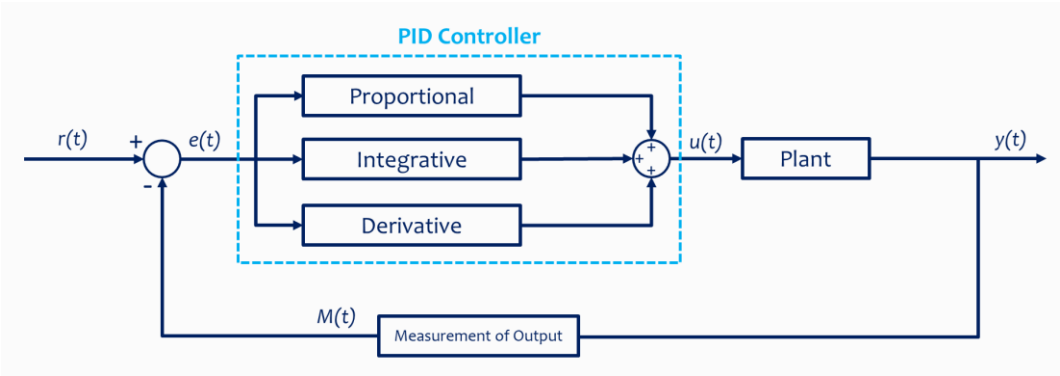

Figure 2.7) PID controller structure. *r(t)* is the reference value, *M(t)* is the measured value of the output, *y(t)* is the output of the plant process, *e(t)=r(t)-M(t)* is the value of the error used as input to the PID controller and *u(t)* is the control variable. The *Plant* block represents the system which output is desired to stabilize in the reference value.

A Proportional-Integrative-Derivative (PID) controller continuously calculates an error (*e(t)*) defined by the difference between a defined reference value (*r(t)*) and the measured value at the system's output (*M(t)*). The error value *e(t)* is corrected by the PID's three branches, characterized by the best proportional, integral and derivative gains combination, in an attempt to minimize the error by application of a control variable (*u(t)*) to the input of the system's plant (Figure 2.7).

$$u(t) = K_p e(t) + K_i \int_0^t e(t')dt' + K_d \frac{de(t)}{dt} \quad (2.6)$$

The overall control function, in order to the control variable *u(t)*, can be mathematically represented as shown in Equation 2.6, where K_p, K_i and K_d are the proportional, integrative and derivative controller gains, respectively. The different terms complement each other. The proportional control term is the trivial method of control, driving the error to 0, but fails when the system possesses disturbances, causing overshooting and instability in the control. The integrative control term takes in account the time passed in which the error is non-zero, forcing the control variable to increase the output of the system accordingly. The derivative control term considers not the absolute value of the error but rather the variation of the error (*Δe(t)*), trying to bring the variable *Δe(t)* to zero. The system stability relates to the control system capability in maintaining the output stable over time. If the system has to perform repetitive overshoot corrections (positive and negative), the output oscillates. If the oscillation's amplitude decreases over time, the system is considered stable. If the oscillation's amplitude increases, the system is considered unstable. If the oscillation's amplitude remains constant, the system is considered marginally stable.

The PID controller transfer function in discrete time domain is represented in Equation 2.7:

$$H_{PID}(z) = \frac{\beta_0 + \beta_1 z^{-1} + \beta_2 z^{-2}}{(1 - z^{-1})} \quad (2.7)$$

$$\beta_0 = K_p\left(1 + \frac{T_s}{K_i} + \frac{K_d}{T_s}\right); \quad \beta_1 = -K_p\left(1 + 2\frac{K_d}{T_s}\right); \quad \beta_1 = K_p\frac{K_d}{T_s}$$

where K_p, K_i and K_d are the controller proportional, integrative and derivative gains and T_s is the sampling period. The PID tuning can be accomplished in loop and depends on the mechanisms involved in the system, on the method to obtain the variable *M(t)* and on system/control delays. There are several phenomena that can drive system instability, such as non-linear blocks, functions, algorithms and transport or pure delays in the loop.

2.3.2.2 Smith-Predictor Controller [69] [70]

The Smith-Predictor works as a predictive controller for systems that possess a pure time delay. This type of controller uses two feedback loops (see Figure 2.8). The *Process* that is to be controlled is in the outer loop, with all the delays associated. The novelty, when compared with the PID structure, is the introduction of an inner loop that uses a replicative model of the original process (G_P), with the advantage of mathematically separating the process and respective delays incurred ($e^{-\tau s}$) into two separate functions/blocks.

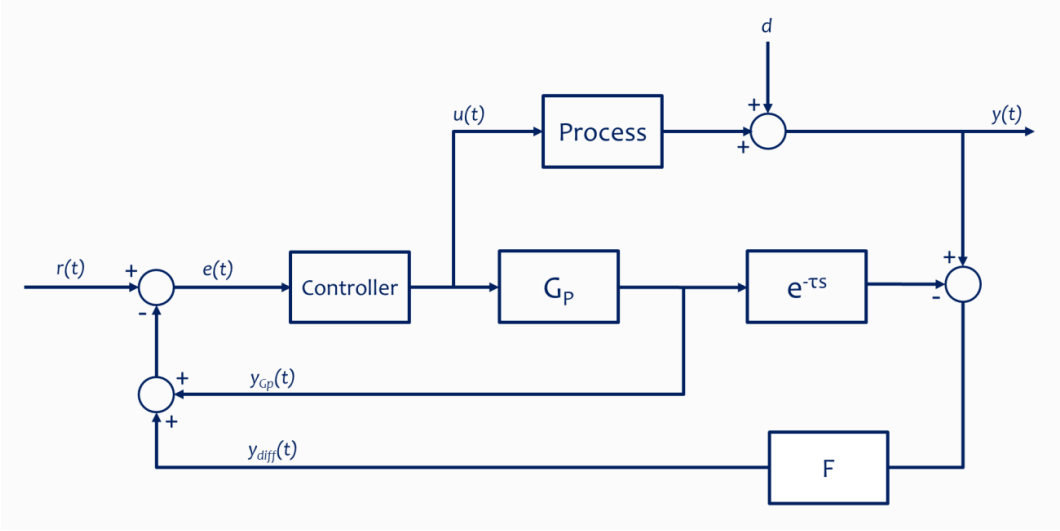

Figure 2.8) Filtered Smith-Predictor controller structure. The G_P block is a replicated mathematical model of the real process, $e^{-\tau s}$ is the real process delays mathematical representation, d are process disturbances and F is a first order filter.

The outer feedback loop calculates the difference between the output of the real process and the output of the delayed mathematically replicated model of the process ($G_p+e^{-\tau s}$). It's easy to observe that, if the process replication model is 100% successful, the outputs will be correspondent ($y_{diff} \approx 0$), and the maximum performance of the controller is achieved.

$$e(t) = r(t) - \left(y_{Gp} + y_{diff}\right) \quad (2.8)$$

The inner feedback drives the output of the replicated model. The real process and model outputs ($y^{diff}(t)$ and $y_{Gp}(t)$, respectively) are summed and the resulting value is subtracted to the reference value ($r(t)$) to obtain the error variable ($e(t)$) to be used at the input of the control (see Equation 2.8).

$$H_{FSP}(z) = \frac{H_{PID}(z)}{1 + H_{PID}(z)G_P(z)(1 - z^{-d}F(z))} \quad (2.9)$$

$$F(z) = \frac{(1-\alpha)^n}{(1-\alpha z^{-1})^n} \quad (2.10)$$

$$\alpha = e^{\frac{-T_s}{T_f}}$$

$T_f = time\ constant\ of\ the\ filter;\quad n = filter\ transfer\ function\ order$

Equation 2.9 represents the system's discrete time transfer function for the use of a PID controller in the Smith-Predictor scheme. The digital filter (see Equation 2.10) placed in the outer feedback loop allows the system to have an extra degree of freedom when dealing with disturbances that cannot be measured and with model G_P lack of replicative capabilities.

2.4 State of the Art in Rehabilitative BCIs

There is a very short list of studies regarding BCI neuro-rehabilitative approaches. Some researches include brain spikes dependent stimulation (BSDS) of efferent nerves and muscles in spinal injured patients; [71] paired associative stimulation (PAS) non-invasive techniques to induce nerve plasticity in human subjects through the combination of transcranial magnetic stimulation (TMS) and stimulation of damaged peripheral nerves; [39] and combination of brain signal recordings in monkeys with functional electrical stimulation (FES) of nerves and muscles to induce plasticity in injured pathways and consequently restore motor function in limbs. [72] [73]

Gharabahi et al [71] findings show that BSDS application using TMS promotes increased excitability in the motor cortex. Such discovery may present advances in artificially driven plasticity of efferent nerves and improve the recovery of patients with nerve or spinal cord lesions, but does not relate with cortical dynamics alteration required in cases of neuropsychiatric or neurophysiologic disorders. *Ethier et al* [39] found that correctly time coordination between TMS and motor-neurons electrical activation increase corticospinal inputs strength to those specific motor-neurons, and that the intervals between stimulations play a decisive role in the

process. Still this doesn't demonstrate palpable changes in cortical dynamics, only in the relations between the CNS and the peripheral neurons that transmit motor information.

On the other hand, *Guggenmos et al* [24] implemented a brain function restoring strategy in rat models focusing on communication mechanisms. After inducing injuries in the primary motor cortex of rat models to interfere with the somatosensory and motor cortical areas communication dynamics, a spike identifying neural prosthesis was implanted in the injured area of the motor cortex to trigger control somatosensory cortex electrical stimulation. This BSDS post-experimental analysis provided evidence of improved functional connectivity between the two target areas in comparison with the injury aftermath condition. The exposed study shows a lot of promise in terms of research but not in terms of applicability, because the strategies implemented rely on invasive techniques which are complex and dangerous to experiment on human subjects. *Rebesco et al* [55] accomplished changes in spontaneous neuron activity *in vitro* and also in rats using spike triggered electrical stimulation, ultimately reaching plastic changes in the rat models forelimb sensorimotor cortex. Evidence supports that plastic changes strongly depend on the precise timing between trigger-spikes and the stimulated activity. Once more the stimulation and spike detecting methods involved invasive procedures in animals, failing to prove that the experiments can be replicated in human subjects.

In a completely different approach, *Garcia-Molina et al* [74] enhanced synchronization of oscillations at low frequencies (slow waves) with auditory stimulus during sleep in humans. The auditory stimulation is applied during EEG controlled stages of subject's sleep, to ensure correct timing in the stimulus delivery. The strategy showed an increase in slow wave activity during stimulus delivery periods for a younger group of subjects tested in the study. This clearly is a strategy to enhance synchronization of frequency specific band linked oscillations with resource to non-invasive stimulation (auditory) and brain signal recording (EEG). Such approach coordinated with other strategies to possibly enhance long-range

synchronization can turn out to be very promising for the overall comprehension of the brain synchronization mechanisms.

The use of invasive methods for BCI rehabilitative research is the most common approach to induce plastic changes given the better performances both in stimulation techniques and recording demonstrated by this kind of equipment. The downside is the difficulty of implementing such strategies in humans, due to the need of surgical procedures to implant electrodes. The findings of *Garcia-Molina et al* [74] can be the proverbial light at the end of the tunnel in rehabilitative non-invasive research.

Chapter 3:

Methods & Control Designs

In this chapter, all the steps taken to implement the neurofeedback control prototype will be described, from EEG recordings, obtaining the variable of interest, and presentation of the final prototype. Furthermore, some results are presented and commented to justify the failure of some approaches and the need for new ones. All the EEG data used to simulate and test the system where recorded in *Soares et al* previous experiences [15] (see *Appendix A* for database description). To know the exact simulation instants in which the stimulation frames are shown on the screen (at a one millisecond scale), a light sensor (photodiode) is used to differentiate the frames that are shown in the screen and to know exactly when each frame appeared. First we present the calculations and algorithms used throughout the study, in order to have a better understanding about the calculations present in the control designs. All calculations, algorithms and software scripts are performed using *Matlab*™ environment and functions, including *Simulink*™ and *Matlab Toolboxes*™. All the amplitude values of signals present in the database and obtained in simulations are presented in arbitrary units (a.u.), because in the database it wasn´t specified the recorded electrical potentials units.

3.1 Calibration Techniques

As SSVEP potentials are generated in the primary visual cortex, the 10 most posterior EEG channels were recorded, to cover the occipital region (directly above the interest region). All the channels were bandpass filtered between 1 and 100 Hz. The aim was to induce an EEG recordable signal in the brain, so the solution was to compare the combination of the 10 previously calibrated channels (*Fit*) with the

stimulation signal (*Photo*), obtained via the light sensor. Therefore, the calibration and posterior combination of the channels would be made according to the best correlation results between channels and sensor's signal. The *Fit* which presents the best correlation with the light sensor's signal corresponds to a signal denominated *Time Best Fit* (TBF).

In every trial a very simple behavioral task is delegated to the subjects. The subject is asked to uninterruptedly fixate a symbol that appears in the center of the stimulation screen. The symbol can have three different forms: '+', '○' or '□'. When the '+' is present in the center of the screen, the subject must press a computer key when the '+' is replaced by the '○' in one frame period. This binds the subject's attention to the center of the screen. When the '□' is present in the center of the screen, the subject must react and keypress at the moment of checkerboard reversal onset, ignoring the symbol '○'. This binds the subject attention to the periphery of the screen. This task didn't induce alterations in the SSVEP response when the attention was varied between center and periphery of the screen, so in this case it was only used to bind the subject's attention to the stimulation screen, in order to avoid distractions that can consequently alter the output of the EEG. All the calculations and algorithms exposed in section *3.1) Calibration Techniques* were introduced in *Soares et al* previous research. [15]

3.1.1 Canonical Correlation Analysis

The canonical correlation analysis (CCA) intends to find calibration coefficients for every EEG channel in order to obtain the *Fit* signal that best correlates to the *Photo* signal. [75] The vector *Theta* contains 10 elements that will be multiplied respectively by each EEG channel before the combination. For this purpose, the signals from each channel are incorporated into a matrix, which contains 10 columns (number of channels) and *n* lines (*n* corresponds to the number of data samples) denominated *DataMat*. Various circular shifts are performed in the *Photo* signal in order to cover delays incurred during the trials.

NOTE:

→ **Canonical correlation analysis (CCA)** finds linear combinations of two vectors that have the highest correlation with one another. [75]

→ **Circular shift (CS)** is a cyclic permutation operation that rearranges the elements in a vector, moving the final element of the vector to the top and shifting the other elements to the next index position.

→ For any matrix A, there is only one **pseudo inverse (A^+)** that satisfies the conditions proposed by the definition. Pseudo inverse is a generalization of the inverse (A^{-1}). [76] The pseudo inverse conditions are:

- $AA^+A = A$;
- $A^+AA^+ = A^+$;
- $(AA^+)^* = AA^+$ (A^* is the conjugate transpose of A);
- $(A^+A)^* = A^+A$.

→ **Correlation coefficient (CC)** is a statistical method that evaluates the relation strength between the instantaneous values of two 'moving' variables. The covariance is used in the calculation of the correlation coefficient and relates to the directional relationship between the two variables.

$$\rho_{xy} = \frac{cov(x,y)}{\sigma_x \sigma_y}$$

$$cov(x,y) = \frac{\sum_{i=1}^{n}(x_i - \bar{x})(y_i - \bar{y})}{n-1}$$

where ρ_{xy} and $cov(x,y)$ are the correlation coefficient and covariance representations, respectively, $\bar{x}$ and $\bar{y}$ are the mean values of the variables, σ_x and σ_y are the standard deviation values of the variables and n is the number of samples of the two variables.

For the next calculations, only the middle indices of the vectors are selected to prevent discontinuities caused by the circular shifts. All vectors are normalized to zero (each element is subtracted by the mean ($\bar{x}$) and divided by the standard deviation (σ), as shown in equation 3.1) using the function *zscore()*.

$$Normalization = \frac{x - \bar{x}}{\sigma} \quad (3.1)$$

To obtain the Theta values, the equation 3.2 is used, incorporating a pseudo inverse function *pinv():*

$$Theta = pinv\left(DataMat'_{[20,n]} \times DataMat_{[n,20]}\right) \times DataMat'_{[20,n]} \times SensorSignal_{[n,1]} \quad (3.2)$$

The resulting *Theta* vectors possess calibration coefficients that give the best *Fit* signal correlation for each *Photo* signal shift. So, there is one *Theta* vector with 10 elements (and consequently one *Fit* signal) for each of the *Photo* signal shifts. To evaluate which of the shifts better accounts for the delays, a correlation coefficient calculation is performed for every shift, to select the best correlated shift's correspondent *Theta* vector and *Fit* signal, which corresponds to the signal denominated TBF.

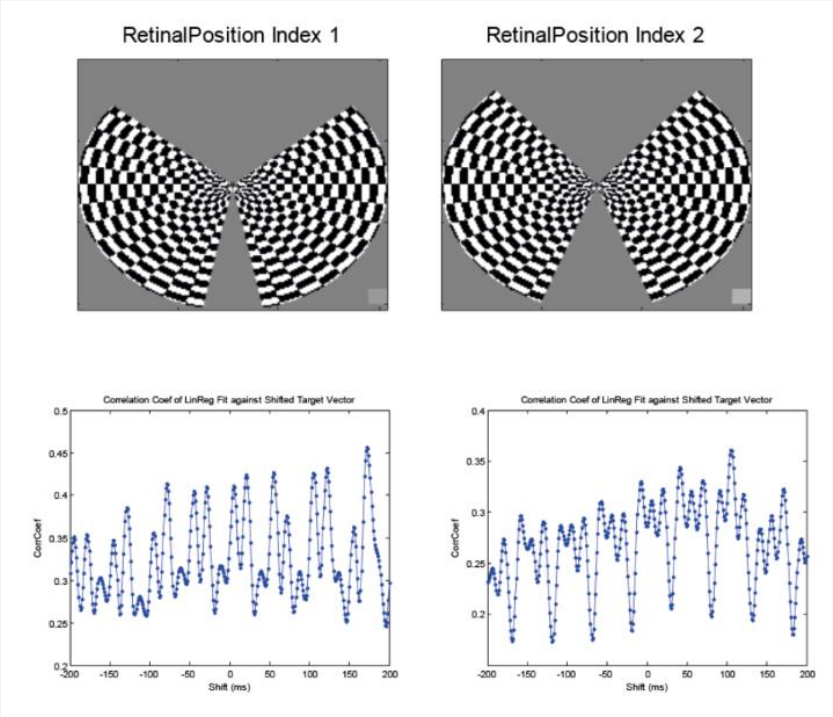

Figure 3.1) Canonical correlation analysis correlation coefficients for two different checkerboard configurations. Coefficient of correlation values (y axis) between the EEG channels combination (*Fit*) and the sensor's signal for every circular shift performed (x axis) for the respective stimulation screen above. Adapted from: *Soares et al.* [15]

3.1.2 Calibration Trials

The calibration prior to experimental trials is composed by two steps: a retinotopic mapping session and a full calibration that consists in two calibration sessions: a first session consisting of CCA at 1000 Hz and a second session consisting of CCA at 20 Hz.

3.1.2.1 Retinotopic Mapping/Calibration

The retinotopic mapping consists in 2 minutes (120 seconds) of 15 different visual stimulation screens sequential presentation (see Figure 3.1) for a total of 8 seconds each, in randomly ordered 1 second periods.

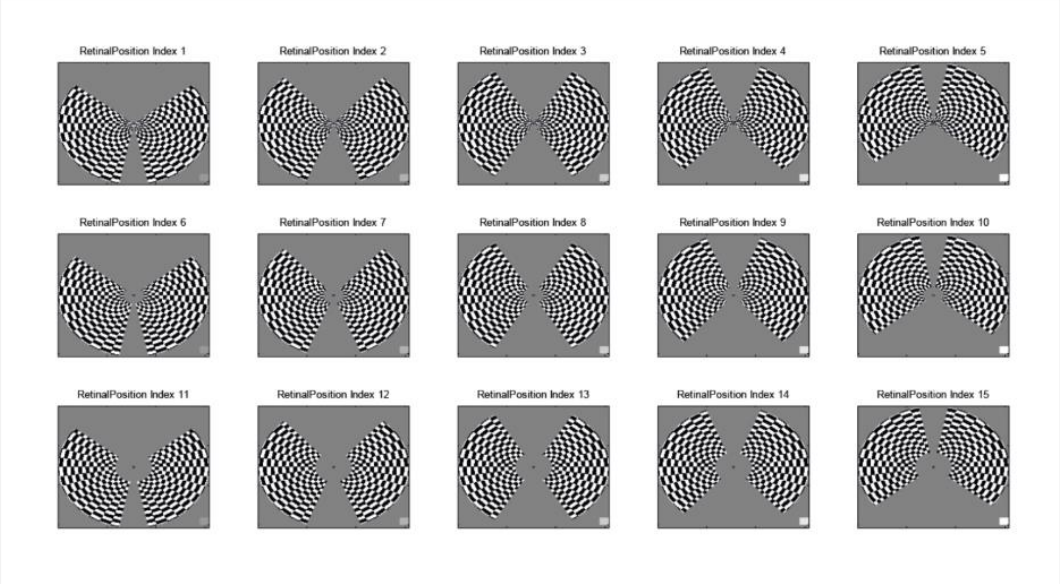

Figure 3.2) Checkerboard configurations available. Fifteen possible checkerboards to be used as visual stimulation screens. In the lower right corner of each panel there is a square which identifies the frame. The light sensor will be placed in the screen directly above the square so it is possible to identify when each frame was presented by means of *Photo* signal analysis. Adapted from: *Soares et al.* [15]

This calibration process ensures which retinal position of the checkerboard presents the most relevant data for each subject. After the 120 second trial, a 1 millisecond resolution CCA is performed using the light sensor signal (*Photo*) as target vector to define each subject most appropriate stimulation checkerboard.

3.1.2.2 Full Calibration

In this session, the stimulation onset is alternated between ON and OFF states. The variable *Contrast* encodes the current stimulation state (ON or OFF), assuming in most cases the values of 0 or 1 (all or nothing) for the OFF set and ON set, respectively. In some representations exposed in this thesis, the absolute value of *Contrast* can acquire different values from the previously referred. What is important is that this variable alternates between two fixed values, the smaller value encoding the OFF state and the higher value the ON state. The ON state corresponds to the presentation of the checkerboard selected in the retinotopic calibration, inverting at 60 Hz between three frames, and the OFF state corresponds to a homogeneous gray screen (see Figure 3.3).

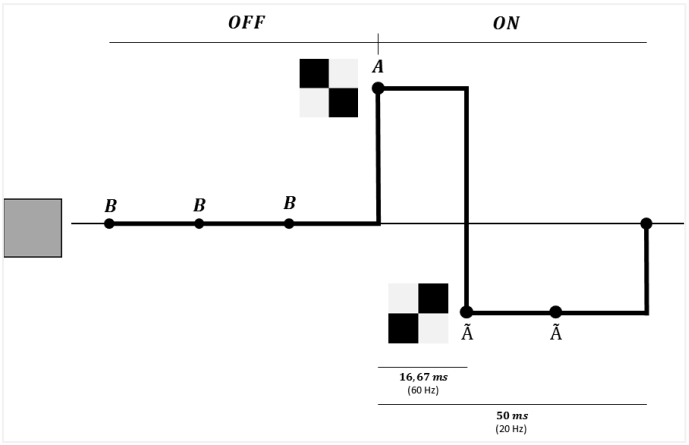

Figure 3.3) Visual stimuli frames representation. Schematic representation of the stimulus delivered in OFF state (frames B) and ON state (frames A and Ã). Both stimulation states (ON and OFF) are delivered in time periods of 50 milliseconds, so between each stimulation decision there are always at least three frames presented.

It is important to verify if the stimulation potentiates the target frequency specific potentials, because a discrepancy between the potentials induced and the algorithms defined frequencies can be damaging to the system development efforts. In this case, EEG recordings verified that the stimulation design presented effectively originates an increase in the 20 Hz SSVEPs amplitude and correspondent harmonics (40 Hz, 60 Hz, …).

The purpose of the first calibration is to obtain the TBF as explained in section *3.1.1) Canonical Correlation Analysis*, with resource to a 1 millisecond resolution CCA (1000 Hz). To perform the second calibration, vectors of 500 TBF signal samples are extracted, with overlaps of 450 samples. As the EEG recording samples at 1000 Hz, the vectors correspond to the latest 500 samples selected at a rate of 20 Hz (intervals of 50 milliseconds between extractions). These vectors are used to perform spectral analysis of the TBF signal. The vectors' power spectral density estimation is obtained using the *pwelch()* function which resorts to the Welch's method. This method is an improvement of common periodogram spectrum estimates, enabling a noise reduction in the power spectrum with frequency resolution sacrifice. The frequency resolution sacrifice is justifiable due to the strong presence of noise in EEG recordings. The frequencies of interest are 20 Hz (fundamental stimulation frequency) and 40 Hz (2nd harmonic of the stimulation frequency).

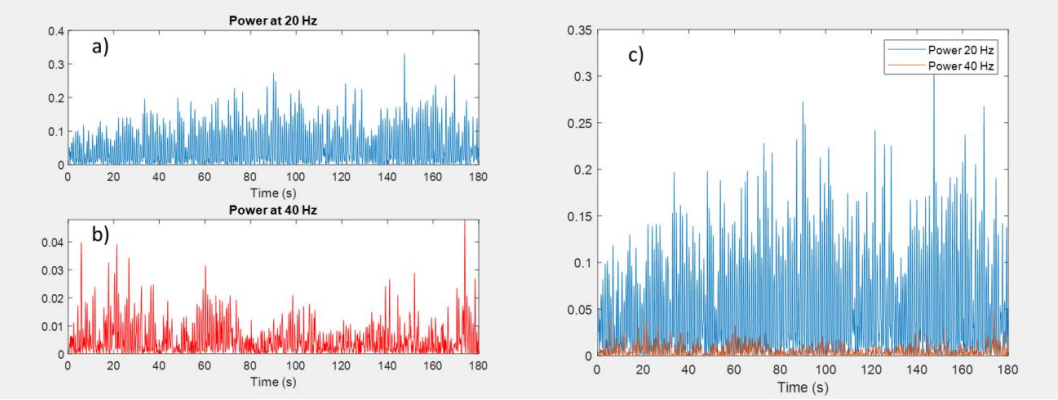

Figure 3.4) SSVEPs power graphics at 20 and 40 Hz oscillation frequencies. Comparison (c) between the magnitudes of the power at 20 Hz (a) versus the power at 40 Hz (b). The power calculation is performed at a rate of 20 Hz and is obtained using the most recent 500 samples of the TBF signal.

The objective is to obtain the instantaneous power at these two frequencies for each of the 500 sample vectors, then perform a CCA with *Contrast* signal circular shifts to find the two frequencies power combination that best correlates with the shifted *Contrast* signal. The resulting frequency power combination that best correlates with the *Contrast* is denominated *Frequency Best Fit* (FBF). The FBF is the project's variable of interest, which relates to the number of synapses activated at the frequency of 20 Hz and the degree of synchronization between the firing patterns of the induced post-synaptic potentials. The FBF is meant to be the control designs' ultimately controlled variable, as it will be shown in further sections of this Chapter.

From this point forward, all the simulations, operations and models built use TBF signals obtained in the available dataset. The FBF will be calculated from the TBF signals and from the output of model's blocks. For the control systems presented in the next sections, the second calibration presented previously will not be performed, so the variable FBF is defined only by the power at 20 Hz in the 500 sample vectors.

3.2 Brain SSVEP Models Estimation

Before developing frequency specific SSVEPs control strategies, it is necessary to obtain models that can faithfully replicate the SSVEPs response to the specific induced type of stimulation. The approach consisted in using the existing stimulation signal (artificially generated accordingly to the frames presented during actual trials)

and SSVEP data as input and output, respectively, to a system estimation algorithm (*System Identification Toolbox*™), so that a calculated mathematical model could respond in a brain similar fashion when presented with a signal correspondent to the visual stimulation presented to subjects in experimental trials. The approximation of brain processes (see sections *2.1.5) Visual Pathway* and *2.2.2) The Steady-State Visual Evoked Potentials*) to LTI systems can possibly show very inaccurate results, because the dynamics involved in the brain's information processing are anything but linear. Yet, the SSVEP responses are characterized, as the denomination SSVEP indicates, as steady-state responses that have very high correlation in amplitude, phase and frequency with the stimulus presented, so the approximation of the processes that originate these responses to LTI oscillatory systems be more reliable than one might expect. SSVEPs are induced through visual stimulation and the goal is to obtain models of the brain's SSVEPs so, given the limited resources, it is not possible to create computational models that receive light stimulus as input. So, one of the challenges is constructing stimulation signals which provoke model's similar reactions to the brain reactions provoked by light stimulus, being the stimulation signals correspondent to the light stimulus.

All the graphics and results in this section refer to the model estimated using the first trial of experimental subject 1 data (model denomination: *tf2040_1_1*), unless otherwise indicated.

3.2.1 Raw & Filtered ON ERPs Approaches to Model Estimation

To calculate models through the existing dataset, the TBF signal was selected to model outputs, since for the purpose of this experiment these are considered the raw output of the EEG. In a first approach, ON and OFF stimulation states corresponding ERPs were calculated and used as system measured output in the *System Identification Toolbox*™ application. The ERPs calculated were composed of 400 samples, so a 400 sample stimulation signal was used as measured input (see Figure 3.5). Only the ERPs for the ON state were used since the OFF state input signal is a constant 0.

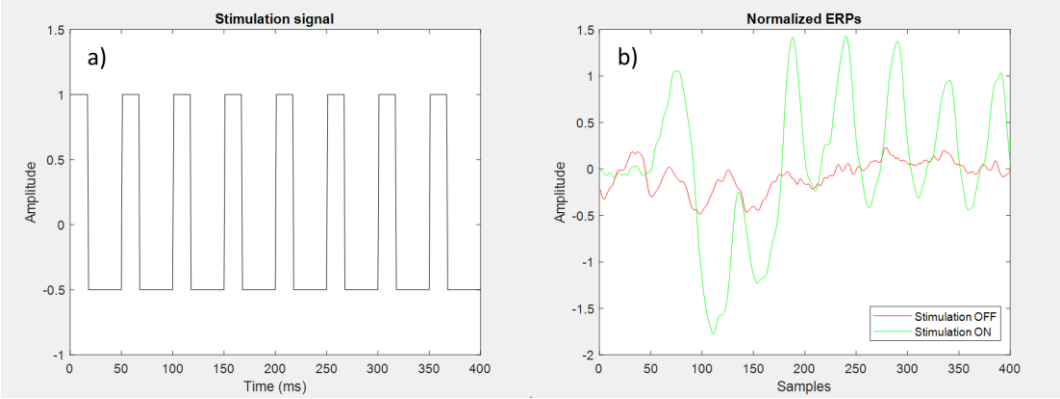

Figure 3.5) Raw TBF signal ERPs and corresponding stimulation. The *System Identification Toolbox*™ requires inputs and outputs with the same number of samples: 400 milliseconds of the stimulation signal were selected (a) to match the ERPs number of samples (b).

In preliminary attempts of calculating models, the TBF was not filtered, possessing all the frequency powers between 1 and 100 Hz, which justifies the noise present in the ERPs (see Figure 3.5b). The same protocol of input/output was used in posterior attempts, with an additional 2nd order Butterworth bandpass filter for the TBF signal, comprising frequencies around 20 and 40 Hz (see Figure 3.6 & 3.7).

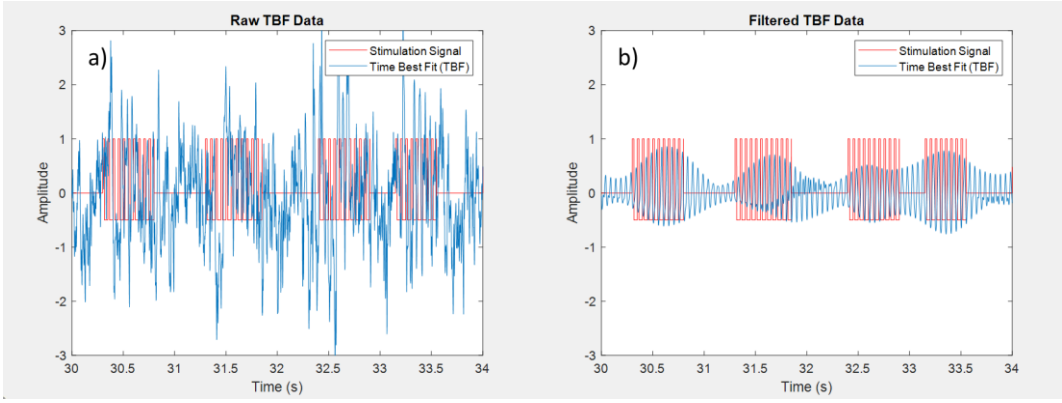

Figure 3.6) Raw & filtered experimental TBF signals. a) Raw TBF signal obtained in experimental trials compared with the stimulation signal presented; b) Filtered TBF signal, comprising only the frequencies of interest (20 & 40 Hz). The filtering enables to obtain more relevant data for models' calculation.

Several models were simulated and the output compared with the ERPs (measured outputs), models which varied in the number of poles and zeros of the transfer function that defines each simulated model.

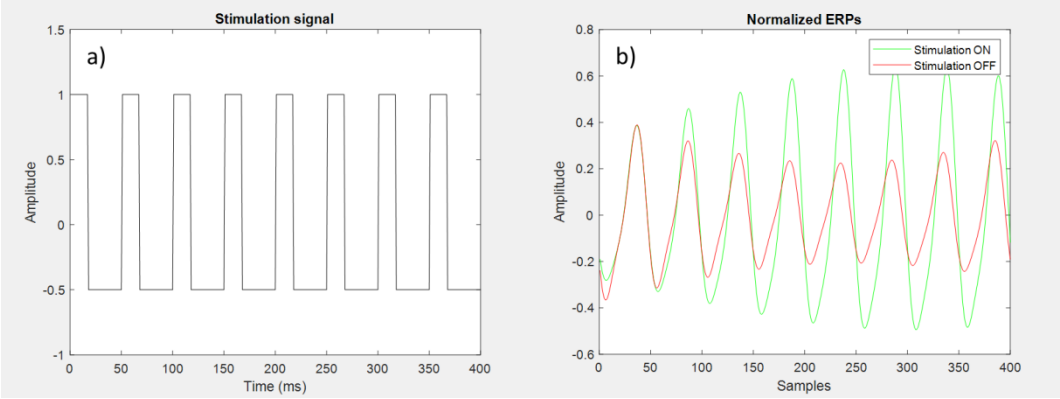

Figure 3.7) Filtered TBF signal ERPs and corresponding stimulation. a) The stimulation signal used as input; b) ERPs calculated using the TBF filtered data. In comparison with the ERPs obtained with the raw data, these show o lot of reduction in noise, having a higher percentage of relevant data.

For these models' estimation, the instrumental variables (IV) initialization method was used, while the *System Identification Toolbox*™ automatically applied the non-linear least squares algorithm (NLLSA) to estimate the LTI transfer functions. The NLLSA is a regression analysis method that approximates non-linear relations between inputs and outputs to a linear model and uses successive iterative processes to rectify the parameters of the approximated linear model. The objective function ($f(x)$) of the NLLSA is represented by an m number of nonlinear auxiliary functions/equations ($f_i(x)$) that correspond to regression residuals resultant from data fitting iterations.

$$\min_x f(x) = \sum_{i=1}^{m} f_i(x)^2 \qquad (3.3)$$

The algorithm minimizes the sum of the auxiliary functions squares (see Equation 3.3), hence the denomination of least squares.

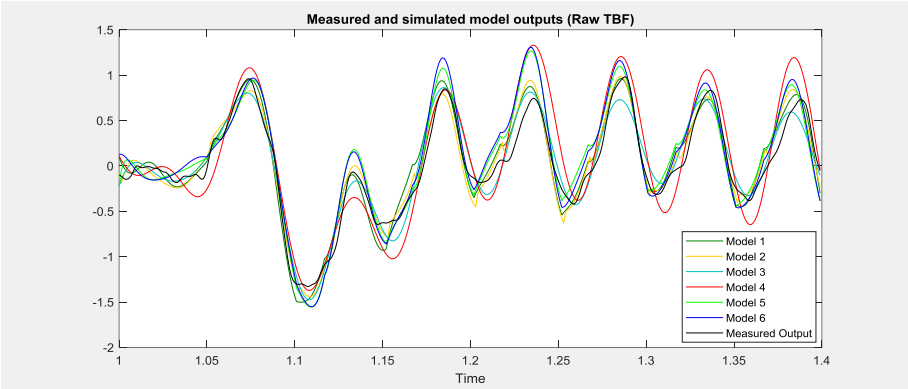

Figure 3.8) Raw TBF signal obtained models output comparison. Measured output (ON ERPs calculated from raw TBF) compared with 6 simulated models' output. The model which showed the best fit to the measured data presented a fit of 76,21 % (11 poles and 11 zeros).

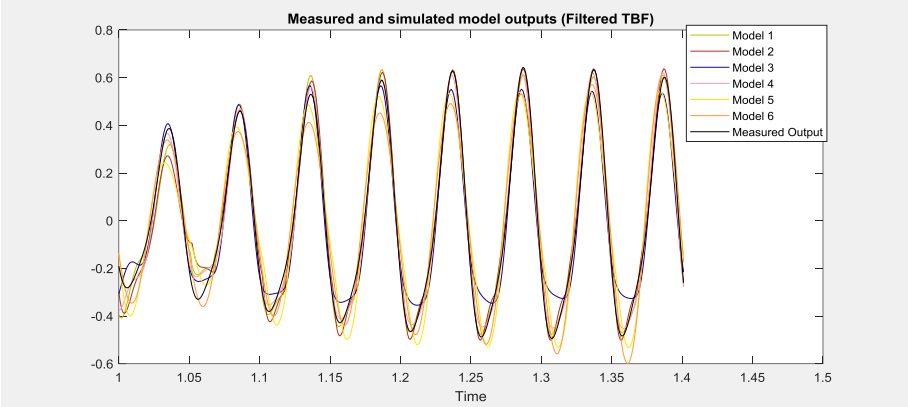

Figure 3.9) Filtered TBF signal obtained models output comparison. Measured output (ON ERPs calculated from filtered TBF) compared with 6 simulated models' output. The model which showed the best fit to the measured data presented a fit of 89,09% (4 poles and 1 zeros).

In Figures 3.8 and 3.9 are represented the estimated models outputs versus the uploaded measured outputs (stimulation ON state ERPs) for the raw and filtered TBF signals, respectively. To validate the estimated models, a *Simulink*™ model was implemented to replicate the database experiments [15] (see Figure 3.10). The simulation has 180 seconds (3 minutes) duration and uses the exact stimulation onset used in the original experiences. The simulated FBF signal calculation is performed both for the 20 & 40 Hz powers combination and for the isolated 20 Hz power. The simulated FBF signals are then compared with the experimental FBF, using a correlation coefficient calculation and visual analysis.

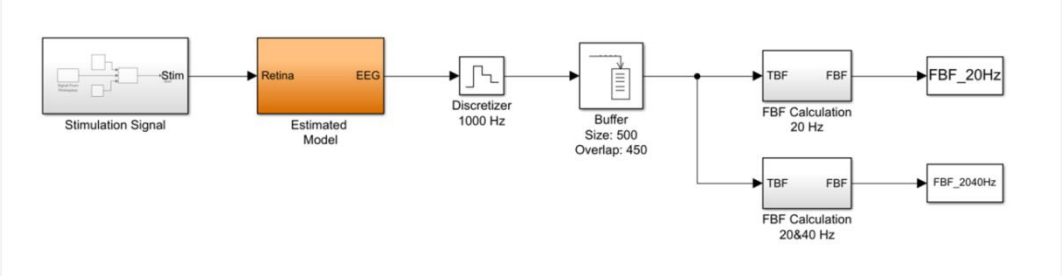

Figure 3.10) Estimated models validation *Simulink*™ scheme. Inclusion a zero-order-hold block to sample the simulation, because the estimated models are continuous time LTI transfer functions and the calculations branch needs to be discrete. The *Buffer* selects the latest 500 samples at every 50 milliseconds (overlap of 450 samples; 20 Hz sampling) to calculate the powers at 20 & 40 Hz. The coefficients used to combine the powers at the two interest frequencies are the same used in experimental trials of *Soares et al.* [15]

Although experiments have shown delays both in the physiological and data transmission mechanisms, the experimental FBF signals are corrected for the observed delays, justifying the validation model non-inclusion of delay blocks. All the following representations of model results concern the first trial of the first experimental subject (Exp1; Trial1) from the database.

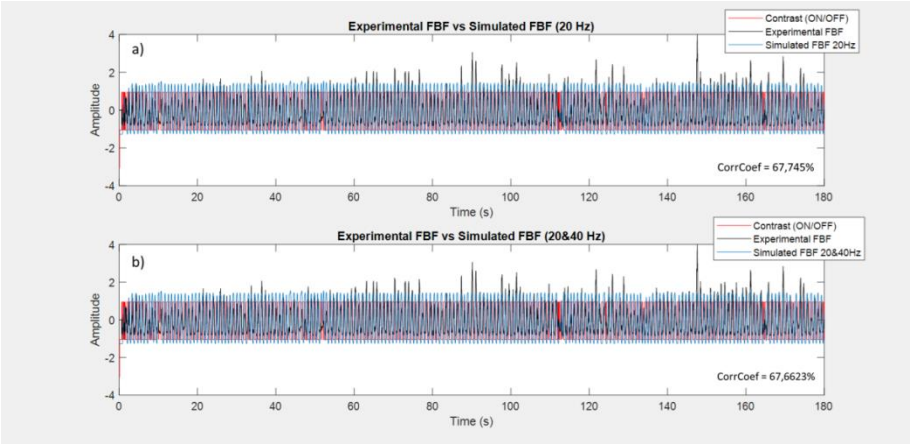

Figure 3.11) Experimental vs simulated FBF variables of the raw TBF signal model. Plotting experimental FBFs (black line) versus simulated FBFs (blue line) for the estimated model using raw TBF data ON state ERPs; a) 20 Hz power FBF signal; b) 20 & 40 Hz combined power FBF signal.

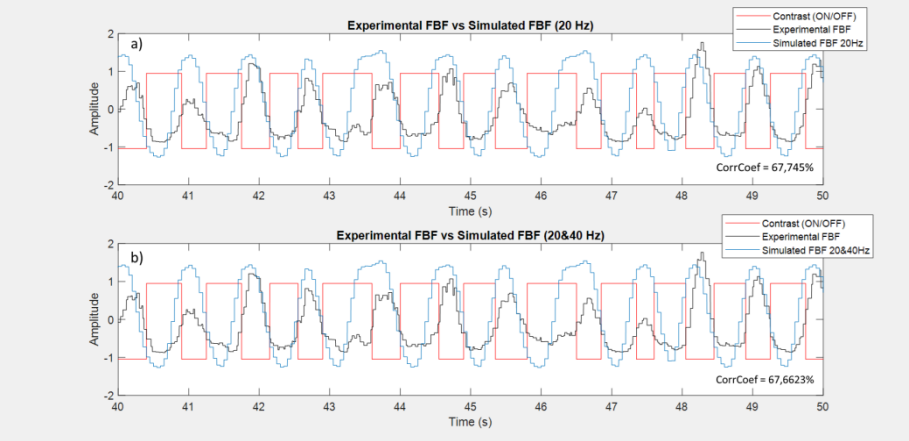

Figure 3.12) Visual inspection of Figure 3.11. Zoom in on Figure 3.11 plots, to perform visual analysis and experimental and simulated FBF comparison.

Analysis results from the models estimated with stimulation ON state ERPs from the raw TBF data present elevated correlation coefficients with the experimental FBF for the simulated 20 Hz power and for the combination of 20 & 40 Hz powers (67,8% and 67,7%, respectively). The correlation coefficient calculation resulting values do not necessarily mean that these models are good replicas of the SSVEP mechanisms in the brain, only that the variation of the two compared values presents an approximated linear correlation. A closer analysis of the plots (see Figures 3.11 and 3.12) reveals very little variation in interest frequencies power amplitude, combined with simulated FBF very repetitive patterns for both FBF power calculation alternatives (20 Hz and 20 & 40 Hz combination).

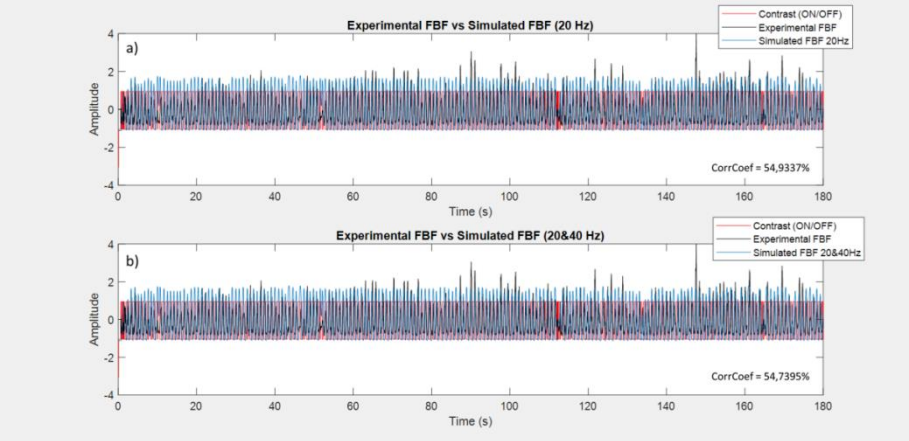

Figure 3.13) Experimental vs simulated FBF variables of the filtered TBF signal model. Plotting experimental FBFs (black line) versus simulated FBFs (blue line) for the estimated model using filtered TBF data ON state ERPs; a) 20 Hz power FBF signal; b) 20 & 40 Hz combined power FBF signal.

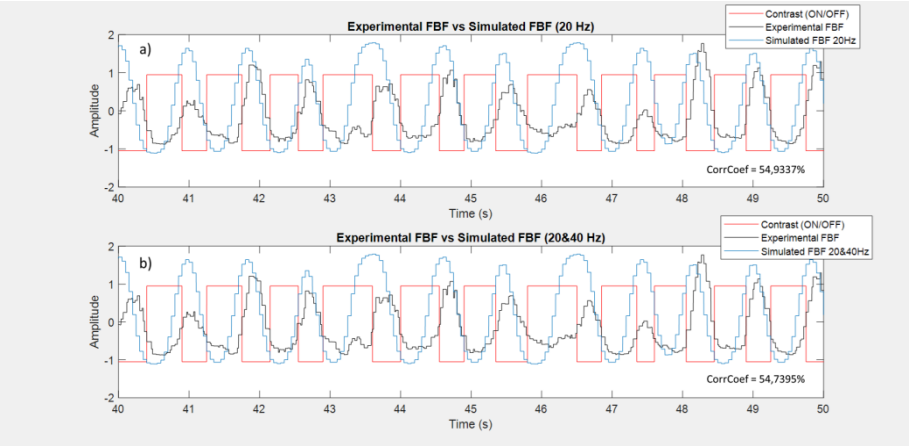

Figure 3.14) Visual inspection of Figure 3.13. Zoom in on Figure 3.13 plots, to perform visual analysis and experimental and simulated FBF comparison.

Analyzing the models estimated with stimulation ON state ERPs from the filtered TBF data, these showed lower correlation values compared to the previous approach (54,9% for 20 Hz; 54,7% for 20 & 40 Hz). The models from this approach showed a little more variability in amplitude, but continue to present repetitive patterns. To better evaluate the performance of the models, the simulated TBF signal was also analyzed (see Figure 3.15).

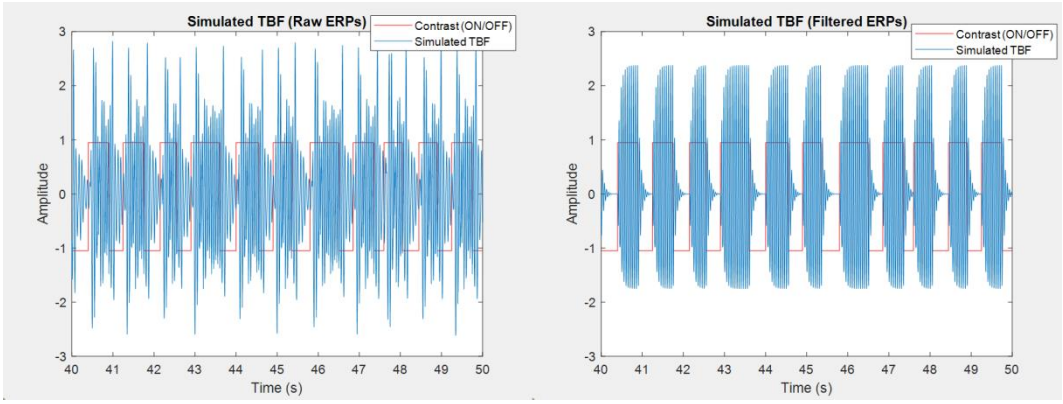

Figure 3.15) Model's TBF response comparison. Simulated TBF variable from raw (left) and filtered (right) ERP estimated models.

The raw ERP estimated model is very noisy (Figure 3.15 (left)), not allowing relevant conclusions about the 20 Hz TBF variable evolution with the stimulation onset. On the other hand, the filtered ERP estimated model (Figure 3.15 (right)) shows a desired power increase in response to stimulation onset, but also presents saturation baselines and an excessively rapid power decrease in response to stimulation offset, not corroborating with power decrease tendencies observed in experimental results (see Figure 3.6b).

The overall results for the two approaches are non-satisfactory. The previous model estimation approaches problems may be related to the solely use of ON ERPs, failing to perform when the stimulation is turned OFF. Such results led to search and study of different protocols to obtain sufficiently reliable SSVEP models.

3.2.2 TBF Reconstruction Approach to Model Estimation

In a new approach to obtain brain SSVEP acceptable models, the objective was to use the ON and OFF ERPs for the purpose of reconstructing the TBF expected reaction to the stimulation onset and offset, respectively. The reconstructed TBF was then used as measured output to estimate models. Better results were expected in comparison to the previous protocol (see section *3.2.1) Raw and Filtered ON ERPs Approaches to Model Estimation*) since this new protocol included the OFF ERPs and comprised uploaded inputs and outputs with more than 400 samples.

The TBF data is firstly filtered (2nd order Butterworth bandpass filter) around the interest frequencies (20 and 40 Hz), 'equipping' the reconstructed signals only with relevant information (see Figure 3.16). Since the background EEG can possess frequencies at 20 and 40 Hz that were not induced by the visual stimulation, the TBF value was set to zero (0) 300 milliseconds after every stimulation offset (see Figure 3.17) to account for background 20 and 40 Hz irrelevant activity.

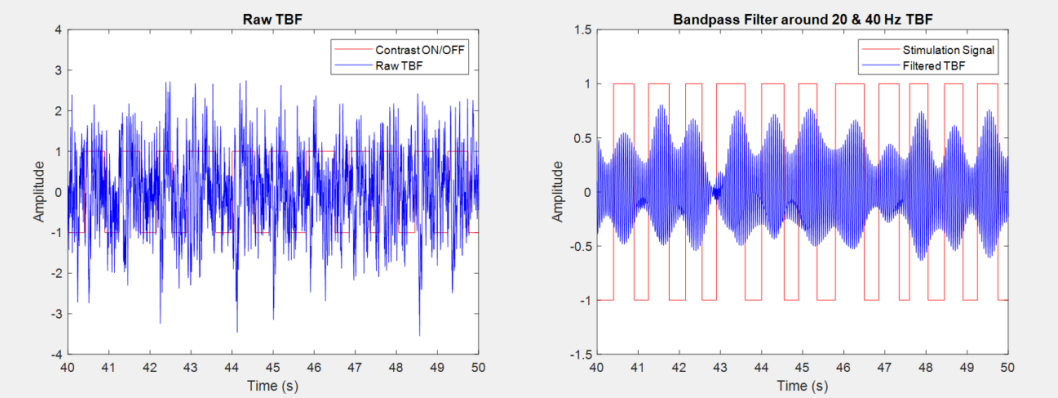

Figure 3.16) Raw vs filtered experimental TBF comparison. Plotting raw TBF signal (left) and bandpass filtered TBF signal (right) versus the *Contrast* signal.

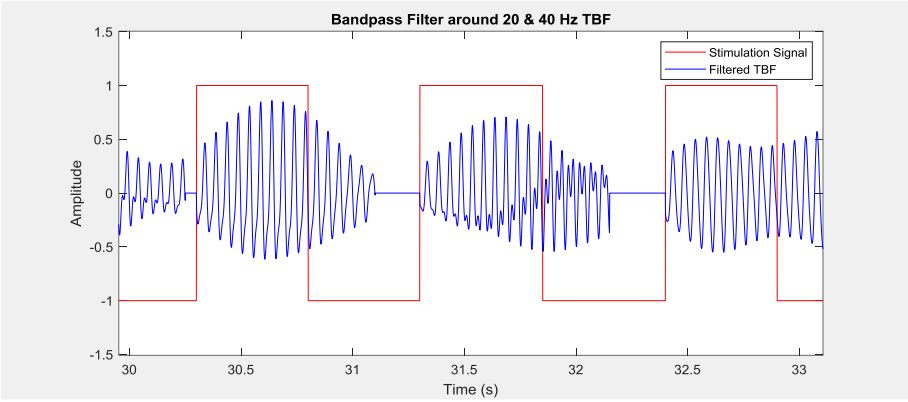

Figure 3.17) Filtered TBF processing. Bandpass filtered TBF signal with value setting to zero (0) 300 milliseconds after stimulation offset.

The resulting processed TBF signal is used to calculate the stimulation onset and offset ERPs (see Figure 3.18) that is later used to estimate the brain SSVEP response.

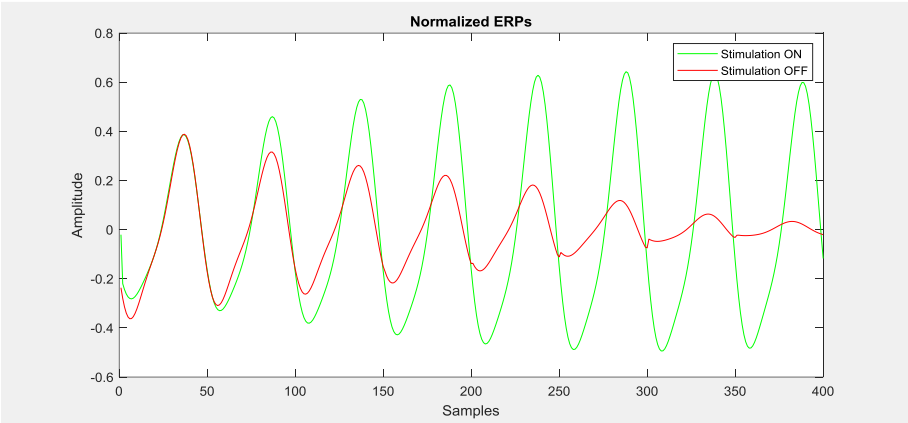

Figure 3.18) ERPs for Figure 3.17 TBF signal. ON and OFF ERPs obtained from the processed TBF signal presented in Figure 3.17.

For the TBF signal reconstruction, a 120 second simulation experiment was performed. A stimulation signal generated for alternating periods of 5 seconds between ON and OFF stimulation states was used as measured input in the estimation algorithm. Later, it was also simulated for alternating periods of 3, 2 and 1 seconds, to evaluate the ON and OFF period's length impact in estimated model's calculations.

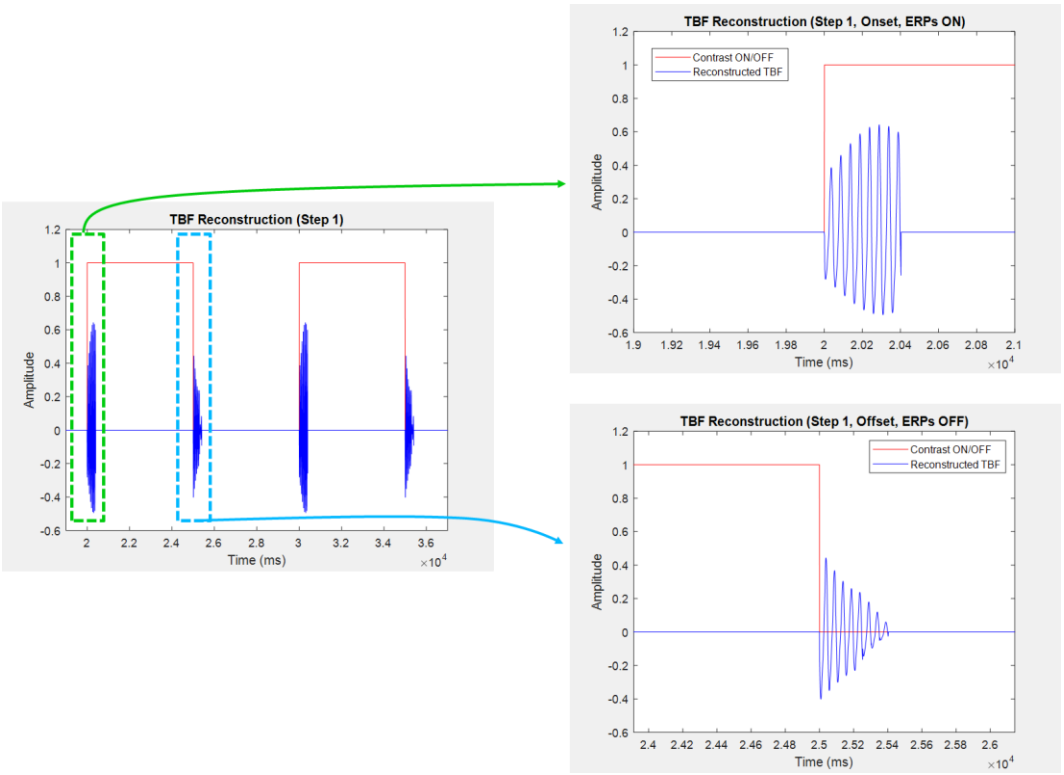

Figure 3.19) TBF signal reconstruction. Combining the stimulation onset and offset with the ON and OFF ERPs, respectively.

The ON ERPs were then expanded for the time course of the *Contrast* signal, thus defining a saturation value for the reconstructed TBF. The reconstructed signal is then put against a corresponding stimulation signal sequence and both signals are uploaded as measured output and input, respectively, in the *System Identification Toolbox*™ application to obtain a TBF reconstructed data LTI transfer function model. In the *System Identification Toolbox*™ app, the IV initialization mode was performed and after some experiments and simulations, the transfer function's number of poles and zeros settings were defined as 4 and 3, respectively (4^{th} order models that showed the best fit percentiles for the reconstructed TBF data). The nonlinear least squares algorithm (NLLSA) was used to calculate estimated model's mathematical equations.

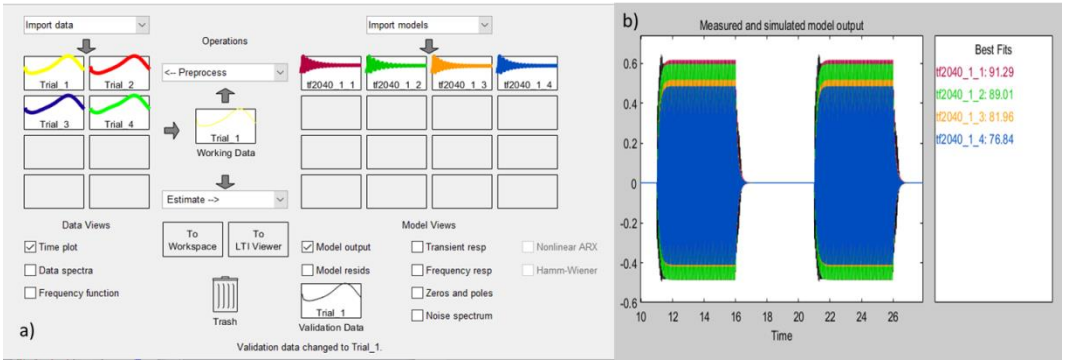

Figure 3.20) ***System Identification Toolbox*™ application interface.** One 4th order model is estimated for each trial of each experimental subject's data. a) 'Trial_n' corresponds to the reconstructed input/output data (left blocks) and 'tf2040_1_n' corresponds to the estimated 4th order LTI models for each trial (right); b) Comparison of the responses presented by each estimated block with the reconstructed TBF signal uploaded as measured output, in the case of this figure the validation data is from 'Trial_1'.

In Figure 3.20 is shown a model estimation protocol example. After Figure 3.20b close examination it's easy to observe that, for this particular experimental subject, the saturation amplitude value decreases throughout experimental trials estimation data. This means that the ERP values used to reconstruct the TBF signal are attenuated in amplitude over time. Such phenomenon can be associated with a certain subject's brain 'adaptation' to the stimulus presented. This variation in results over the trials may occur in different ways for different subjects. The same validation procedure presented in *3.2.1) Raw and Filtered ON ERPs Approaches to Model Estimation* (see Figure 3.10) was used to examine the estimated models robustness and replicative capabilities in comparison to the SSVEP experimentally measured.

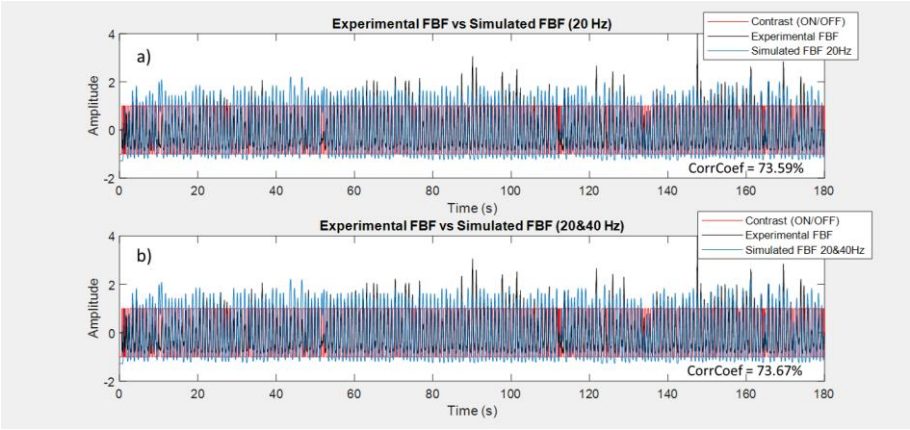

Figure 3.21) Experimental vs simulated FBF variables using the reconstructed TBF estimated model. Plotting experimental FBFs (black line) versus simulated FBFs (blue line) for the reconstructed TBF data estimated model; a) 20 Hz power FBF signal; b) 20 & 40 Hz combined power FBF signal.

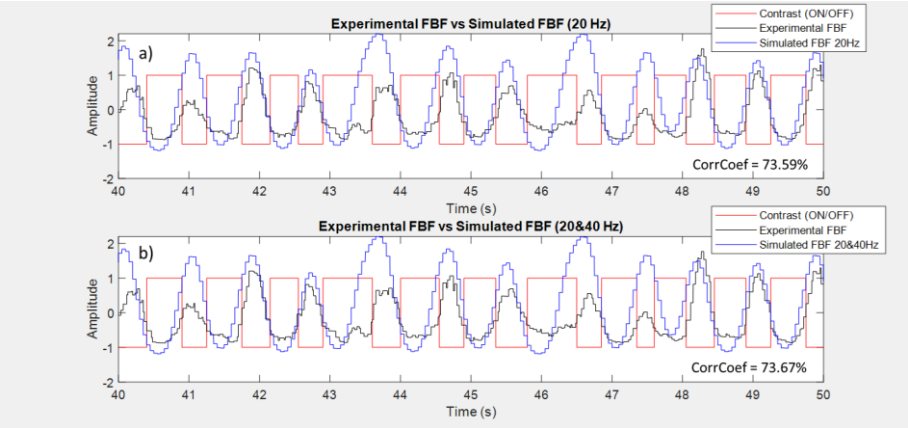

Figure 3.22) Visual inspection of Figure 3.21. Zoom in on Figure 3.20 plots, to perform visual analysis and comparison between experimental and simulated FBF.

When analyzing the new estimated models' FBF response, it is possible to observe more amplitude variability in comparison to the estimated models using the previous section protocol (see *3.2.1) Raw and Filtered ON ERPs Approaches to Model Estimation*). Also, there is an increase in the correlation coefficient values (73,59% and 73,66% for FBF 20 Hz and FBF 20 & 40 Hz, respectively). There are still palpable differences between experimental and modulated responses, probably arising by the fact that the models are linear approximations of a dynamic and nonlinear biological system (brain SSVEP responses). Comparing experimental TBF with simulated TBF, the two present a 84,1% correlation coefficient value, and after visual evaluation of the signals, stands out the stimulus offset power response considerable improvements in comparison to the results obtained for the ON ERPs protocol (see Figure 3.23).

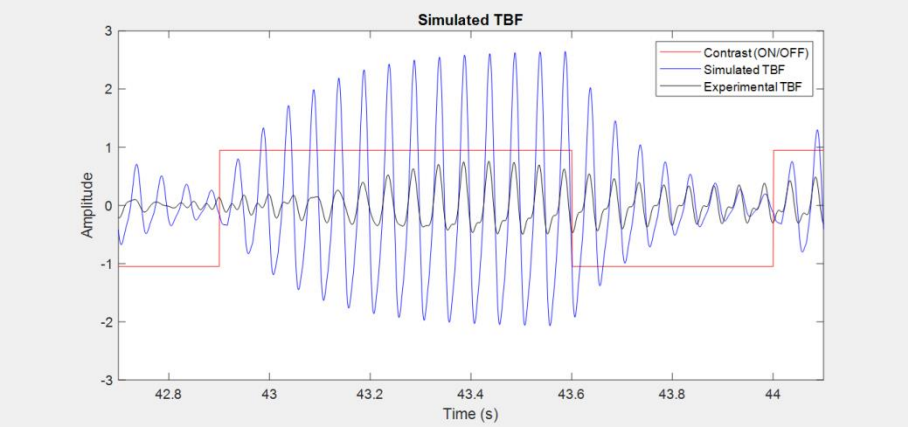

Figure 3.23) Experimental vs simulated TBF variables. Experimental (black line) and simulated (blue line) TBF signals. There is clearly an amplitude difference between the two, but the main focus is the response to the stimulus onset/offset, which shows considerable improvements in comparison with the ON ERPs approach.

Although the protocol does not generate perfect brain SSVEP experimental response models, the validation results observed support the conclusion that the models satisfactorily replicate amplitude variations and responses evoked by stimulation onset/offset, so the control system's implementation models will be obtained following the TBF reconstruction model estimation approach.

3.2.3 Models Validation

Models were estimated for 4 trials of the 10 experimental subject's available data. All the models were subject to validation to inquire which ones are eligible for implementation in control strategies. The validation is performed using the same *Simulink*™ model as presented in section *3.2.1) Raw and Filtered ON ERPs Approaches to Model Estimation* (see Figure 3.10). The criteria defined to select the models that will be subject to control simulations are as follows:

- *Trial number corresponding model that possesses the highest correlation with the respective experimental data for the four TBF signal reconstruction modalities used (5, 3, 2 & 1 second stimulation onset/offset alternating periods);*
- *The models selected using the first criteria must have a minimum of 60% correlation with the experimental data;*
- *After implementation of the first two criteria, one trial number corresponding model is selected for each experiment and for every TBF signal reconstruction modality. The final criteria states:*
  - *focusing on individual experiments, if for the four reconstruction modalities the estimated models trial number selected is the same, then only one model is selected, the one having the highest correlation with experimental data;*
  - *Models corresponding to non-repetitive trial numbers are automatically selected (see Table 3.5).*

In the following tables every model experimental and simulated FBFs correlation values are presented.

Table 3.1) Validation results 1. Correlation coefficient values between experimental and simulated FBF signals using the 5 second stimulation onset/offset alternating periods modality for TBF reconstruction. The two primary selection criteria are implemented in this table: the model presenting the highest correlation coefficient for each experimental subject; the correlation coefficient value of the best model needs to be ≥ 60%. The selected models are highlighted in blue.

Trial Number	Exp 1		Exp 2		Exp 3		Exp 4		Exp 5	
	20 Hz	20&40 Hz	20 Hz	20&40 Hz	20 Hz	20&40 Hz	20 Hz	20&40 Hz	20 Hz	20&40 Hz
1	0,7359	0,7366	0,5556	0,5497	0,5430	0,5432	0,4589	0,4578	0,6324	0,6463
2	0,7317	0,7327	0,6084	0,6017	0,6330	0,6333	0,4509	0,4508	0,4645	0,4683
3	0,6872	0,6884	0,5060	0,4993	0,5957	0,5957	0,1168	0,1154	0,5607	0,5505
4	0,6866	0,6880	0,6212	0,6261	0,6640	0,6644	0,1266	0,1262	0,5736	0,5749
$\bar{x}$	0,7104	0,7114	0,5728	0,5692	0,6089	0,6092	0,2883	0,2876	0,5578	0,5600

Trial Number	Exp 6		Exp 7		Exp 8		Exp 9		Exp 10	
	20 Hz	20&40 Hz	20 Hz	20&40 Hz	20 Hz	20&40 Hz	20 Hz	20&40 Hz	20 Hz	20&40 Hz
1	0,6425	0,6458	0,6262	0,6307	0,4434	0,4421	0,7119	0,7119	0,7117	0,7306
2	0,6962	0,6991	0,6571	0,6620	0,3624	0,3618	0,6759	0,6759	0,7397	0,7588
3	0,6757	0,6786	0,5666	0,5704	0,4534	0,4519	0,6565	0,6564	0,7670	0,7768
4	0,6832	0,6850	0,5815	0,5831	0,5032	0,5018	0,7599	0,7599	0,7380	0,7448
$\bar{x}$	0,6744	0,6771	0,6079	0,6116	0,4406	0,4394	0,7011	0,7010	0,7391	0,7528

Table 3.2) Validation results 2. Correlation coefficient values between experimental and simulated FBF signals using the 3 second stimulation onset/offset alternating periods modality for TBF reconstruction. The two primary selection criteria are implemented in this table: the model presenting the highest correlation coefficient for each experimental subject; the correlation coefficient value of the best model needs to be ≥ 60%. The selected models are highlighted in blue.

Trial Number	Exp 1		Exp 2		Exp 3		Exp 4		Exp 5	
	20 Hz	20&40 Hz	20 Hz	20&40 Hz	20 Hz	20&40 Hz	20 Hz	20&40 Hz	20 Hz	20&40 Hz
1	0,6988	0,7001	0,5554	0,5489	0,5439	0,5441	0,4591	0,458	0,6330	0,6467
2	0,7312	0,7323	0,6088	0,6015	0,6338	0,6341	0,4509	0,4508	0,4649	0,4689
3	0,6869	0,6881	0,5145	0,5086	0,5968	0,5967	0,1162	0,1151	0,5549	0,5449
4	0,6859	0,6873	0,6218	0,6259	0,6650	0,6654	0,1383	0,1381	0,5614	0,5651
$\bar{x}$	0,7007	0,7020	0,5751	0,5712	0,6099	0,6101	0,2911	0,2905	0,5536	0,5564

Trial Number	Exp 6		Exp 7		Exp 8		Exp 9		Exp 10	
	20 Hz	20&40 Hz	20 Hz	20&40 Hz	20 Hz	20&40 Hz	20 Hz	20&40 Hz	20 Hz	20&40 Hz
1	0,6415	0,6448	0,6256	0,6301	0,4444	0,4431	0,7115	0,7115	0,7134	0,7322
2	0,6953	0,6982	0,6565	0,6614	0,3643	0,3636	0,4181	0,4181	0,7411	0,7600
3	0,6749	0,6779	0,5661	0,5700	0,4550	0,4534	0,6555	0,6555	0,7689	0,7787
4	0,6823	0,6841	0,5807	0,5823	0,5056	0,5043	0,7563	0,7563	0,7397	0,7466
$\bar{x}$	0,6735	0,6763	0,6072	0,6110	0,4423	0,4411	0,6354	0,6354	0,7408	0,7544

Table 3.3) Validation results 3. Correlation coefficient values between experimental and simulated FBF signals using the 2 second stimulation onset/offset alternating periods modality for TBF reconstruction. The two primary selection criteria are implemented in this table: the model presenting the highest correlation coefficient for each experimental subject; the correlation coefficient value of the best model needs to be ≥ 60%. The selected models are highlighted in blue.

Trial Number	Exp 1		Exp 2		Exp 3		Exp 4		Exp 5	
	20 Hz	20&40 Hz	20 Hz	20&40 Hz	20 Hz	20&40 Hz	20 Hz	20&40 Hz	20 Hz	20&40 Hz
1	0,7003	0,7016	0,5562	0,5492	0,5451	0,5453	0,4599	0,4587	0,6343	0,6475
2	0,7324	0,7334	0,6100	0,6023	0,6349	0,6351	0,4512	0,4510	0,4658	0,4696
3	0,6884	0,6897	0,5161	0,5097	0,5983	0,5982	0,1167	0,1159	0,5491	0,5394
4	0,6875	0,6888	0,6233	0,6267	0,6664	0,6668	0,1227	0,1218	0,5534	0,5495
$\bar{x}$	0,7022	0,7034	0,5764	0,5720	0,6112	0,6114	0,2876	0,2869	0,5507	0,5515
Trial Number	**Exp 6**		**Exp 7**		**Exp 8**		**Exp 9**		**Exp 10**	
	20 Hz	20&40 Hz	20 Hz	20&40 Hz	20 Hz	20&40 Hz	20 Hz	20&40 Hz	20 Hz	20&40 Hz
1	0,6432	0,6465	0,6272	0,6316	0,4417	0,4401	0,7122	0,7122	0,7157	0,7343
2	0,6966	0,6994	0,6581	0,6629	0,3640	0,3627	0,4261	0,4261	0,7430	0,7619
3	0,6772	0,6800	0,5679	0,5716	0,4536	0,4519	0,6555	0,6554	0,7715	0,7813
4	0,6843	0,6861	0,5825	0,5841	0,4861	0,4845	0,7562	0,7562	0,7423	0,7493
$\bar{x}$	0,6753	0,6780	0,6089	0,6126	0,4364	0,4348	0,6126	0,6126	0,7431	0,7567

Table 3.4) Validation results 4. Correlation coefficient values between experimental and simulated FBF signals using the 1 second stimulation onset/offset alternating periods modality for TBF reconstruction. The two primary selection criteria are implemented in this table: the model presenting the highest correlation coefficient for each experimental subject; the correlation coefficient value of the best model needs to be ≥ 60%. The selected models are highlighted in blue.

Trial Number	Exp 1		Exp 2		Exp 3		Exp 4		Exp 5	
	20 Hz	20&40 Hz	20 Hz	20&40 Hz	20 Hz	20&40 Hz	20 Hz	20&40 Hz	20 Hz	20&40 Hz
1	0,7071	0,7083	0,5650	0,5554	0,5501	0,5503	0,4671	0,4659	0,6402	0,6512
2	0,7375	0,7385	0,6179	0,6084	0,6389	0,6391	0,4402	0,4398	0,4281	0,4239
3	0,6953	0,6965	0,5249	0,5169	0,6040	0,6039	0,1074	0,1057	0,5156	0,5074
4	0,6980	0,6991	0,6314	0,6326	0,6729	0,6732	0,1173	0,1166	0,5283	0,5260
$\bar{x}$	0,7095	0,7106	0,5848	0,5783	0,6165	0,6166	0,2830	0,2820	0,5281	0,5271
Trial Number	**Exp 6**		**Exp 7**		**Exp 8**		**Exp 9**		**Exp 10**	
	20 Hz	20&40 Hz	20 Hz	20&40 Hz	20 Hz	20&40 Hz	20 Hz	20&40 Hz	20 Hz	20&40 Hz
1	0,6513	0,6543	0,6337	0,6379	0,3556	0,3541	0,6599	0,6598	0,7250	0,7426
2	0,7031	0,7058	0,6644	0,6690	0,3041	0,3027	0,6746	0,6745	0,7520	0,7698
3	0,6869	0,6895	0,5747	0,5781	0,3636	0,3620	0,6513	0,6511	0,7835	0,7921
4	0,6930	0,6946	0,5898	0,5912	0,4207	0,4193	0,7481	0,7480	0,7557	0,7615
$\bar{x}$	0,6836	0,6861	0,6157	0,6191	0,3610	0,3595	0,6835	0,6834	0,7541	0,7665

After analyzing the results, (see Tables 3.1, 3.2, 3.3 and 3.4) we found that only the 4th and 8th experimental subject's data did not provide satisfactory results. This can be related to problems in these two experimental data-sets. For all the other experimental trials, the results are much better than might have been originally expected for such a simple modulation protocol. In terms of reconstruction modalities used (5, 3, 2 & 1 second stimulation onset/offset alternating periods), all showed much approximated results, with the '1 second' modality standing out. This can be related to the stimulation patterns presented in the experiments, which may be more approximated to 1 second differences between stimulation onsets and offsets. It can also be related to the reconstructed TBF shorter saturation periods, which are reduced with the onset/offset alternation time period reduction.

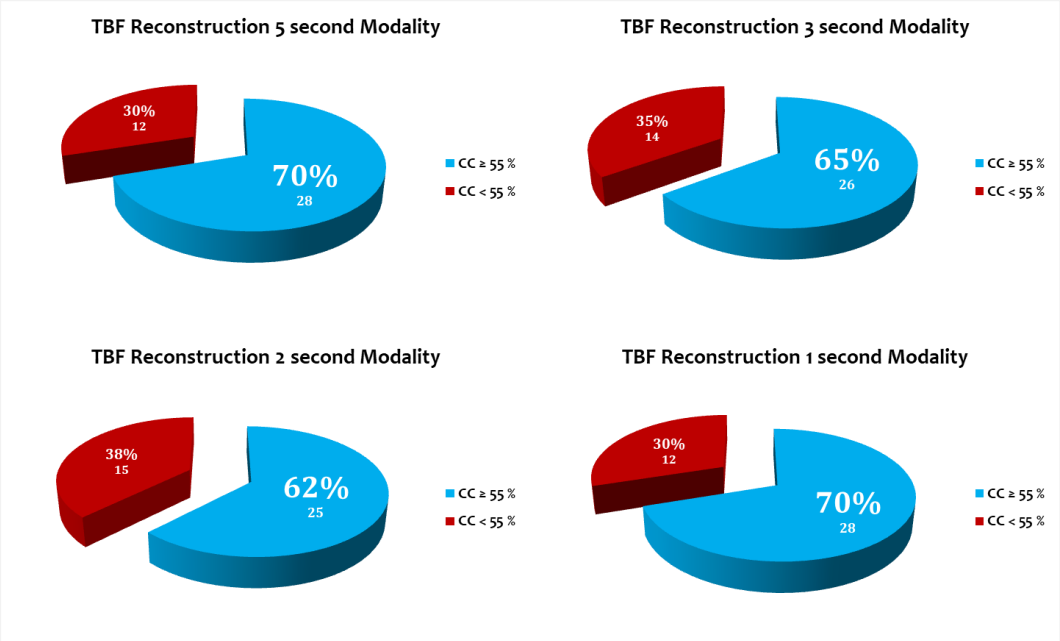

Figure 3.24) Models validation results. Model percentiles and absolute quantity numbers (blue) which showed experimental data correlation coefficient (CC) values ≥ 55% and < 55%. These results were obtained for all the experimental data, including experiences 4 and 8 which make up for 66.67%, 57.14%, 53.33% and 66.67% of the refused models (red) for the 5, 3, 2 and 1 second modalities, respectively.

The accepted models selection is made using the third selection criteria (see Table 3.5) before implementation in control systems.

Table 3.5) Estimated models selection for control system simulations. Estimated model's trial numbers for each experience (rows), each TBF reconstruction modality and correspondent correlation values with experimental data (columns). In this table the third and final selection criteria is applied. The models selected for posterior control implementation and testing are highlighted in green.

Experience Number	Trial #'s (5 second)	CorrCoef 20&40 Hz (%)	Trial #'s (3 second)	CorrCoef 20&40 Hz (%)	Trial #'s (2 second)	CorrCoef 20&40 Hz (%)	Trial #'s (1 second)	CorrCoef 20&40 Hz (%)
1	1	73.66	2	73.23	2	73.34	2	73.85
2	4	62.61	4	62.59	4	62.67	4	63.26
3	4	66.44	4	66.54	4	66.68	4	67.32
4	NaN	-	NaN	-	NaN	-	NaN	-
5	1	64.63	1	64.67	1	64.75	1	65.12
6	2	69.91	2	69.82	2	69.94	2	70.58
7	2	66.20	2	66.14	2	66.29	2	66.90
8	NaN	-	NaN	-	NaN	-	NaN	-
9	4	75.99	4	75.89	4	75.62	4	74.80
10	3	77.68	3	77.87	3	78.13	3	79.21

There are very slight differences between the models obtained using the four TBF reconstruction modalities, with TBF reconstruction '1 second' modality models standing out in terms of correlation percentiles. Even so, the correlation values and responsive behavior to stimulation differences are very faint for all four cases, meaning that satisfactory models can be obtained for the majority of subjects, 80% in the case of the used database experimental subjects. The models to be used are defined by their transfer functions (see Table 3.6).

Table 3.6) Estimated models selected characteristics. Selected model's denominations, respective transfer functions and percentile fit to the TBF reconstruction data uploaded to *System Identification Toolbox*™ application.

Models Selected (Denomination)	Transfer Functions (Continuous Time)	Fit to Reconstruction Data
tf2040_1_1	$\frac{-8.625\,s^3 + 464.2\,s^2 - 5.064e05\,s - 1.521e07}{s^4 + 26.63\,s^3 + 8.043e04\,s^2 + 1.072e06\,s + 1.032e09}$	88.24 %
tf2040_9_4	$\frac{14.89\,s^3 + 2450\,s^2 + 4.235e05\,s + 3.303e05}{s^4 + 363\,s^3 + 2.098e04\,s^2 + 5.566e06\,s + 5.994e05}$	87.30 %
tf2040_1_2_1s	$\frac{-9.096\,s^3 + 410.5\,s^2 - 5.777e05\,s - 1.669e07}{s^4 + 28.98\,s^3 + 7.881e04\,s^2 + 1.182e06\,s + 9.995e08}$	83.95 %
tf2040_2_4_1s	$\frac{9.809\,s^3 + 1217\,s^2 + 3.153e05\,s + 2.777e07}{s^4 + 24.2\,s^3 + 7.97e04\,s^2 + 9.335e05\,s + 1.018e09}$	81.55 %
tf2040_3_4_1s	$\frac{-0.5485\,s^3 - 1662\,s^2 + 1.783e04\,s - 7.607e07}{s^4 + 24.07\,s^3 + 7.99e04\,s^2 + 1.005e06\,s + 1.02e09}$	84.55 %
tf2040_5_1_1s	$\frac{1.184\,s^3 + 1987\,s^2 + 3.962e05\,s + 9.108e07}{s^4 + 39.58\,s^3 + 7.885e04\,s^2 + 1.782e06\,s + 1.009e09}$	75.67 %

tf2040_6_2_1s	$\frac{-6.238\,s^3 + 598.4\,s^2 - 5.333e05\,s + 3.355e07}{s^4 + 29.56\,s^3 + 7.902e04\,s^2 + 1.384e06\,s + 9.931e08}$	79.62 %
tf2040_7_2_1s	$\frac{-4.134\,s^3 + 208.9\,s^2 - 4.899e05\,s - 8.608e06}{s^4 + 28.57\,s^3 + 7.873e04\,s^2 + 1.195e06\,s + 9.864e08}$	84.61 %
tf2040_10_3_1s	$\frac{8.456\,s^3 - 4048\,s^2 + 4.451e05\,s - 1.355e08}{s^4 + 28.12\,s^3 + 7.997e04\,s^2 + 1.201e06\,s + 1.029e09}$	80.81 %

3.3 Control System Design

After obtaining brain SSVEPs response replicative models, the following objective was to simulate real-life approximated experimental conditions and limitations in control models to proof that it is possible to stabilize the output of the replicated models. In this section, several approaches to control design will be exposed together with problems faced, limitations and simulation results. All the representative graphics and results in this section refer to the model estimated using the first trial of experimental subject 1 data (model denomination: *tf2040_1_1*), unless otherwise indicated. If it is not possible to stabilize the output of estimated LTI systems with approximated conditions to the experimental setup, than surely is not possible to stabilize the output of the brain real SSVEP responses. On the other hand, it may be possible to stabilize the output of the LTI systems. But if these do not faithfully replicate brain responses in real time closed-loop, then probably it can be very complex to stabilize a human brain SSVEPs. Anyways, the proof that these estimated LTI systems can be stabilized, or partially stabilize will serve as required condition to perform human experiments using the control designs developed.

3.3.1 PID Control Design

The Proportional-Integrative-Derivative controller design is one of the simplest approaches to control system implementation, so it was the trivial first choice to test the control of the estimated models (see section 2.3.2.1) *PID Controller* for more detailed information about the PID controller). Figure 3.25 shows the *Simulink*™ PID control model used for testing.

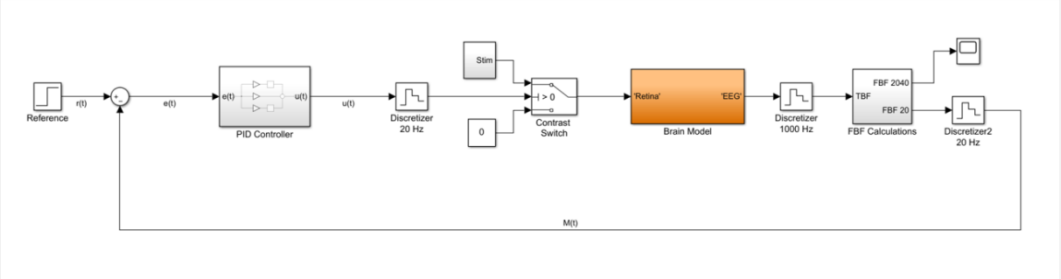

Figure 3.25) PID controller design *Simulink*™ model. In the scheme stands out the *contrast switch*, responsible for the stimulation onset & offset, which output is controlled by the control variable *u(t)* input. The system possesses two sampling rates (20 Hz and 1 kHz) defined by the zero-order-hold blocks, both used as *discretizers*.

For the control design, was included a *contrast switch* responsible for the stimulation onset & offset, which output is controlled by the control variable *u(t)* input, zero-order-hold blocks acting as *discretizers* with sampling rates of 20 and 1000 Hz to define two sampling rates within the system (for the FBF calculation and EEG sampling, respectively), a FBF calculation block composed by the signal 500 sample selector buffer and *Matlab*™ functions to calculate the 500 sample windows frequency specific powers (20 Hz and 20 & 40 Hz combination). A fixed transport delay of 55 milliseconds is introduced in the model to approximate the physiological delays observed experimentally. To test the system, 10 second simulations were performed, reference value *r(t)* and the PID tunings (proportional, integrative and derivative gains) were altered between simulations. The FBF variable was constantly monitored (see PID results in Figures 3.26, 3.27 & 3.28).

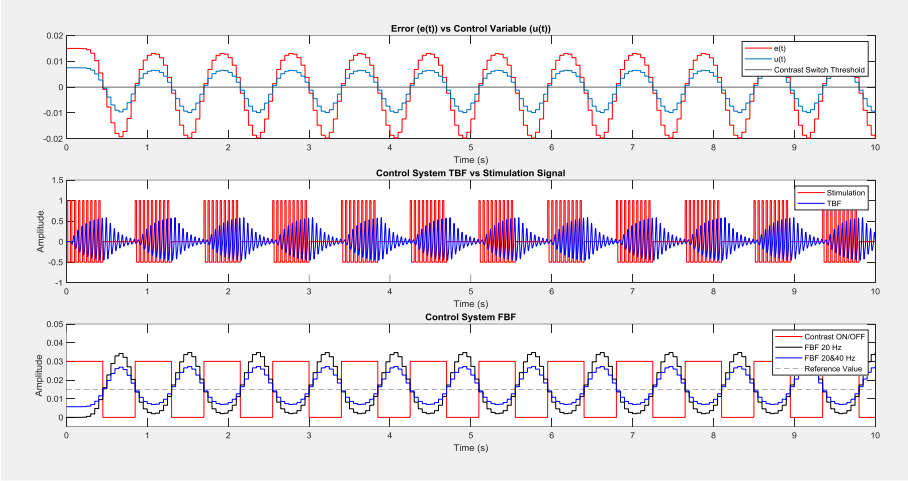

Figure 3.26) PID control design results 1. Variables *e(t)* and *u(t)* values (top), simulated TBF variation with the stimulation signal (middle), and FBF variable vs *contrast* signal (bottom). Reference value =0,015; Proportional gain =0.5; Integrative gain =0; Derivative gain =0;

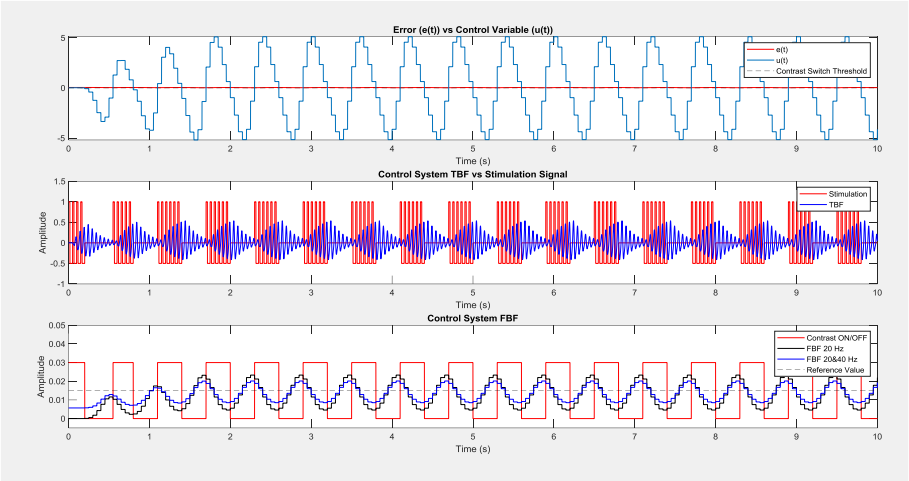

Figure 3.27) PID control design results 2. Variables *e(t)* and *u(t)* values (top), simulated TBF variation with the stimulation signal (middle), and FBF variable vs *contrast* signal (bottom). Reference value =0,015; Proportional gain =0.5; Integrative gain =0; Derivative gain =1;

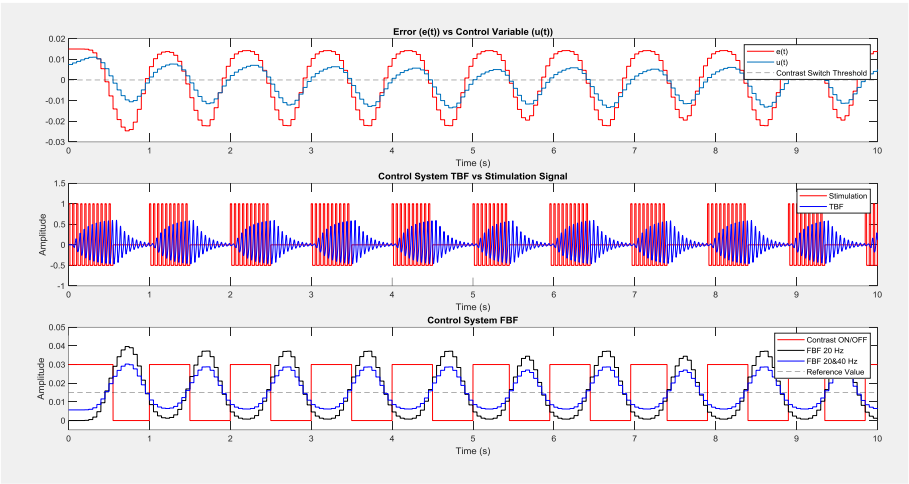

Figure 3.28) PID control design results 3. Variables *e(t)* and *u(t)* values (top), simulated TBF variation with the stimulation signal (middle), and FBF variable vs *contrast* signal (bottom). Reference value =0,015; Proportional gain =0.5; Integrative gain =1; Derivative gain =0;

Reference value and PID gains variation did not show improvements in the FBF variable control. The FBF variable followed a tendency already observed in *Soares et al* experimental results, [15] namely ~1 Hz FBF oscillations. A reference value increase provoked increase of FBF oscillatory variable maximum amplitude value, making no difference for the control purpose (Figure 2.29).

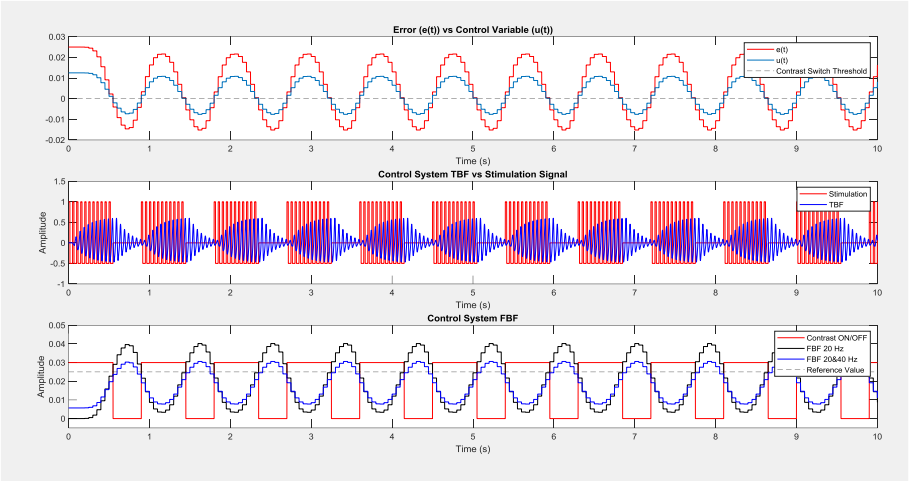

Figure 3.29) PID control design results 4. Variables *e(t)* and *u(t)* values (top), simulated TBF variation with the stimulation signal (middle), and FBF variable vs *contrast* signal (bottom). Reference value =0,025; Proportional gain =0.5; Integrative gain =0; Derivative gain =0;

A ~125 milliseconds delay was measured in *Soares et al* experimental trials, [15] due to data transfer between EEG amplifier and signal analysis computer. Once there is no absolute certainty about this control design delay magnitude, several delays were tested in system simulations (Figure 3.29). The results were worrying because the system remained unstable throughout all the simulation length, even in the absence of delays.

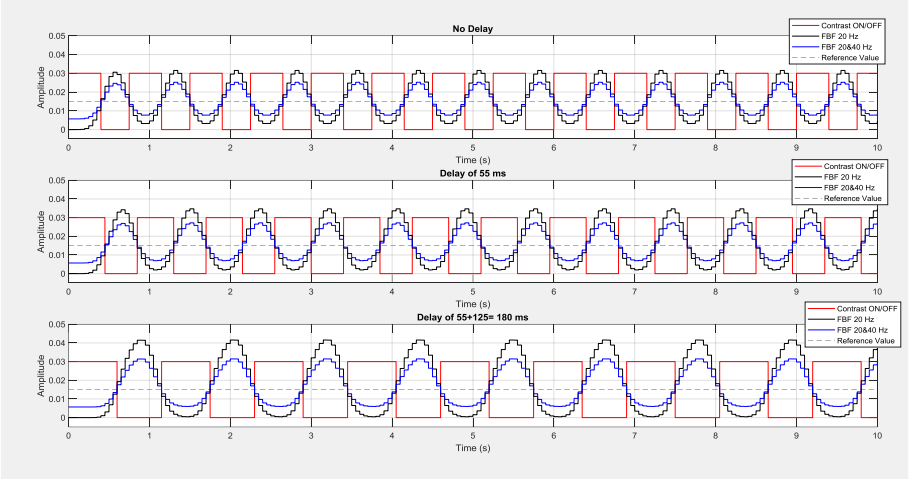

Figure 3.30) PID control design delay variation results. FBF outputs comparison for different system enforced transport delays. The system remains unstable even when there is no in loop delay. Reference value =0.015; Proportional gain =0.5; Integrative gain =0; Derivative gain =0;

The instability observed even in the absence of delays can be due to delays provoked by the FBF calculations. This assumption will be put to the test in following simulations, comprising different control system designs. A stand-alone PID controller is a very simplistic method to control process outputs, therefore is very vulnerable to disturbances, delays and non-linear components. After system analysis (see Figure 3.25), it is possible to infer that the *contrast switch* is a non-linear behavior inductor in the system, not allowing the control variable *u(t)* to act directly as a process input. This means the PID tuning turns out to be somehow irrelevant for the FBF variable control, being the *contrast switch* the main controller of the system (all or nothing control). This experimental setup limitation is bounded with visual stimulation mechanisms, where the stimulation is performed by a flickering screen and not directly by a controller outputted signal. Also, the stand-alone PID controller design does not consider delays incurred in loop (55 millisecond transport delay to account for physiological pathways and not calculated delays incurred in the FBF calculations). The stand-alone PID simulation trials were considered very important to understand the roles and limitations of the system components when placed in a control loop, thus working as starting point to the design approaches that followed.

3.3.2 Smith-Predictor Control Design

To bypass the delays present in loop, the solution was the implementation of a Filtered Smith-predictor (FSP) control design. The FSP places the real process in an outer loop and a real process model LTI system in an inner loop, to isolate delays measured in the real process. For more detailed information about the FSP controller see section 2.3.2.2) *Smith-Predictor Controller*. The *Simulink*™ FSP control model used for testing is represented in Figure 3.31.

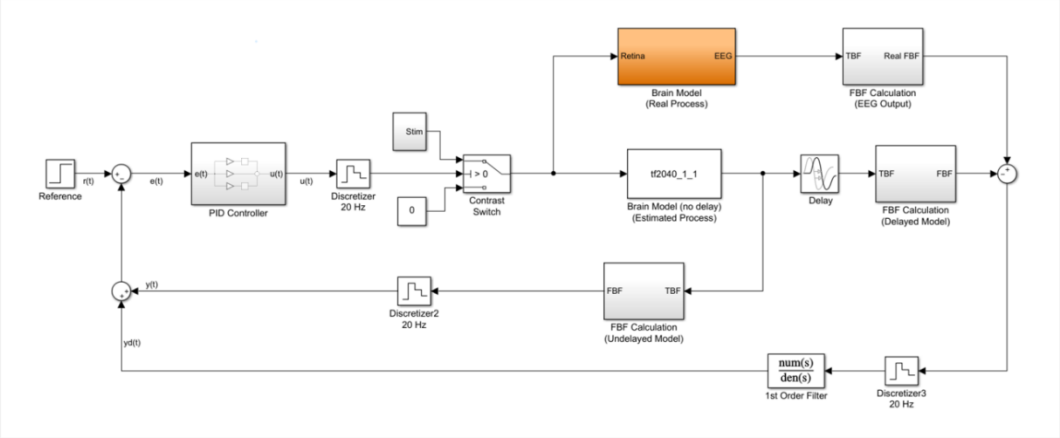

Figure 3.31) FSP control design *Simulink*™ model. The model possesses two summed feedback loops: one containing the real process; the other a real process estimated model (experimental setup).

For the simulations, the real process and the model are exactly the same. In both blocks is to be used the estimated models selected in section *3.2.3) Models' Validation*, so the FSP control system (see Figure 3.31) can be considered as in ideal condition simulation. Given that the controller is mostly the *contrast switch* (all or nothing control), the PID only possesses a proportional gain of 1, which means that the variables *e(t)* and *u(t)* are equal over the simulation time course.

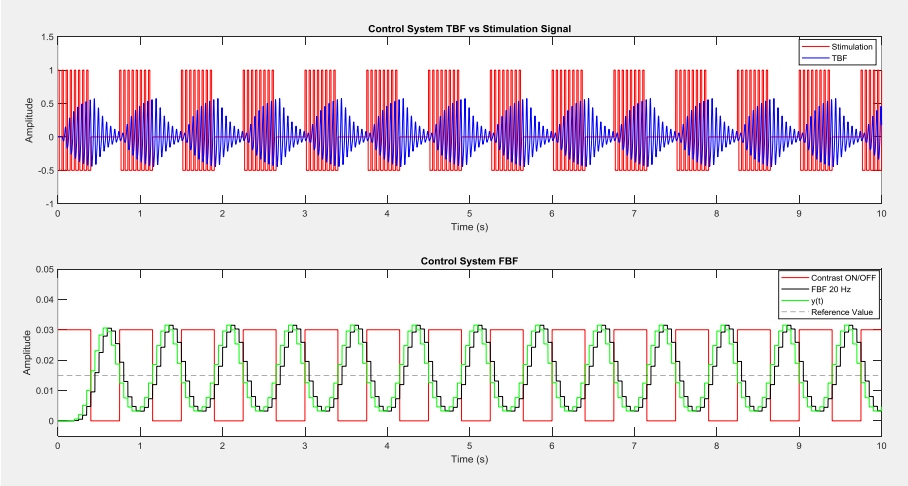

Figure 3.32) FSP control design results. TBF and stimulation signal variables (top), variation of the simulated FBF with the *contrast* variableG for the non-delayed model and for the real process model (bottom). Reference value =0.015; Proportional gain =1; Integrative gain =0; Derivative gain =0;

The results are very similar to the stand-alone PID system design, even with reference value and PID tuning variations. It's possible to observe by the FBF and *y(t)* variables time difference (see Figure 3.32) that the FSP controller design is accounting

for the 55 millisecond delay, but the real process output remains unstable. Closer TBF and FBF variables evaluation explains the instability origin (see Figure 3.33).

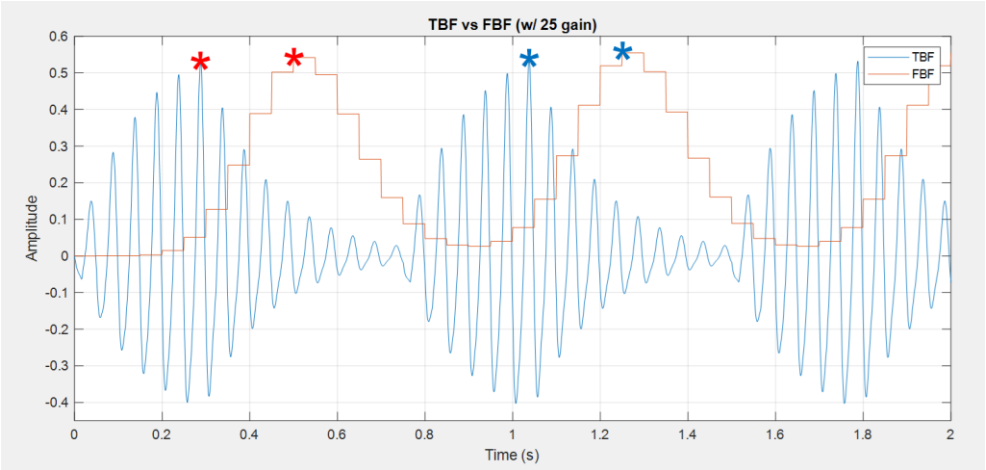

Figure 3.33) TBF vs FBF FSP control design results plot. Real process TBF vs FBF variables plotting. Matching color asterisks represent real time correspondent point of the two signals, demonstrating that there is a delay incurred between the real process TBF output and the FBF calculation containing block output.

Analysis show a massive delay induced by in FBF calculations, fact that was already suspected and now proved by the FSP design testing. The instantaneous power of a signal's specific frequency is bounded to the signal oscillations envelope at that same frequency, so the greater the oscillatory amplitude at 20 Hz frequency oscillations, the greater the value of the instantaneous power at 20 Hz frequency. This means that the TBF's signal maximum amplitude point must correspond in time with the FBF's maximum value. The asterisks in Figure 3.33 point the maximum values of the TBF and FBF variables in two different time points (red and blue asterisks). If the FBF calculation did not induce delays, the two red asterisks would be correspondent in time, and the same for the blue asterisks. The current calculation induces a ~5 FBF samples delay in the system. Given the FBF variable sampling at 20 Hz, this means that the calculation induces a ~275 ms delay in control, which makes the system impossible to stabilize. This delay cannot be isolated in the FSP design because it is not associated with transport/transmission delays incurred in the real process, but rather is associated with signal processing outside of the process.

3.3.2 TBF Envelope Linear Extrapolation

The TBF bandpass filtered signal around 20 Hz envelope is related to the power calculated to obtain the FBF variable. This new approach focuses on making an estimated 'prediction' of the direction in which the TBF envelope is evolving, so the *contrast switch* can deliver the stimulation based on real-time approximated conditions and avoid calculation delays.

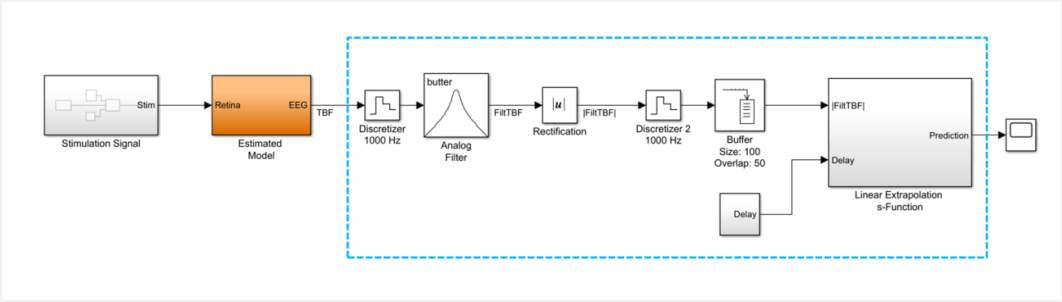

Figure 3.34) TBF variable linear extrapolation algorithm *Simulink*™ model. The blocks highlighted in blue will be implemented in the control loop were the FBF calculation was present in previous designs.

The TBF signal is firstly 2nd order butterworth bandpass filtered around 20 Hz (*FiltTBF*), rectified (|*FiltTBF*|) and then the oscillations peaks are identified (see Figure 3.35).

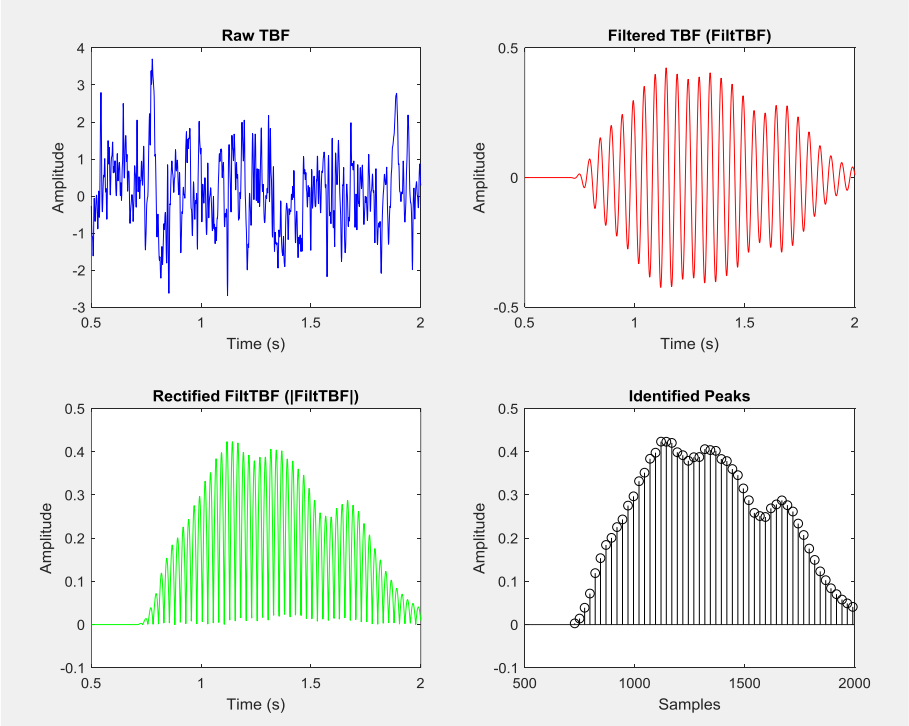

Figure 3.35) TBF variable signal processing steps. The TBF variable processing methods necessary to implement the proposed linear extrapolation algorithm.

The algorithm uses $|FiltTBF|$ variable 100 sample vectors with 50 sample overlap, calculates the peaks present in the sample vectors and performs the linear extrapolation from the two last peaks in each sample vector. The linear extrapolation algorithm defined delay (LEADD) is set depending on the delays to use in each simulation. If the LEADD value set is 0 milliseconds, the algorithm aims the extrapolation at the end of the 100 sample vector. If the delay is D the algorithm aims the extrapolation at D milliseconds ahead of the last sample (see Figure 3.36).

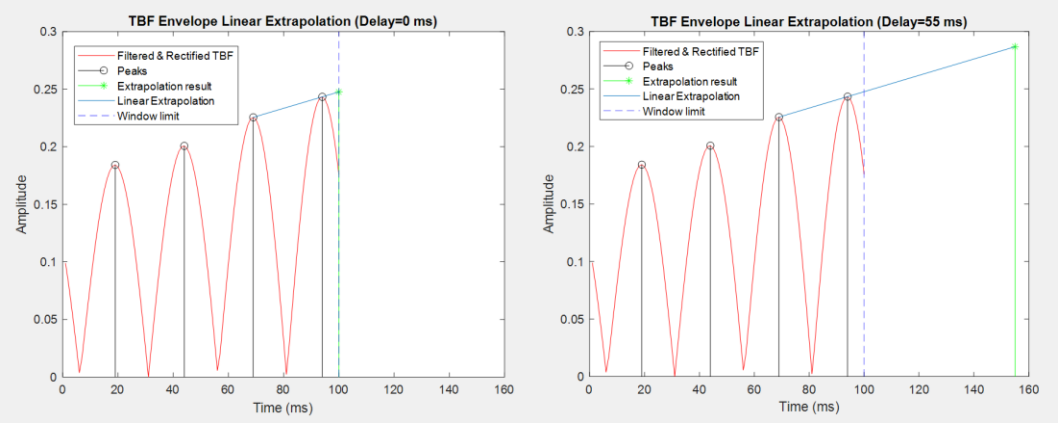

Figure 3.36) Linear extrapolation algorithm 1. Example of the linear extrapolation algorithm application in a $|FiltTBF|$ variable 100 sample vector. Specific cases of 0 milliseconds (left) and 55 milliseconds (right) LEADD settings.

The algorithm gives a TBF amplitude absolute value prevision. The prediction absolute value is not really relevant for the control purpose, because the *control switch* (all or nothing mechanism) reacts when the error variable *e(t)* crosses a defined threshold. The linear extrapolation algorithm real advantage is the direction prevision in which the delayed TBF variable at the EEG output is evolving, enabling an educated predictive control of the brain's present 20 Hz SSVEP amplitude value. Given the TBF variable is measured with a physiological delay in the best case scenario, what the algorithm tries to accomplish is not really a prediction (because the SSVEPs are being generated at the same time in the brain) but rather a estimation of the brain SSVEP response present value, based on the delayed recordings at the EEG output.

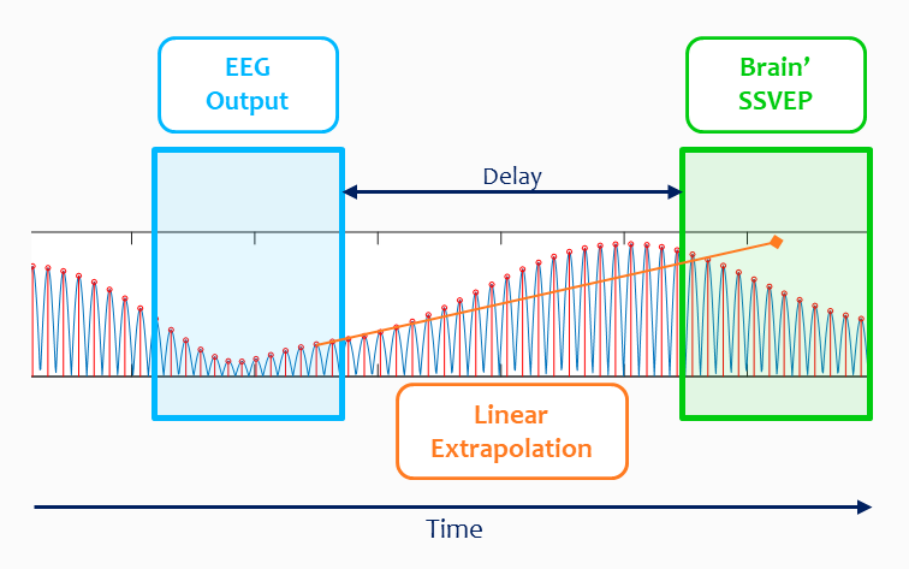

Figure 3.37) Linear extrapolation algorithm 2. Exemplified representation of the control loop linear extrapolation algorithm's purpose. The envelope estimated absolute value is not precise, but indicates that the potentials amplitude is rising, which gives the control a trigger reaction to signals that were not even recorded in the EEG.

Theoretically, this solves the problem of the in loop delays induced by the FBF calculation and can also be important in the physiological and hardware delay's effect reduction in the control loop.

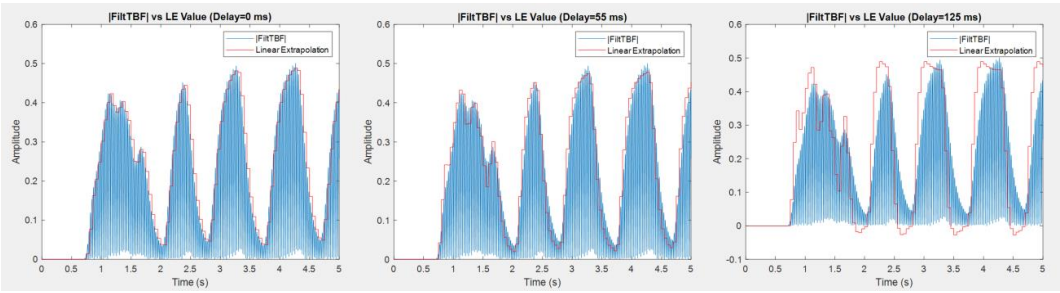

Figure 3.38) Linear extrapolation algorithm 3. Linear extrapolation values observed for different LEADD settings. The estimated absolute value precision increases for lower LEADD settings (tending to o ms). In the case of 0 ms LEADD setting (left) the resultant linear extrapolation value follows the envelope almost precisely, while in the case of 125 ms LEADD setting (right) the envelope absolute values are clearly over- and under- shoot by the linear extrapolation.

The linear extrapolation algorithm blocks were implemented in the filtered Smith-predictor (FSP) control design (Figure 3.39).

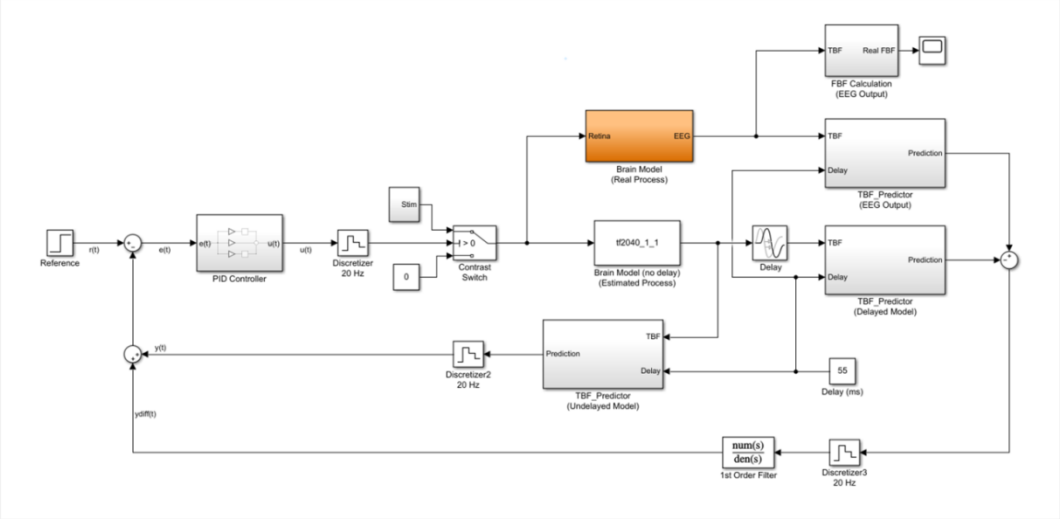

Figure 3.39) FSP & linear extrapolation algorithm control design. FSP with in loop incorporated linear extrapolation algorithm *Simulink*™ model. This design uses a constant block with a definable delay to use for the algorithm calculation. The linear extrapolation algorithm replaces the in loop FBF calculation, although this calculation is still performed at the real process output.

In this new control design, the reference value is related to the TBF variable amplitude. Now, the EEG TBF 20 Hz oscillations envelope is the variable controlled. The FBF is simultaneously calculated outside the control loop, for analysis purposes.

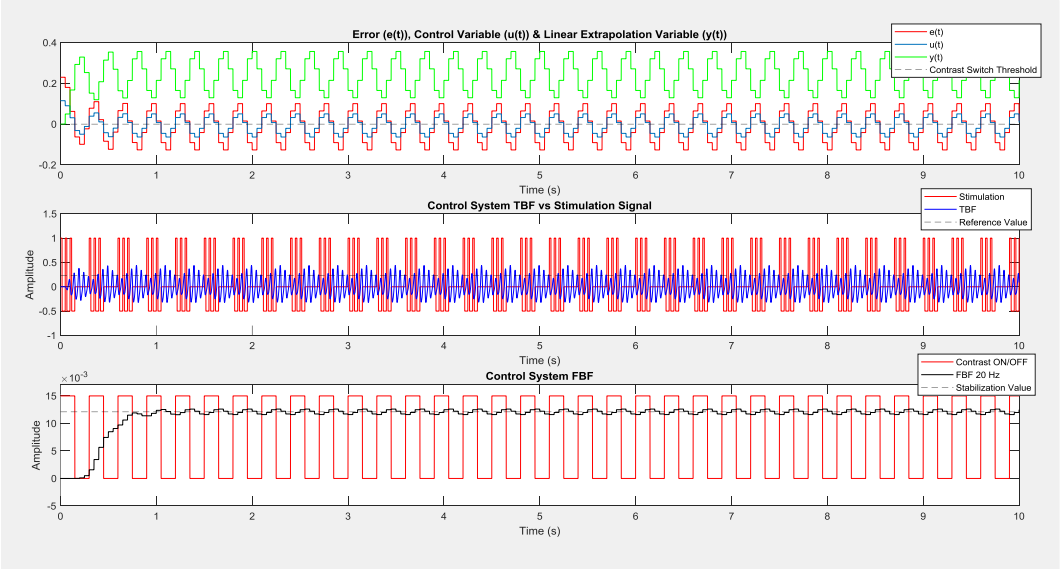

Figure 3.40) FSP & linear extrapolation algorithm control design results 1. Results observed after linear extrapolation algorithm incorporated FSP simulation. Reference value =0.23; Proportional gain =0.5; Integrative gain =0; Derivative gain =0; LEADD =55 ms; FBF Stabilization Value =0.0121.

The new control system design simulation results are encouraging (linear extrapolation algorithm incorporated in the FSP control design). In Figure 3.40, is observable a clear manipulation of both the TBF and FBF variables. The linear

extrapolation algorithm resultant variable *y(t)* is subtracted to the reference value *r(t)* setting obtaining the proportional controller error *e(t)* (PID tuning with proportional gain only). However, the TBF 20 Hz amplitude oscillates around the reference value *r(t)*, so the system is marginally stable. This does not diminish the importance of the results, given the previous control system simulations repetitive unsuccessful outcomes and difficulty in bypassing system delays. Also, the PID tuning provokes alterations in stabilization as presented in the following figures.

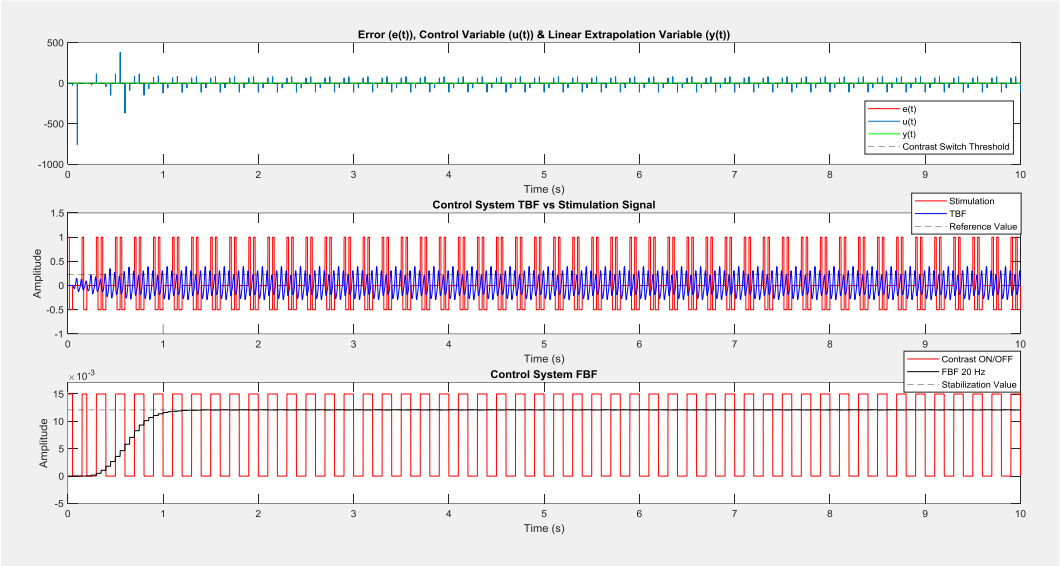

Figure 3.41) FSP & linear extrapolation algorithm control design results 2. Derivative gain variation results. Reference value =0.23; Proportional gain =0.5; Integrative gain =0; Derivative gain =0.5; LEADD=55 ms; FBF Stabilization Value =0.0121.

For an inclusion of a 0.5 gain in the PID's derivative branch, there are clear alterations in the TBF variable response (see Figure 3.41 and compare with Figure 3.40). The system FBF variable oscillates around a stabilization step value maintained at 0.0121, with this tuning modification considerably reducing the FBF variable oscillations. However, the system enters in a steady state. Reference value setting variations do not influence the FBF stabilization step value, so the derivative gains inclusion will be avoided. Integral gain alterations also provoke unwanted modifications (instability) in the FBF variable, however with a 0.5 integral gain and a 0.29 reference value, the system outputs a very stable FBF variable and the reference value setting increase presents an interesting output evolution (see Figure 2.42).

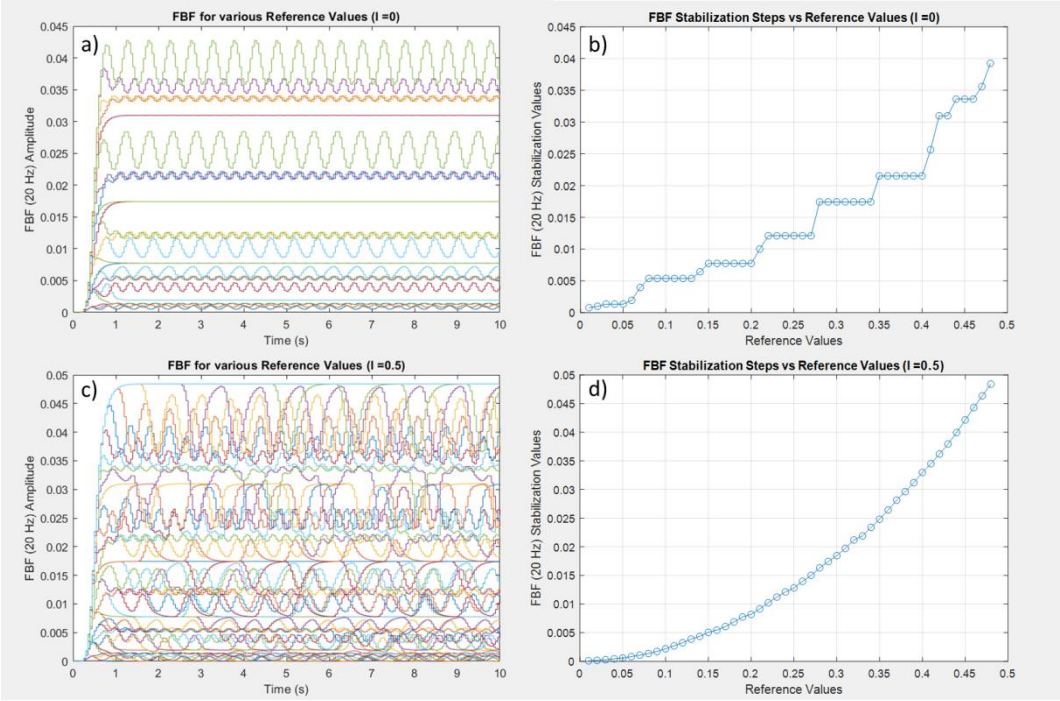

Figure 3.42) FSP & linear extrapolation algorithm control design integral gain variation results. Reference value ranging from 0.01 to 0.48; Proportional gain =0.5; Derivative gain =0; LEADD =55 ms.

The FBF signals obtained for a 0.5 integral gain are much more unstable than the ones obtained using only a proportional gain. Analyzing Figure 3.42b it's possible to observe that, for some sequential reference values the stabilization step does not change (*I=0* tuning). This phenomenon can be linked with unknown estimated models characteristics/properties when stimulated with the variables generated by the *contrast switch*. It is not expected that this phenomenon occurs in the brain. For the case of *I =0.5* (Figure 3.42d), the FBF stabilization step varies exponentially. Analyzing the FBF variables (Figure 3.42c), several instabilities are present for almost all of the reference values tested, except for the reference value of 0.29, which satisfactorily stabilizes at 0.0174 (see Figure 4.43).

Setting the LEADD to 0 milliseconds has an impact on stability and on FBF stabilization step absolute values for each reference value setting, but maintains the FBF 20 Hz variable oscillating reference value (see Figure 3.44). The LEADD setting can be defined accordingly to the delays observed in a specific experiment, adjusting the algorithm to each individual case. This is important given the inter- and intra-individual variability observed in SSVEP responses observed throughout experimental trials.

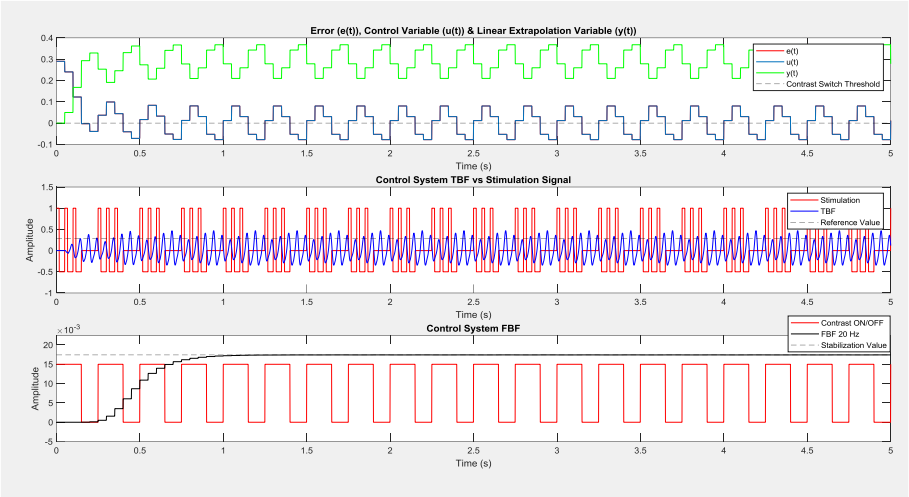

Figure 3.43) FSP & linear extrapolation algorithm control design results 3. Integral gain presence result for a 0.29 reference value. Reference value =0.29; Proportional gain =0.5; Integrative gain =0.5; Derivative gain =0; LEADD =55 ms; FBF Stabilization Value =0.0174.

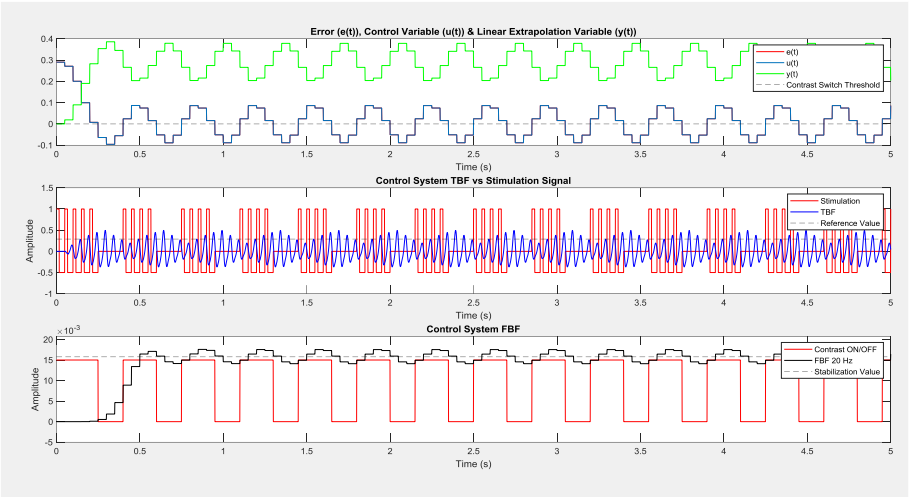

Figure 3.44) FSP & linear extrapolation algorithm control design results 4. Results for the variation of defined delay value in the algorithm. Reference value =0.29; Proportional gain =0.5; Integrative gain =0.5; Derivative gain =0; LEADD =0 ms; FBF Stabilization Value =0.0158.

After obtaining such results it can be confidently stated that the designed system successfully manipulates the estimated model *tf2040_1_1* and can be tested for all the models selected in section *3.2.3) Models' Validation*. If these results are replicable for all the models, then a real time experimental prototype can be developed to test the control system in real-time experiences with humans. Based on the previously presented results, the simulations will include reference value and linear extrapolation algorithm defined delay (LEADD) setting throughout simulations.

Chapter 4:

Results & Discussion

In this chapter, all the estimated models selected in section *3.2.3) Models Validation* will be tested for various reference value settings and algorithm parameters. The goal is to evaluate if the results observed in section *3.3.2) TBF Envelope Linear Extrapolation* are replicable for several models obtained with section's *3.2.2 TBF Reconstruction Approach to Model Estimation* protocols and if the design is suited for real-time closed loop experiments in human.

4.1 Simulation Results

Every estimated model possesses a saturation reference value which makes the system present a continuous stimulation ON state. This saturation value was measured for every model and is presented in Table 4.1.

Table 4.1) Models simulation parameters. TBF saturation corresponding reference values and estimated models maximum reference values tested.

Models Selected (Denomination)	Maximum Reference Value to be Tested (TBF)	Saturation Reference Value (TBF)
tf2040_1_1	0,48	0,49
tf2040_9_4	0,36	0,37
tf2040_1_2_1s	0,50	0,51
tf2040_2_4_1s	0,30	0,31
tf2040_3_4_1s	0,49	0,50
tf2040_5_1_1s	0,47	0,48
tf2040_6_2_1s	0,39	0,40
tf2040_7_2_1s	0,44	0,45
tf2040_10_3_1s	0,79	0,80

The models will be simulated in loop for 0.01 spaced reference values settings between 0.01 and their respective maximum reference value (see Table 4.1). These

stimulations will give a FBF stabilization step variation perspective with the increase of the reference value setting for each individual simulation. Models results will present: a graphic containing all the individual simulations FBF variables, each corresponding to a reference value setting; a detailed result analysis for an individual reference value setting. For purposes of brevity, only the detailed analysis will contain linear extrapolation algorithm defined delay (LEADD) setting variations. The PID controller is tuned with a proportional gain of 1, given the instability induced by the derivative and integral branches observed during system design. To replicate the physiological delays incurred in the visual pathway (see section *2.1.5) Visual Pathways*), a 55 milliseconds transport delay is applied in loop.

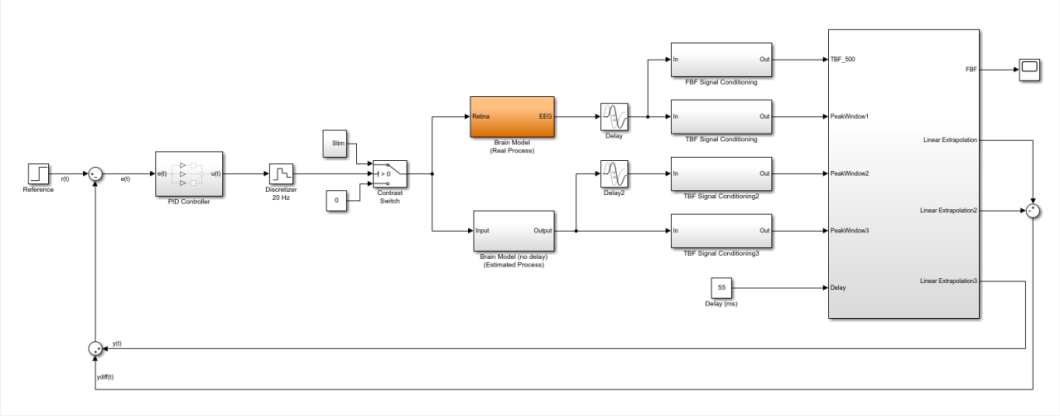

Figure 4.1) Simulations control system design. *Simulink*™ model used to perform simulations with the estimated models. This model makes use of a level-2 *Matlab*™ s-function comprising all the signal analysis and control calculations and algorithms.

Model tf2040_1_1

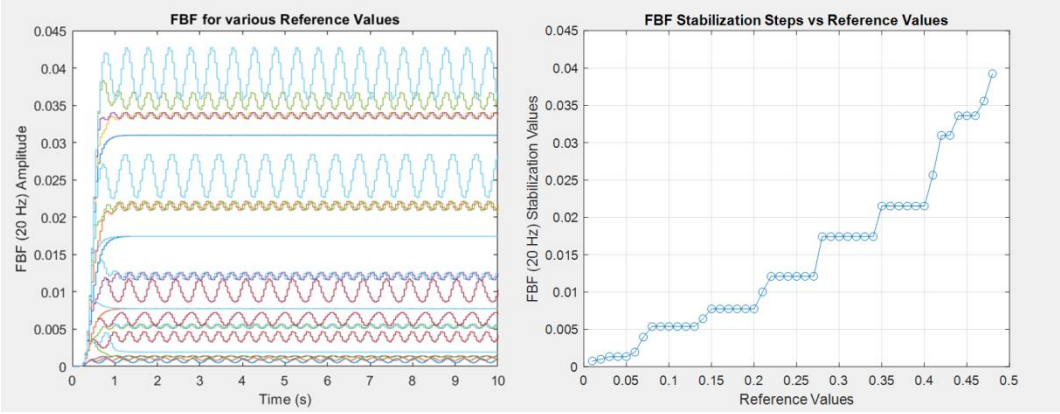

Figure 4.2) Model *tf2040_1_1* simulation results 1. Model *tf2040_1_1* reference values variation results. Proportional gain =1; Integrative gain =0; Derivative gain =0; LEADD=55 ms.

For model *tf2040_1_1*, the FBF variable presents similar stabilization steps values for sequential reference values (see Figure 4.2 right). This phenomenon can be related with the estimated models stimulation response, which is a visual stimuli approximation. Most important is that the FBF stabilization step values increase with the reference values setting increase throughout simulations (see Figure 4.2 left). This proves that the estimated brain models output can be controlled using the proposed control system design (see sections *3.2.2) TBF Reconstruction Approach to Model Estimation* and *3.3.2) TBF Envelope Linear Extrapolation*). The above results were obtained with a 55 ms LEADD to enforce the system output stabilization, given that the in loop transport delay is set to 55 milliseconds. The procedure is repeated for all models simulation.

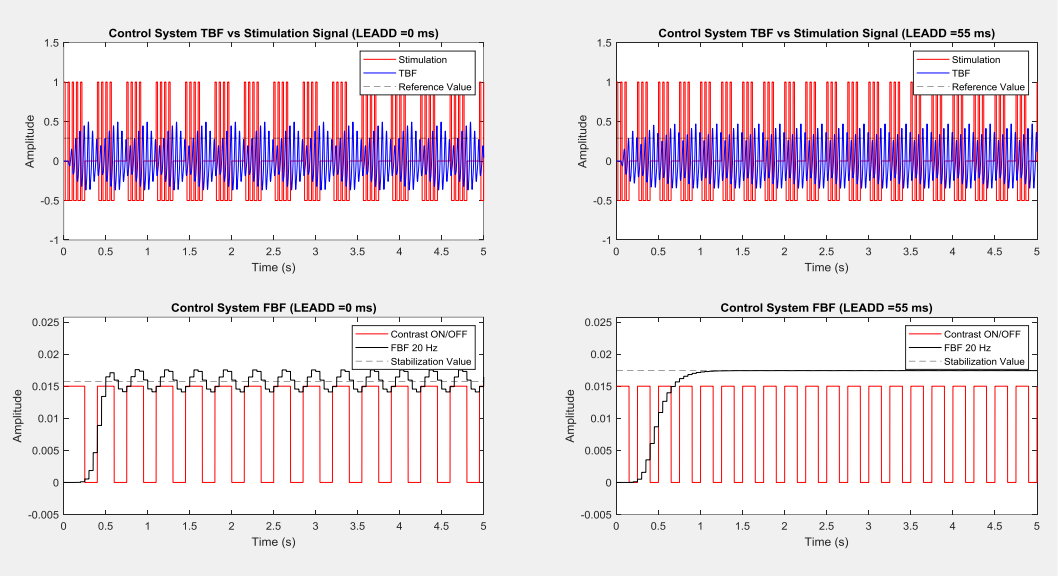

Figure 4.3) Model *tf2040_1_1* simulation results 2. Model *tf2040_1_1* results for the LEADD of 0 (left) and 55 (right) milliseconds, in a 0.29 reference value simulation. Proportional gain =1; Integrative gain =0; Derivative gain =0; FBF stabilization step (LEADD=0ms) =0.0158; FBF stabilization step (LEADD=55ms) =0.0174.

Analyzing the 0.29 reference value setting results, by comparison of left and right simulation graphics presented in Figure 4.3, it is possible to observe the LEADD setting influence in the FBF and TBF variables. The LEADD setting influences the FBF variable both oscillatory behavior and stabilization step value. Such findings sustain that the algorithm's LEADD setting is of major importance in the efforts to control and improve the FBF variable stabilization. The LEADD setting must be defined accordingly to the hardware and physiological processes' delays observed experimentally.

Model tf2040_9_4

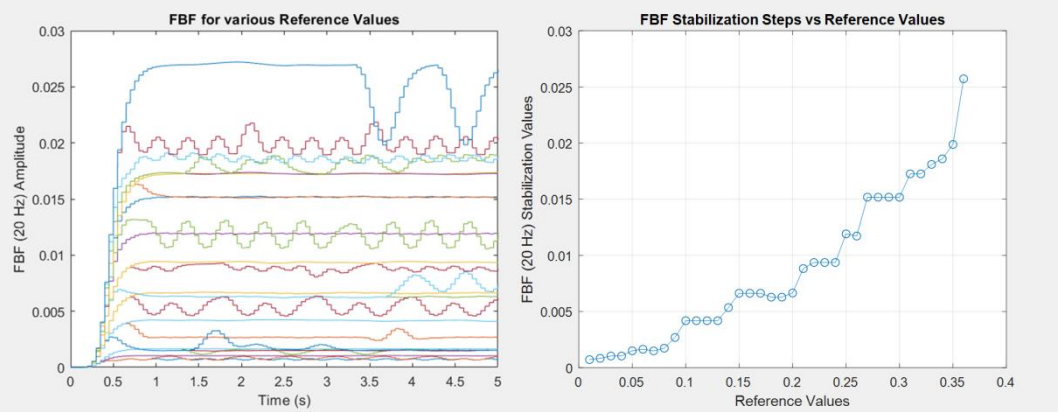

Figure 4.4) Model *tf2040_9_4* simulation results 1. Model *tf2040_9_4* reference values variation results. Proportional gain =1; Integrative gain =0; Derivative gain =0; LEADD =55 ms.

A model *tf2040_1_1* similar behavior is observed for the model *tf2040_9_4* responses. Some reference values swept generated very unstable FBF responses, so not all reference values can be considered suited to accomplish model output stabilization. Nonetheless, these results are again very encouraging, given this model results coherence with the model results analyzed so far.

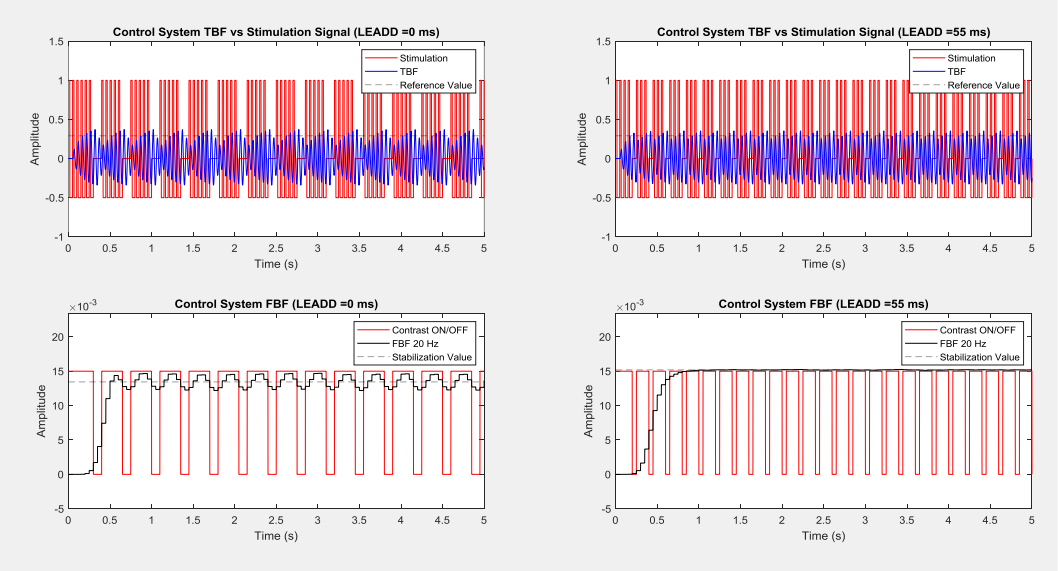

Figure 4.5) Model *tf2040_9_4* simulation results 2. Model *tf2040_9_4* results for the LEADD of 0 (left) and 55 (right) milliseconds, in a 0.29 reference value simulation. Proportional gain =1; Integrative gain =0; Derivative gain =0; FBF stabilization step (LEADD=0ms) =0.0134; FBF stabilization step (LEADD=55ms) =0.0152.

Also the LEADD setting variation produced a model *tf2040_1_1* similar behavior, with the output oscillatory amplitude being attenuated and the stabilization step value lightly increasing.

Model tf2040_1_2_1s

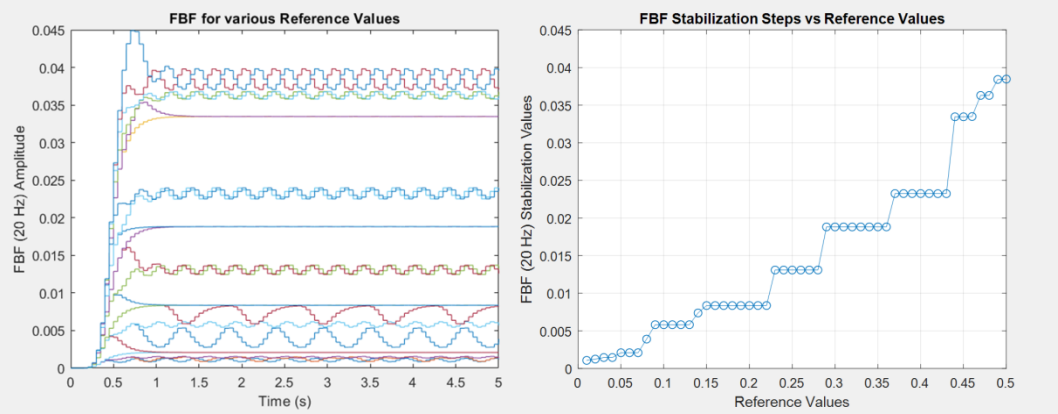

Figure 4.6) Model *tf2040_1_2_1s* simulation results 1. Model *tf2040_1_2_1s* reference values variation results. Proportional gain =1; Integrative gain =0; Derivative gain =0; LEADD =55 ms.

Given that the estimation data of model *tf2040_1_2_1s* is from the same experimental subject as model *tf2040_1_1*, the stabilization step values similarities were already expected, demonstrating coherence in the results (comparison of Figures 4.2 & 4.6). Only by performing new experimental trials is possible to evaluate which of the model estimation techniques is best suited for each individual, but these evidences support both models are stabilization possibilities and are prepared to be implemented in loop.

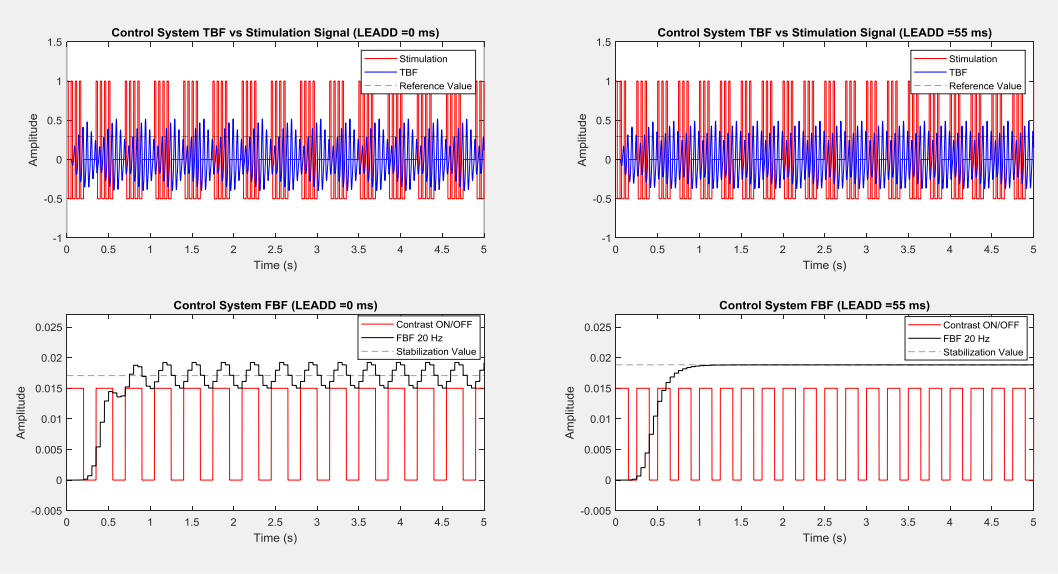

Figure 4.7) Model *tf2040_1_2_1s* simulation results 2. Model *tf2040_1_2_1s* results for the LEADD of 0 (left) and 55 (right) milliseconds, in a 0.29 reference value simulation. Proportional gain =1; Integrative gain =0; Derivative gain =0; FBF stabilization step (LEADD=0ms) =0.0170; FBF stabilization step (LEADD=55ms) =0.0188.

Once again, the LEADD setting to 55 milliseconds enforces FBF response stability (see Figure 4.7).

Model tf2040_2_4_1s

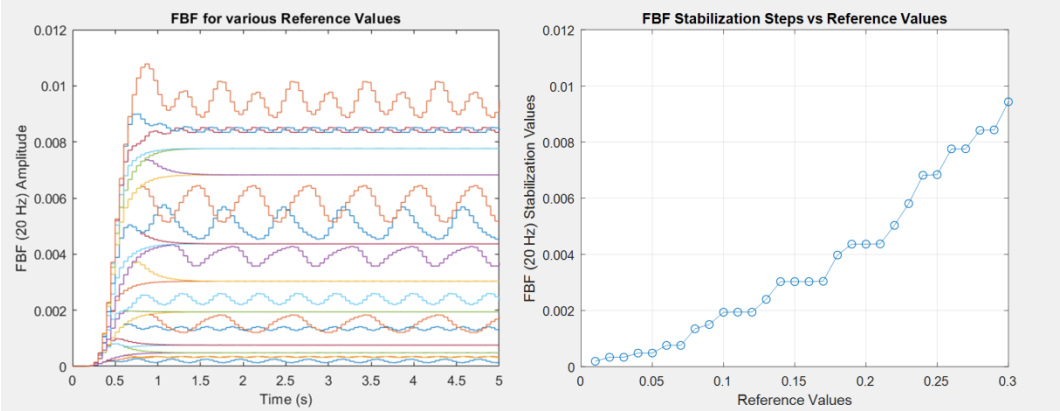

Figure 4.8) Model *tf2040_2_4_1s* simulation results 1. Model *tf2040_2_4_1s* reference values variation results. Proportional gain =1; Integrative gain =0; Derivative gain =0; LEADD =55 ms.

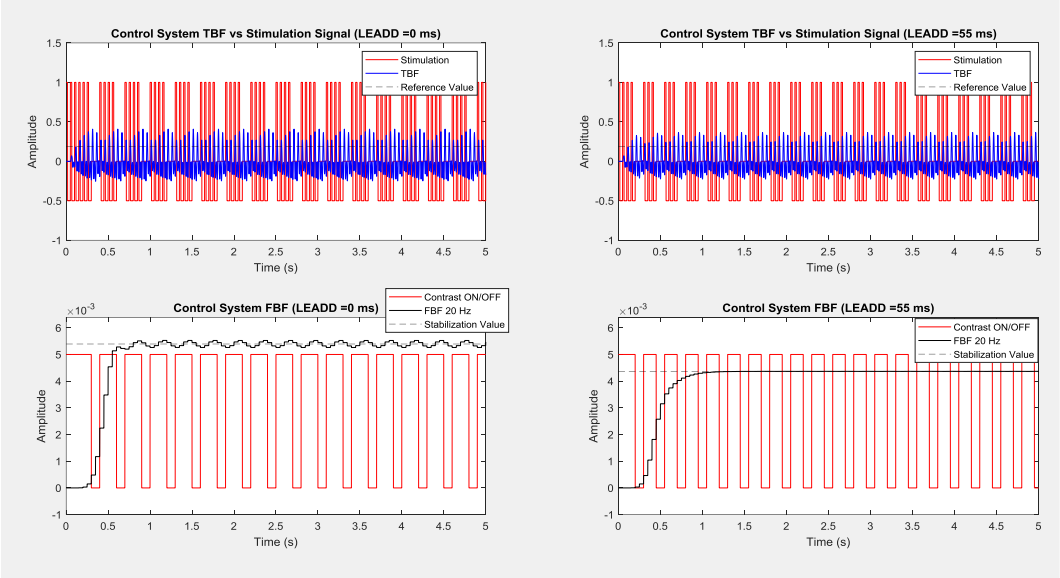

Figure 4.9) Model *tf2040_2_4_1s* simulation results 2. Model *tf2040_2_4_1s* results for the LEADD of 0 (left) and 55 (right) milliseconds, in a 0.19 reference value simulation. Proportional gain =1; Integrative gain =0; Derivative gain =0; FBF stabilization step (LEADD=0ms) =0.0054; FBF stabilization step (LEADD=55ms) =0.0044.

Model *tf2040_2_4_1s* behaves differently from the previous models. When varying the LEADD from 0 to 55 milliseconds, the stabilization is enforced (as expected), but the model responded with a lower stabilization step value, presenting an opposite behavior to the previous models results. Also, this is the only model which detailed analysis was performed using a 0.19 reference value setting (all the other models were observed at 0.29 reference value), given that the use of a higher reference value for this model throws the system very close to saturation.

Model tf2040_3_4_1s

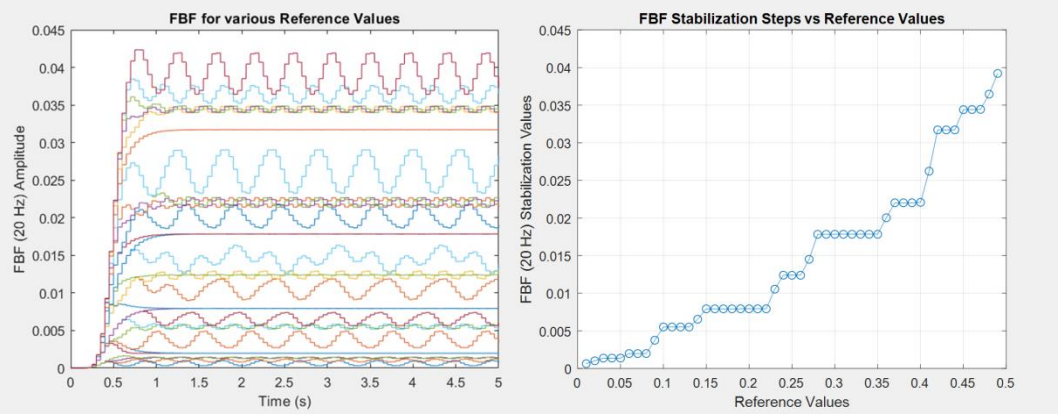

Figure 4.10) Model *tf2040_3_4_1s* simulation results 1. Model *tf2040_3_4_1s* reference values variation results. Proportional gain =1; Integrative gain =0; Derivative gain =0; LEADD =55 ms.

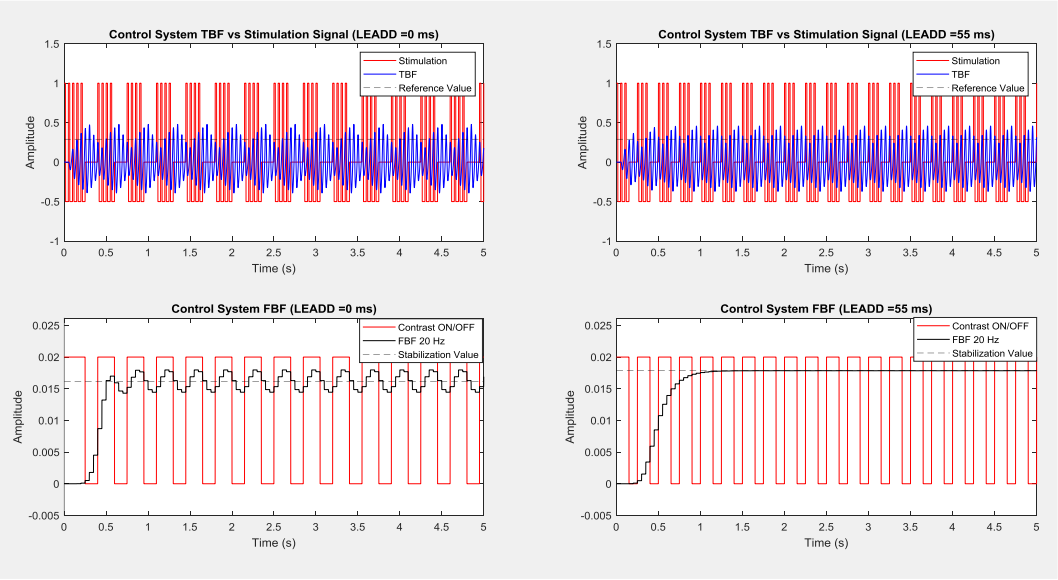

Figure 4.11) Model *tf2040_3_4_1s* simulation results 2. Model *tf2040_3_4_1s* results for the LEADD of 0 (left) and 55 (right) milliseconds, in a 0.29 reference value simulation. Proportional gain =1; Integrative gain =0; Derivative gain =0; FBF stabilization step (LEADD=0ms) =0.0161; FBF stabilization step (LEADD=55ms) =0.0178.

Model *tf2040_3_4_1s* presents a similar behavior to models *tf2040_1_1*, *tf2040_9_4* and *tf2040_1_2_1s*, with the FBF variable presenting stabilization steps for various reference value settings. With 55 ms LEADD enforced stability, the FBF variable stabilization step value slightly increased, showing coherence with the majority of models already simulated.

Model tf2040_5_1_1s

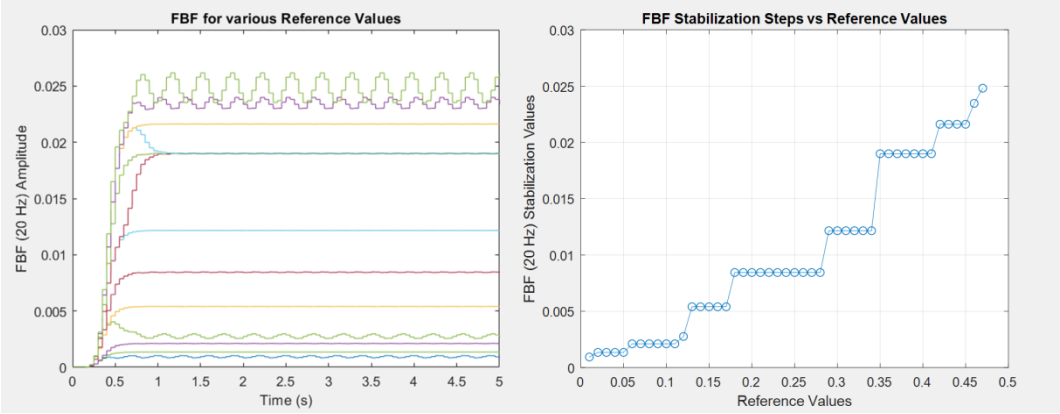

Figure 4.12) Model *tf2040_5_1_1s* simulation results 1. Model *tf2040_5_1_1s* reference values variation results. Proportional gain =1; Integrative gain =0; Derivative gain =0; LEADD =55 ms.

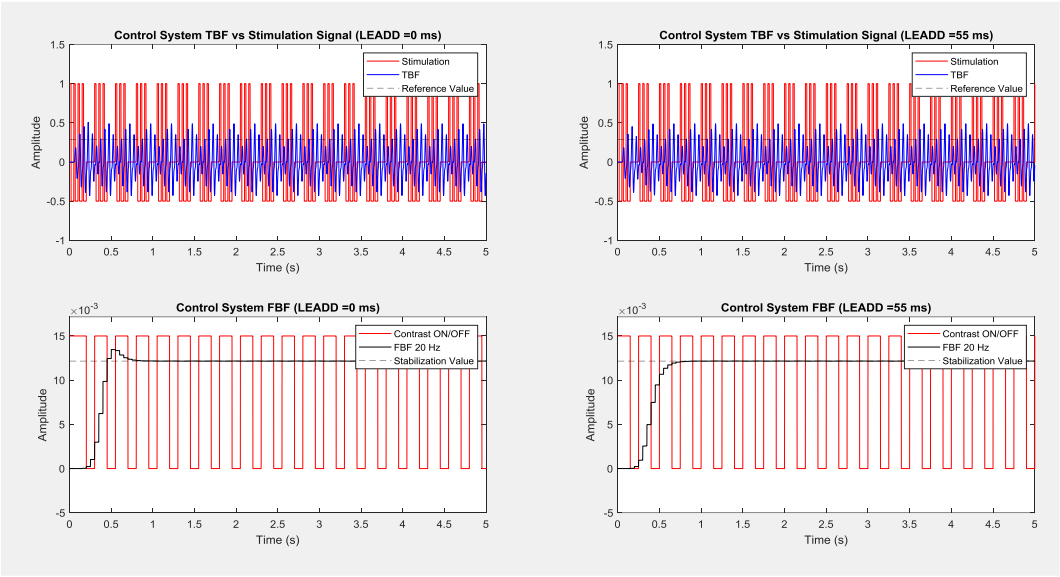

Figure 4.13) Model *tf2040_5_1_1s* simulation results 2. Model *tf2040_5_1_1s* results for the LEADD of 0 (left) and 55 (right) milliseconds, in a 0.29 reference value simulation. Proportional gain =1; Integrative gain =0; Derivative gain =0; FBF stabilization step (LEADD=0ms) =0.0122; FBF stabilization step (LEADD=55ms) =0.0122.

Stabilization step values evolution was coherent with previous results (see Figure 4.12). A new behavioral tendency is observed in model *tf2040_5_1_1s* detailed analysis. The o ms LEADD setting performs FBF variable stabilization at the value 0.0122, with a slight overshoot (see Figure 4.12 left). The 55 ms LEADD setting corrects the overshoot and stabilizes the FBF output at the value of 0.0122, behavior not coherent with the stabilization step value increase observed in previous cases for a 55 ms LEADD.

Model tf2040_6_2_1s

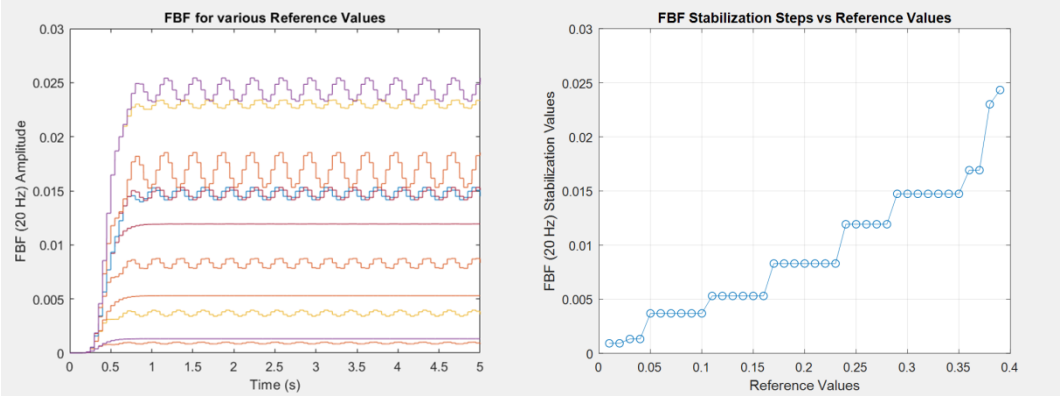

Figure 4.14) Model *tf2040_6_2_1s* simulation results 1. Model *tf2040_6_2_1s* reference values variation results. Proportional gain =1; Integrative gain =0; Derivative gain =0; LEADD =55 ms.

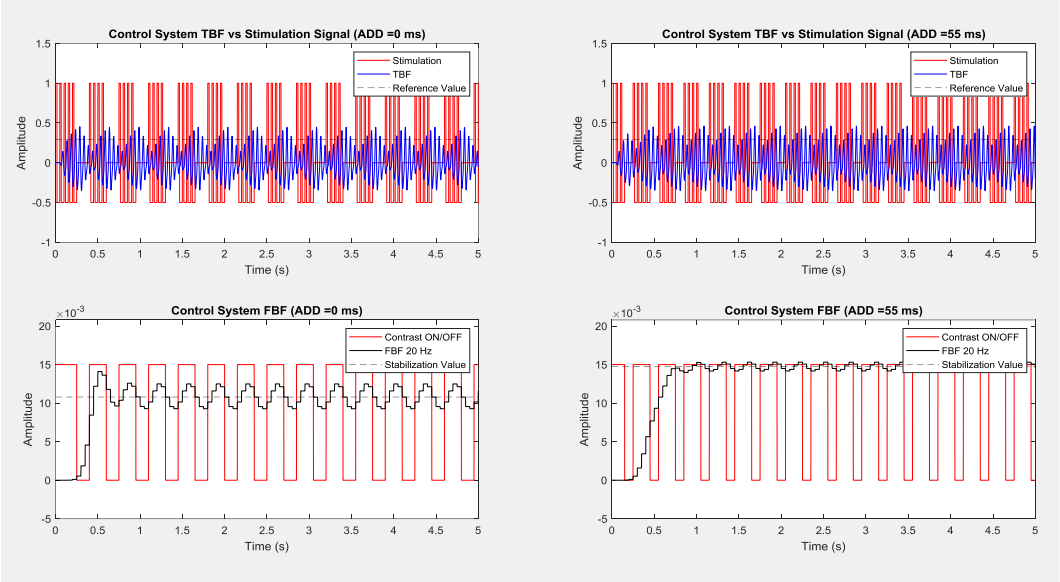

Figure 4.15) Model *tf2040_6_2_1s* simulation results 2. Model *tf2040_6_2_1s* results for the LEADD of 0 (left) and 55 (right) milliseconds, in a 0.29 reference value simulation. Proportional gain =1; Integrative gain =0; Derivative gain =0; FBF stabilization step (LEADD=0ms) =0.0108; FBF stabilization step (LEADD=55ms) =0.0147.

Model *tf2040_6_2_1s* presents a similar FBF variable behavior to models *tf2040_1_1*, *tf2040_9_4*, *tf2040_1_2_1s* and *tf2040_3_4_1s*, which presents increasing stabilization step values for various reference value settings. With 55 ms LEADD enforced stability, the FBF variable stabilization step value slightly increases once more, showing coherence with the majority of models already simulated.

Model tf2040_7_2_1s

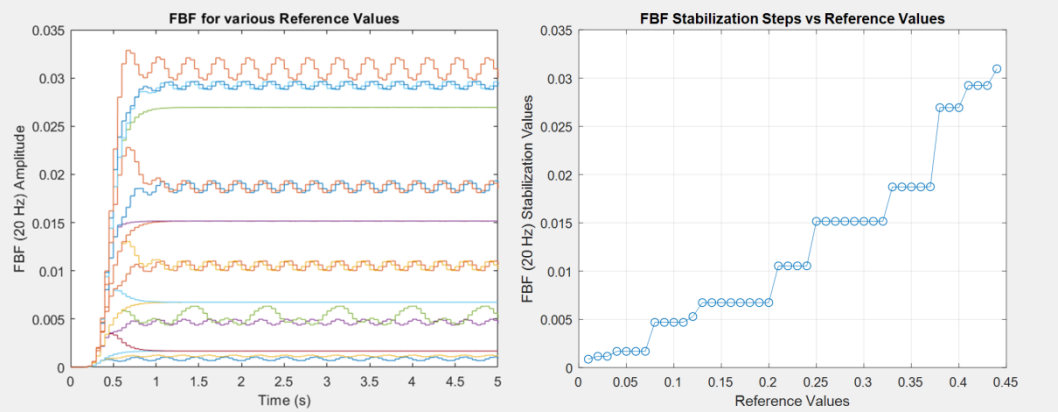

Figure 4.16) Model *tf2040_7_2_1s* simulation results 1. Model *tf2040_7_2_1s* reference values variation results. Proportional gain =1; Integrative gain =0; Derivative gain =0; LEADD =55 ms.

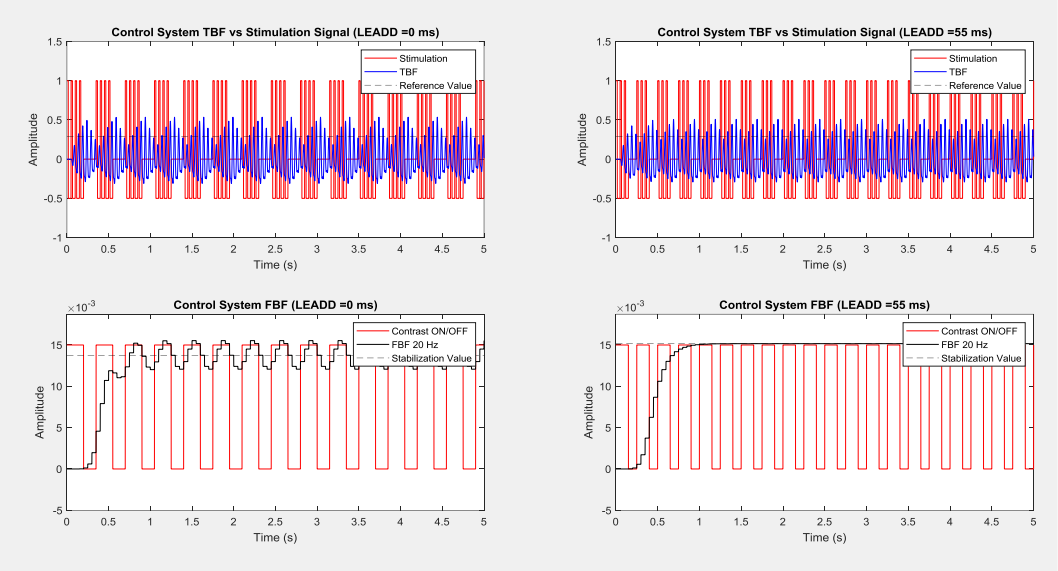

Figure 4.17) Model *tf2040_7_2_1s* simulation results 2. Model *tf2040_7_2_1s* results for the LEADD of 0 (left) and 55 (right) milliseconds, in a 0.29 reference value simulation. Proportional gain =1; Integrative gain =0; Derivative gain =0; FBF stabilization step (LEADD=0ms) =0.0137; FBF stabilization step (LEADD=55ms) =0.0152.

Model *tf2040_7_2_1s* presents a similar FBF variable behavior to models *tf2040_1_1*, *tf2040_9_4*, *tf2040_1_2_1s*, *tf2040_3_4_1s* and *tf2040_6_2_1s*, were the FBF variable presents increasing stabilization step values for various reference value settings. With 55 ms LEADD enforced stability, the FBF variable stabilization step value slightly increases once more, showing coherence with the majority of models already simulated.

Model tf2040_10_3_1s

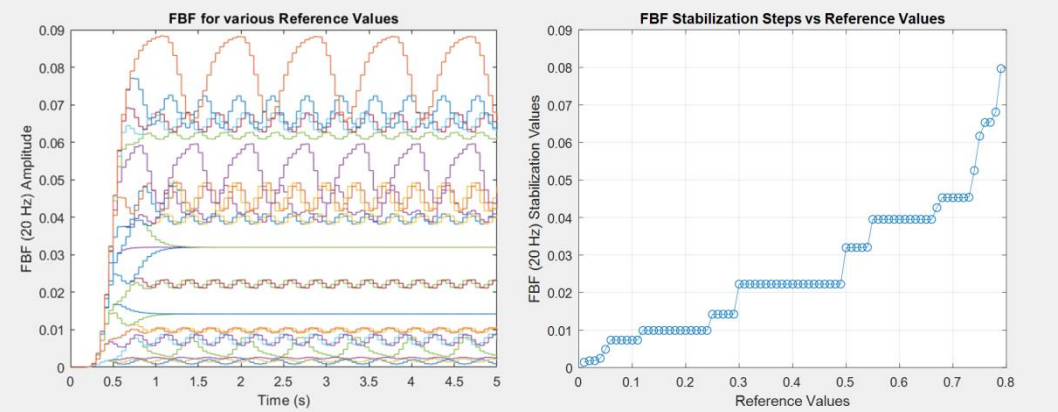

Figure 4.18) Model *tf2040_10_3_1s* simulation results 1. Model *tf2040_10_3_1s* reference values variation results. Proportional gain =1; Integrative gain =0; Derivative gain =0; LEADD =55 ms.

Model *tf2040_10_3_1s* presents the highest saturation value in comparison to all the other selected estimated models responses, supporting the inter-individual variability presented by brain SSVEP responses.

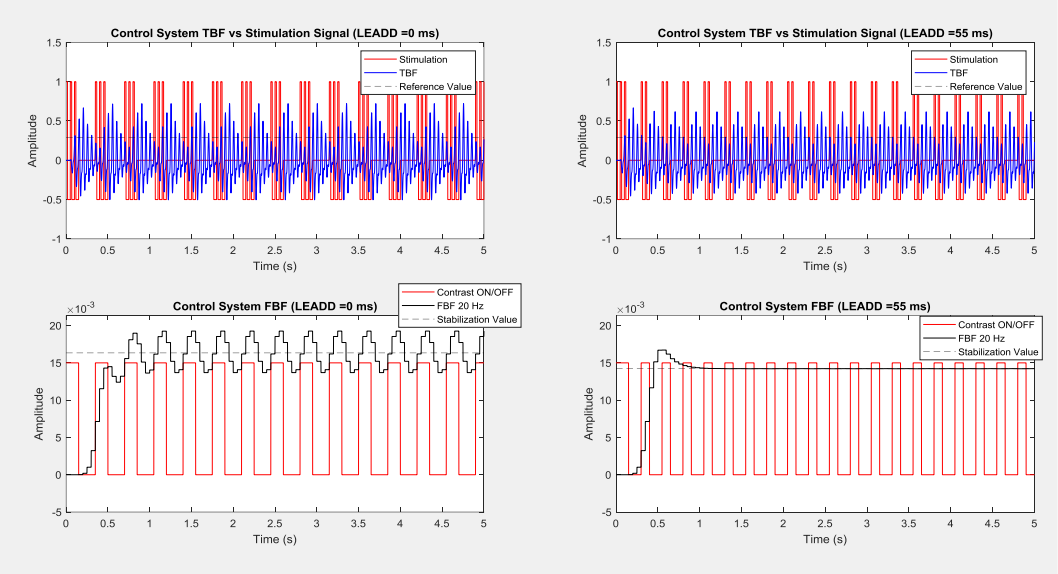

Figure 4.19) Model *tf2040_10_3_1s* simulation results 2. Model *tf2040_10_3_1s* results for the LEADD of 0 (left) and 55 (right) milliseconds, in a 0.29 reference value simulation. Proportional gain =1; Integrative gain =0; Derivative gain =0; FBF stabilization step (LEADD=0ms) =0.0163; FBF stabilization step (LEADD=55ms) =0.0142.

Similarly to model *tf2040_2_4_1s*, the 55 ms LEADD setting stabilization step is lower than for the 0 ms LEADD setting. What is evident is that the LEADD enforced stabilization, observable both in the TBF and FBF signals (see Figure 4.19).

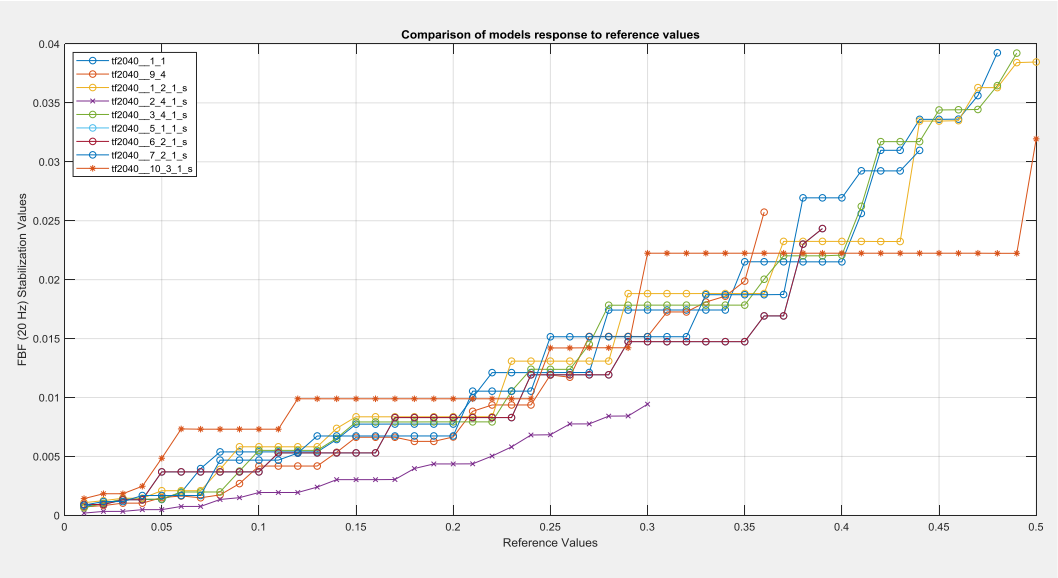

Figure 4.20) FBF variable stabilization results. Comparison between all the models stabilization step values evolution with reference value setting increase (LEADD= 55 ms and 0.01 reference value increase between simulations). The plot does not include all the data for model *tf2040_10_3_1s*, given the significant difference in stabilization step values magnitude when compared to the other models. See Appendix B for model *tf2040_10_3_1s* magnitude comparison with remaining models.

With the exception of models *tf2040_2_4_1s* and *tf2040_10_3_1s* significant stabilization step values magnitude differences, the models present similar evolutions with the reference value increase. All the models present stabilization steps with equal absolute value for sequential reference values. Given that the models are estimated with resource to recorded brain signals, it is possible to differentiate three groups of individuals based on the TBF signal amplitude. Also, models can be distinguished by responses to the 55 ms LEADD setting. The 55 ms LEADD setting enforces stability in all models, but the models responses differ in terms of stabilization step values variation in consequence of LEADD increase from 0 to 55 ms. Models *tf2040_1_1*, *tf2040_9_4*, *tf2040_1_2_1s*, *tf2040_3_4_1s*, *tf2040_6_2_1s* and *tf2040_7_2_1s* present the most common behavior, with the 55 ms LEADD setting enforced stability slightly increasing the FBF variable stabilization step value. Models *tf2040_2_4_1s* and *tf2040_10_3_1s* response to 55 ms LEADD set include stabilization enforcement and a slight decrease in the stabilization step value.

4.2 Results' Discussion

The interpretation of results must not only be made in light of the FBF variable. As previously presented, the FBF variable is a discrete calculation performed in 500 sample FBF variable vectors at a 20 Hz rate. This means that the FBF variable is an instantaneous power measurement of system's state, performed every 50 ms, while the brain reactions and responses to visual stimulus information arrival at the primary visual cortex can happen at much lower time orders. The instantaneous power is related with the TBF 20 Hz oscillations amplitude. So, the FBF variable is an approximation to the system real state, while the TBF variable gives a more complete understanding about the brain SSVEP responses current state. This means the TBF 20 Hz envelope analysis is more efficient for studies related with brain SSVEPs. When comparing system's TBF and FBF variables, it is possible to observe that even if the FBF variable is stabilized in one specific value, the TBF variable from which the FBF was measured presents oscillations in amplitude (see Figures 4.3, 4.5, 4.7, 4.9, 4.11, 4.13, 4.15, 4.17 and 4.19). From *Soares et al* [15] results observation and interpretation, it was never expected to obtain absolute stabilizations of the TBF 20 Hz envelope due to several facts: firstly, the all or nothing stimulation design used makes it very difficult to induce and maintain oscillatory activity given the physiological mechanisms involved in generating brain SSVEPs; secondly, the SSVEPs driven by long periods of visual stimulation are often attenuated throughout experimental trials (and even during individual trials) due to subject light stimulus habituation and/or eye fatigue. However, prior to these control strategies implementation, it was not even possible to stabilize the FBF variable. It can be confidently said that the primary objective was successfully accomplished. Also, the stabilization step values variation with the reference value setting increase is also a very important observation (see Figure 4.20), giving space to study several system stabilizations and opt for reference value settings that best suit each experimental individual case. All the models tested presented coherent results. However, each individual case presents slightly different characteristics and behavior to the same type of stimulation, so the system parameters must be adjusted by analysis of each case individually.

It's important to underline that these results relate to simulated SSVEP brain models, which do not consider physiological noise levels or intra-individual brain activity variability throughout experimental trials. Despite that, the elevated validation percentile correlations with experimental data are convincing about the reliability of the brain models. The frequency specific SSVEPs amplitude stabilization setup is expected to present experimental results similar to simulation results, with a marginally stable FBF variable and a low oscillatory TBF frequency specific (20 Hz in this case) variable around a reference value. Moreover, the system successful performance strongly depends on the models capability to replicate the real-time brain SSVEPs induced by visual stimuli. One of the observation conclusions is that different models present different behaviors with reference value setting increase. This inter-individual variability of brain responses along with an observed intra-individual SSVEPs variability through experimental trials (results not presented in this thesis) represent the need to study each individual independently, which adds complexity and time necessity to the control experimental trials fulfillment.

The validation results obtained for the models and the successful stabilization of models outputs massively supports the implementation of the designs exposed in this thesis for BCI experimental trials, to attempt the stabilization of EEG measured SSVEPs. There are still tests that may be advantageous to undertake. The system can be tested with EEG noise magnitudes to evaluate the resistance of the system to EEG background noise. Giving the SSVEPs elevated signal-to-noise ratio, it is expected that the system endures the noise addition. The simulations were successfully terminated. The experimental setup hardware & software designs necessary to validate the simulation results are justified.

Chapter 5:

BCI Prototype Framework

In this chapter, the *Matlab*™ systems design application to experimental setup for performing real-time experiments will be exposed. The experimental setup will comprise EEG equipment and visual stimulation screens. The BCI system is intended to be used in human experiments to evaluate system's responsiveness to the presence of real-time brain signals, measurement noise and physiological delays. Due to the time-length and complexity involved in performing such experiments, the procedures are intended to take place in future work, not being covered in this thesis.

5.1 Hardware & Software

The experimental setup is based on *Matlab*™ applications, namely *Simulink*™ for control system implementation; *Psychophysics Toolbox 3*™ (PTB3) to design and present visual stimulation on target screens; *Matlab*™ s-functions that extend capabilities of *Simulink*™ models by being compiled as MEX files and functioning as dynamically linked subroutines which can be automatically loaded and executed by *Matlab*™; UDP/TCPIP Ethernet communication protocols for *Matlab-Matlab* command; a *Thorlabs*™ SM1PD1A photodiode to have measurable signals from the stimulation screen and to evaluate the performance of the system by comparison of visual stimuli presentation; a LCD screen and a *gUSBamp SNR.: 2007.10.06* 16 channel (active electrodes) EEG amplifier from *g.Tec*™.

5.2 Experimental Setup

The designed approach consisted in two simultaneously running *Matlab*™ instances, connected through an Ethernet communication protocol. The first instance contains a control system *Simulink*™ model connected to the EEG output. The second instance runs PTB3, which generates and presents the visual stimulation in a LCD screen. After several failed attempts to real-time connect the *Matlab*™ instances, a UDP communication protocol was accomplished. The communication protocol purpose is to send system state information from the control model to the stimulation software. One of the challenges is the real time implementation of the communication procedure between two simultaneously running *Matlab*™ instances. As it is not known beforehand, if one computer can successfully run two communicating *Matlab*™ instances (mainly due to the PTB3 software), simulations will also be performed for two Ethernet communicating computers (see Figure 5.1).

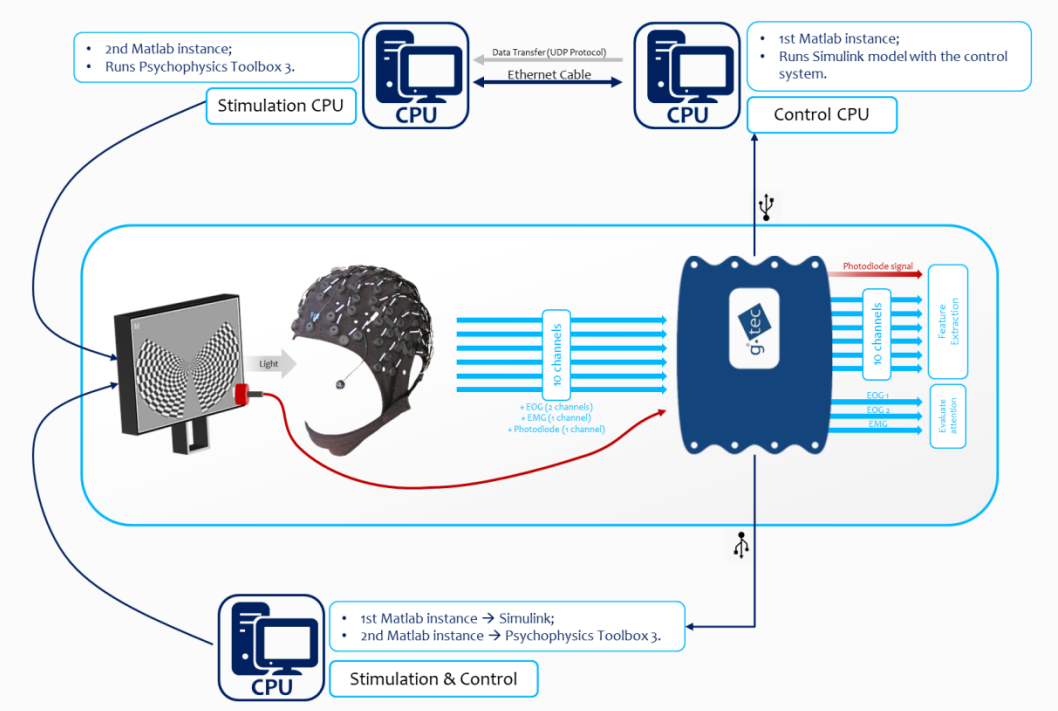

Figure 5.1) Experimental control system setup. Closed-loop real-time experimental setup schematic representation. Two approaches were successfully tested, both using two *Matlab*™ instances running simultaneously, one running PTB3 and the other running *Simulink*™. One approach uses a single computer for both instances and the other uses separated computers to run each instance.

The EEG amplifier is directly connected to the *Simulink*™ model via USB, so there are expected no EEG data transfer delays. All the blocks containing functions and calculation algorithms were compiled in one single level 2 *Matlab*™ s-function. S-functions are *Matlab*™ executable subroutines that can be automatically loaded and executed, simplifying the processes execution. The signal conditioning and processing is performed outside of the s-function, using the same blocks presented in Chapter 3 (see Figures 3.10 for FBF variable conditioning and Figure 3.34 for Linear Extrapolation variable conditioning).

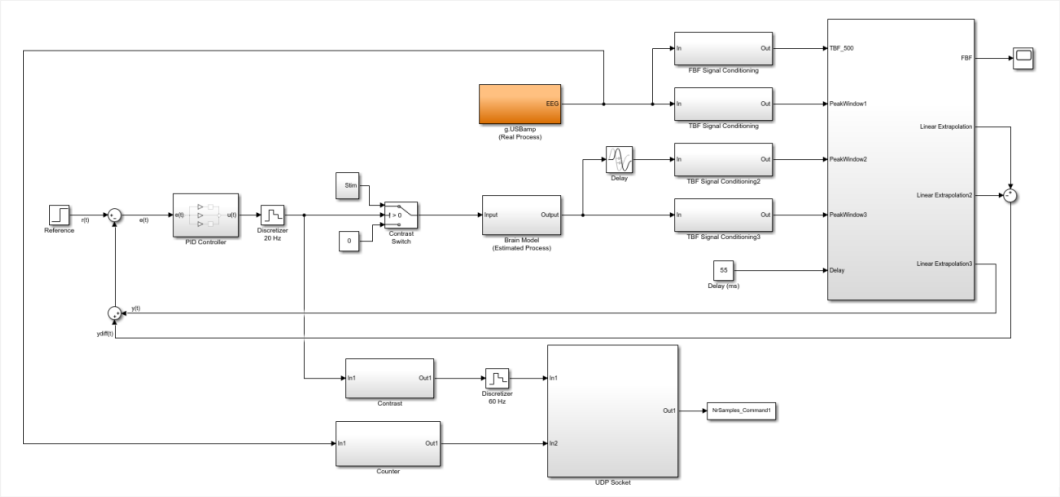

Figure 5.2) BCI experimental *Simulink*™ control model setup. This model differs from the simulations model in the inclusion of an EEG amplifier (*g.USBamp*), an s-function, a communication socket and EEG sample counters.

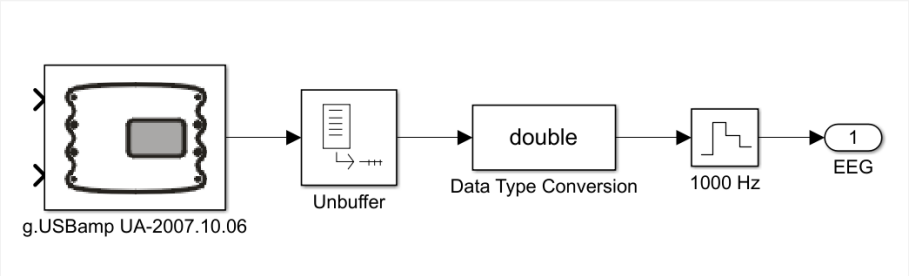

Figure 5.3) *g.USBamp Simulink*™ interface. Closer inspection at the *g.USBamp* block. This block contains an unbuffer block, a 'double type' data conversion block and a 1000 Hz discretizer due to the sampling rate of the amplifier (1200 Hz).

The experimental subject wears a 10 channel EEG cap, with all electrodes positioned in the most occipital are of the scalp. A LCD screen presents a system controlled onset & offset visual stimulation (see section *3.1.2.2) Full Calibration*), consisting of three alternating checkerboards (see Figure 3.3). Simultaneously, a stimulation signal is generated inside the *Simulink*™ model by the *contrast switch*.

The *contrast switch* generates the visual stimulation signal used as calculated brain SSVEP model input (see Figure 5.2). The EEG amplifier output is processed to extract the TBF variable (see section *3.1.2) Calibration Trials*) which possesses the interest features used in algorithm calculations. It is important to record the specific time moments at which each stimulation checkerboard is presented in the screen. This can be achieved by means of a photodiode attached to the screen lower right corner, which records a calibrated luminous signal accordingly to a specific defined square present in the lower inferior corner of the screen. The photodiode is directly connected to the *g.USBamp*, so the time stamp of the photodiode signal is in accordance with all the control system's signals. For the purpose of system analysis and performance measurements, a counting block is added to record the data measured volume in every onset stimulation, so it is possible to perfectly time and correct delays for all the involved variables. The counter and the *contrast* signal are used as input to the *UDP socket* block. This block connects with PTB3 *Matlab*™ instance, instructing and managing the stimulation software. The *g.USBamp* sampling rate is set to 1200 Hz, given the limited sampling rates available for this equipment (256 Hz, 600 Hz, 1200 Hz). All system components and calculations were designed aiming at a 1000 Hz EEG sampling rate, so a *discretizer* is included at the *g.USBamp* output to solve this issue (see Figure 5.3). For BCI experimental setup montage, see Appendix B.

5.3 Closed-Loop Testing

System testing is fundamental to evaluate efficiency, namely communication processes (correctly functioning and not influencing software processes), and the time delays present in the BCI system. Moreover, there is the need to evaluate if all control model components are compatible with the *g.USBamp* real-time acquisition and which (individual or dual CPU) approach is more suited. It is necessary to perform stimulation frames (checkerboards) construction. This is accomplished with *Matlab*™ code from *Soares et al* [15] experiences. Both the checkerboards and the PTB3 code are prepared for system implementation. A UDP client socket is

incorporated in the PTB3 code to receive commands from the S*imulink*™ control model. The tests don't include the use of an EEG cap, so calibrations aren´t needed for these. This means there is no EEG signal to perform feature extraction. To close the loop, the photodiode signal was used in the input designed for the EEG output, which enables to communication between control model and PTB3 software evaluation. In the estimated model's block is defined a simple oscillatory first order transfer function to minimize the influence of the process model during testing.

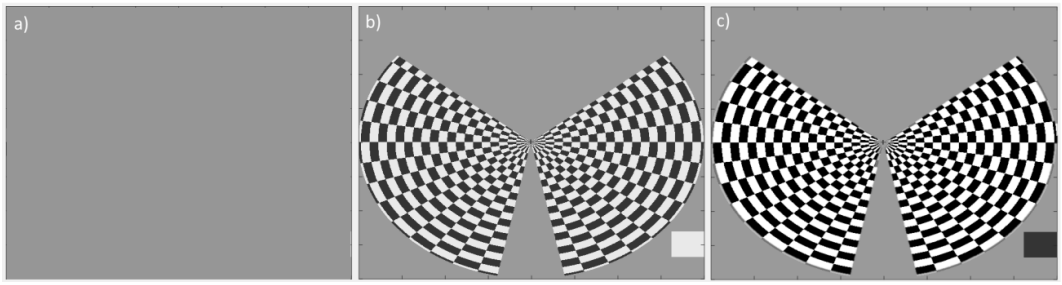

Figure 5.4) Visual stimulation frames. There are three stimulation screens/frames available for presentation: a) grey screen (frame B) presented for stimulation offset; b) first checkerboard (frame A), presented during one period of 16.67 ms for stimulation onset; second checkerboard (frame Ã), presented in two consecutive periods of 16.67 ms after frame A (see Figure 3.3 for stimulus description).

The *g.USBamp* manages the timing of the system, so all the signals recorded are coordinated in time (photodiode signal and the signals originated from the control model). The PTB3 is run first and waits for control model commands, which are sampled and sent at 60 Hz through the UDP socket. After testing it is possible to evaluate control model command generation and first frame presentation delays (timed by filtered photodiode signal's frame identifying peaks).

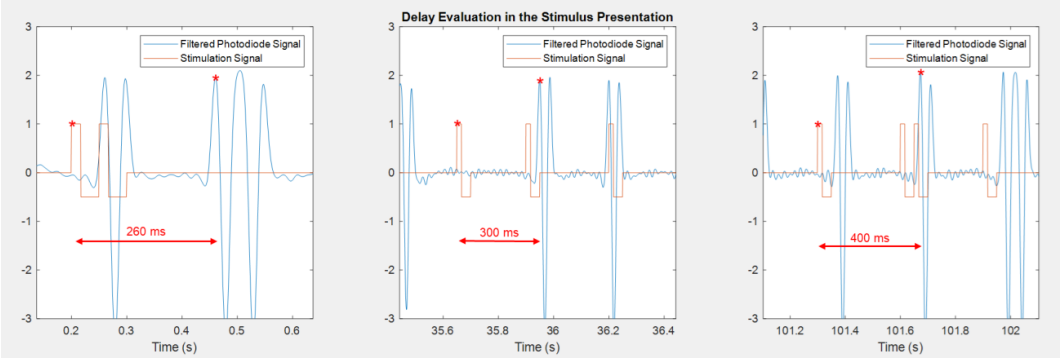

Figure 5.5) Experimental setup delay analysis results 1. Delays' evaluation through stimulation signal and photodiode signal time difference measurements (the first peak corresponds to the first frame onset). Results obtained for a 3 minute trial (180 seconds), using 1 computer running the two *Matlab*™ instances and a 0 ms LEADD.

After command and screen presentation delay successful evaluation, the first observation is that the photodiode montage is proven fundamental for system analysis. Secondly, the control system command generation and the screen stimulation onset & offset time differences (delays) increase throughout a single simulation session. In the simulation trial beginning, the delay is already problematic for experience purposes, measured at around 260 ms (see Figure 5.8). This means the screen is presenting the first frame 260 ms after the control command was generated. The same results were replicated for longer simulation courses and parameter variation like the linear extrapolation defined delay (LEADD), which showed no significant improvements in the delay results. The elevated initial delays and corresponding increase over the simulation course are believed to be strongly linked to the communication algorithm. The UDP protocol used to connect the two instances possesses a very simplistic code which could influence the PTB3 performance. To evaluate if the delays are due to the communication or to the presence of two instances running in the same computer, the same test was performed using two instances running in independent computers .

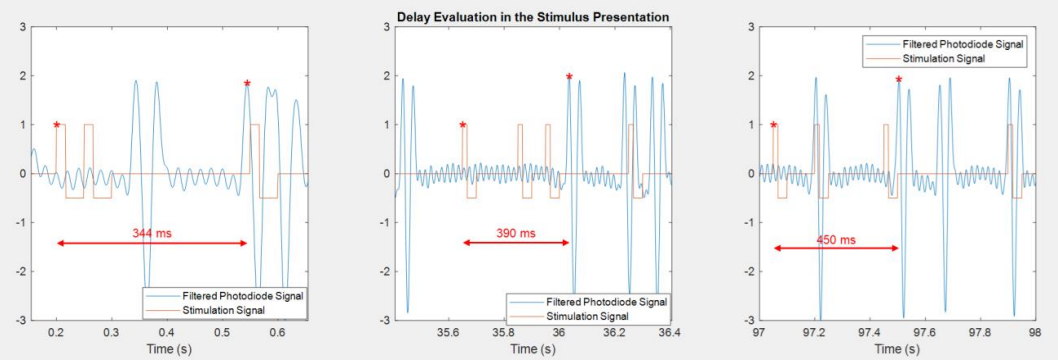

Figure 5.6) Experimental setup delay analysis results 2. Delays' evaluation through stimulation signal and photodiode signal time difference measurements (the first peak corresponds to the first frame onset). Results obtained for 3 minute trial (180 seconds), using 2 independent computers running each of the *Matlab*™ instances and a 0 ms LEADD.

The use of a two computer Ethernet cable connection only increases the delay. So the system functions by means of one computer running both *Matlab*™ instances, confirming that the two computer Ethernet connection ping increases the PTB3 command delay.

In the following figures (Figures 5.7 & 5.8) is shown the delay between each control command and frame presentation.

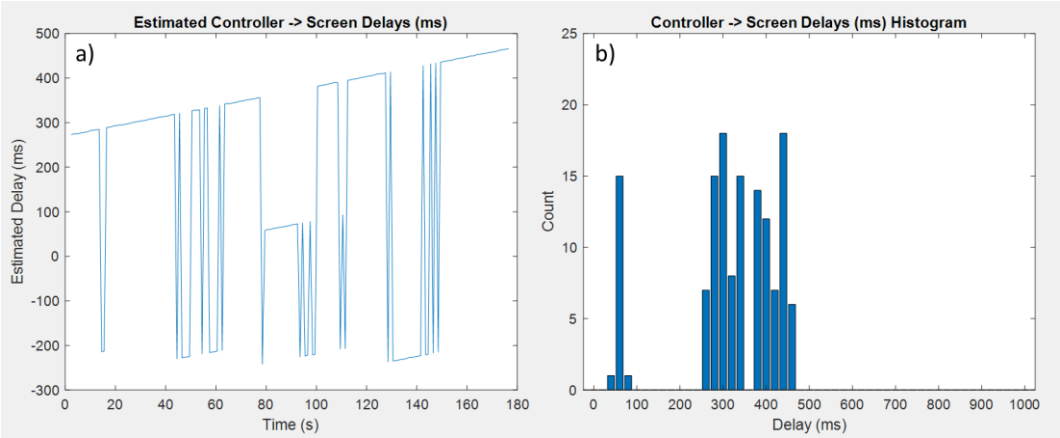

Figure 5.7) Experimental setup delay analysis results 3. These results refer to a 3 minute simulation using the two *Matlab*™ instances running in the same computer. The absolute delay values between control commands and frame presentation increases throughout single simulations (a). The absolute delay values magnitude is between 250 ms and 500 ms (b).

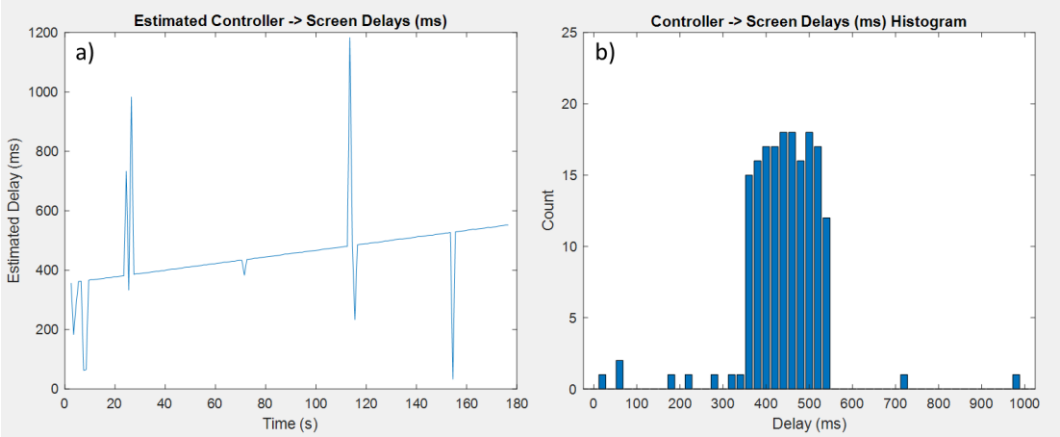

Figure 5.8) Experimental setup delay analysis results 4. These results refer to a 3 minute simulation using the two *Matlab*™ instances running in independent computers. The behavior is similar to the observed using only one computer (a). The absolute delay values magnitude is significantly higher (b), with delays between 300 ms and 550 ms.

The results support the delay increase phenomenon throughout individual simulations (see Figures 5.7a & 5.8a) and confirm that the control system and stimulation software can run simultaneously in the same computer with significantly better delay performance than with two computers. The hypothesis that the UDP connection is causing these massive delays is sustained by these findings. The most important elations taken from BCI experimental setup testing trials are: proof that the closed-loop works through communication of two *Matlab*™ instances; the photodiode montage allows a thorough system performance evaluation. In future

work, there is the need to improve the communication algorithm between the two running instances for delay reduction. The first frame peak identifier algorithm used is very advantageous to analyze system performance, automatically identify all the first frames corresponding peak in the photodiode signal and calculating the correspondent command delay. The algorithm must be adaptable to different experiments in order to identify the specific photodiode time stamps in which each frame was presented, facilitating analysis.

Chapter 6:

Conclusions & Future Work

Inducing dynamic changes in physiological brain potentials through non-invasive stimulation and recording techniques is clearly unpaved ground. Most rehabilitative BCI studies use invasive techniques (methods which enable precise stimulus delivery and recording), such as FES, to influence neuron activity in desired brain areas. Some of these efforts actually accomplished to induce intended and calculated activity alterations in specific brain areas (see section *2.4) State of the Art in Rehabilitative BCIs*). In contrast, the hypothesis of accomplishing neuronal activity manipulation using non-invasive methods both to record and stimulate presents several drawbacks, mainly the characteristic poor spatial resolution associated to EEG equipment. The lack of precise non-invasive technology to study the brain discourages researchers to pursuit solutions such as the ones we're trying to introduce. The advantage of using EEG equipment is the temporal resolution presented by this method. Some invasive methods can present better spatial resolution, but require more logistics to perform experiences and can present deficiencies in temporal resolution, which is fundamental for this approach. It is important to understand that the objective of this study is not to implement short-term rehabilitative solutions, given that even complex approaches cannot present palpable rehabilitative results. What is trying to be achieved is proof that, with resource non-invasive low-resolution equipment in a very simple experimental setup with elevated delay disturbances, it is possible to influence measured brain potentials in a controlled and calculated way. Till now, the hypothesis was only proven using brain SSVEP mathematical models, but a prototype system is almost set to observe system's performance in humans. There is still some work needed to accomplish the final objective, but the simulations results and the confirmation that the experimental

setup can perform real-time experiences are encouraging to pursue the proposed goal. The challenges are clear, overcome hardware delays, given the already prejudicial intrinsic physiological delays associated with SSVEP and consider EEG measurement noise. In case the brain models fail to perform in real time experiences, mathematical models improvements must be achieved, maybe through introduction of intra-individual specific variability. In this thesis case, given the highly satisfactory validation results, it is believed that even the simplistic models used can produce interesting results when placed in loop. The control model's prejudicial delay sensitivity brings the need to considerably reduce hardware delays, mainly in data and command transfer/transmission. In future work, a combination of brain signals recording methods would be advantageous to combine the temporal resolution capabilities of EEG with the spatial resolution capabilities of other methods. The spatial information would be important to relate the controlled power variables with the brain dynamics that originate them, since this relation cannot be observed with resource to EEG.

In conclusion, the objective of this thesis was clearly and unequivocally accomplished: stabilization of simulated brain SSVEP models to be used in BCI experiences. There is the need to evaluate if this SSVEP control can be accomplished in humans. The biological hypothesis presented in this thesis is proposed in light of evidences collected in reviewed literature. The hypothesis that relates the SSVEP potentials with synapse activation and synchronization is one of the many questions that still need to be answered when the subject is brain dynamics and signals. Nevertheless, the marginal control of brain signals is one unprecedented achievement, and can be put to the test with a system like the one presented on this document.

References

[1] C. Honey, R. Kotter, M. Breakspear and O. Sporns, "Network Structure of Cerebral Cortex Shapes functional connectivity on multiple time scales", 2007.

[2] P. Hagmann, L. Cammoun, X. Gigandet, R. Meuli, C. Honey, V. Wedeen and O. Sporns, "Mapping the structural core of human cerebral cortex", 2008.

[3] C. Honey, O. Sporns, L. Cammoun, X. Gigandet, J. Thiran, R. Meuli and P. Hagmann, "Predicting human resting-state functional connectivity from structural connectivity", 2009.

[4] M. Rubinov, O. Sporns, C. van Leeuwen and M. Breakspear, "Symbiotic relationship between brain structure and dynamics", 2009.

[5] C. Honey, J. Thivierge and O. Sporns, "Can structure predict function in the human brain?", 2010.

[6] J. Fell and N. Axmacher, "The role of phase synchronization in memory process - A review", 2011.

[7] E. Roelfsema, "Perception's shadow, long-distance synchronization of human brain activity", 1999.

[8] J. Cavanagh, M. Cohen and J. Allen, "Prelude to and resolution of an error, EEG phase synchrony reveals cognitive control dynamics during action monitoring", 2009.

[9] A. Schnitzler and J. Gross, "Normal and Pathological Oscillatory Communication in the Brain", 2005.

[10] I. Timofeev and M. Steriade, "Neocortical seizures: initiation, development and cessation", 2004.

[11] R. Traub, "Fast oscillations and epilepsy", 2003.

[12] O. vanderStelt, A. Belger and J. Lieberman, "Macroscopic fast neuronal oscillations and synchrony in schizophrenia", 2004.

[13] J. Jeong, "EEG dynamics in patients with Alzheimer's", 2004.

[14] W. Hutchison, "Neuronal oscillations in the basal ganglia and movement disorders: evidence from whole animal and human recordings", 2004.

[15] E. Soares, Research in SSVEP, 2015.

[16] G. Fishman, D. Birch, G. Holder and M. Brigell, "Electrophysiologic Testing in Disorders of the Retina, Optic Nerve and Visual Pathway", 2001.

[17] D. Hood, J. Odel and B. Winn, "The Multifocal Visual Evoked Potential", 2003.

[18] N. Birbaumer, "Breaking the Silence: Brain-Computer Interfaces (BCI) for Communication and Motor Control", 2005.

[19] A. Fedotchev, S. Parin, S. Polevaya and S. Velikova, "Brain-Computer Interface and Neurofeedback Technologies: Current State, Problems and Clinical Prospects (Review)", 2016.

[20] J. Mak and J. Wolpaw, "Clinical Applications of Brain-Computer Interfaces: Current State and Future Prospects", 2009.

[21] A. Rezeika, M. Benda, P. Stawicki, F. Gembler, A. Saboor and I. Volosyak, "Brain-Computer Interface Spellers: A Review", 2018.

[22] I. Volosyak, H. Cecotti, D. Valbuena and A. Graser, "Evaluation of the Bremen SSVEP based BCI in real world conditions", 2009.

[23] A. Jackson and J. Zimmermann, "Neural interfaces for the brain and spinal cord - restoring motor function", 2012.

[24] D. Guggenmos, M. Azin, S. Barbay, J. Mahnkend, C. Dunham, P. Mohseni and R. Nudo, "Restoration of function after brain damage using a neural prosthesis", 2013.

[25] M. Krucoff, S. Rahimpour, M. Slutzky, V. Edgerton and D. Turner, "Enhancing Nervous System Recovery Throught Neurobiologics, Neural Interface Training and Neurorehabilitation", 2016.

[26] P. Rutecki, "Neuronal excitability: voltage-dependent currents and synaptic transmission", 1992.

[27] A. Hodgkin and A. Huxley, "A quantitative description of membrane current and its application to conduction and excitation in nerve", 1952.

[28] D. Purves, "Neuroscience" (5th Edition), 2011.

[29] S. Sur and V. Sinha, "Event-related potential: An overview", 2009.

[30] A. Capilla, P. Alvarez, A. Darriba, P. Campo and J. Gross, "SSVEP can be explained by Temporal Superposition of Transient ERP", 2011.

[31] S. Simrock, "Control Theory".

[32] G. Buzsáki, "Rhythms of the Brain", Oxford University Press, 2006.

[33] H. Haken, "Principles of brain functioning", 1996.

[34] P. Nunez and R. Srinivasan, "Electric fields of the brain: The neurophysics of EEG", Oxford University Press, 1981.

[35] X. Wang, "Neurophysiological and Computational Principles of Cortical Rhythms in Cognition", 2010.

[36] J. Cardin, M. Carlen, K. Meletis, U. Knoblich, F. Zhang, K. Deisseroth, L. Tsai and C. Moore, "Driving fast-spiking cells induces gamma rhythm and controls sensory responses", Nature, 2009.

[37] F. Vialatte, M. Maurice, J. Dauwels and A. Cichocki, "Steady-state visually evoked potentials: Focus on essential paradigms and future perspectives", 2010.

[38] K. Ramó and C. Verdecia, "What We Know About the Brain Structure-Function Relationship", 2018.

[39] C. Ethier, J. Gallego and L. Miller, "Brain-Controlled Neuromuscular Stimulation to Drive Neural Plasticity and Functional Recovery", 2015.

[40] D. Hebb, "The Organization of Behavior", 1949.

[41] E. Bienenstock, L. Cooper and P. Munro, "Theory for the Development of Neuron Selectivity: Orientation specificity and binocular interaction in visual cortex", 1982.

[42] P. Rossini, M. Ferilli and F. Ferreri, "Cortical plasticity and brain computer interface", 2012.

[43] M. Rioult-Pedotti, J. Donghue and A. Dunaevsky, "Plasticity of the synaptic modification range, 2007.

[44] V. Dietz and K. Fouad, "Restoration of Sensorimotor Functions After Spinal Cord Injury", Oxford University Press, 2013.

[45] T. Murphy and D. Corbett, "Plasticity during stroke recovery: from synapse to behaviour", 2009.

[46] G. Pfurtscheller and A. Aranibar, "Event-related cortical desynchronization detected by power measurements of scalp EEG", 1977.

[47] J. Carmena, M. Lebedev, R. Crist, J. O'Doherty, D. Santucci and D. Dimitrov, "Learning to control a brain-machine interface for reaching and grasping by primates", 2003.

[48] N. Fitzsimmons, M. Lebedev, I. Peikon and M. Nicolelis, "Extracting kinematic parameters for monkey bipedal walking from cortical neuronal ensemble activity", 2009.

[49] M. Nicolelis and M. Lebedev, "Principles of neural ensemble physiology underlying the operation of brain-machine interfaces", 2009.

[50] P. Konig, A. Engel and W. Singer, "Integrator or coincidence detector? The role of the cortical neuron", 1996.

[51] J. Lachaux, E. Rodriguez and J. Martinerie, "The brainweb: phase synchronization and large scale integration", 2001.

[52] J. Gross, "Modulation of long-range neural synchrony reflects temporal limitations of visual attention in humans", 2004.

[53] P. Brown, "Oscillatory nature of human basal ganglia activity: relationship to the pathophysiology of Parkinson's disease", 2003.

[54] W. Abraham, O. Jones and D. Glanzman, "Is plasticity of synapses the mechanism of long-term memory storage?", 2019.

[55] J. Rebesco, I. Tevenson, K. Kording, S. Solla and L. Miller, "Rewiring neural interactions by micro-stimulation", 2010.

[56] A. Guyton and J. Hall, "Guyton and Hall Textbook of Medical Physiology 11th Edition", 2006.

[57] A. Cotrina, "Toward Brain Computer Interaction in Paralysis - Chapter 2: Fundamentals: From Light to Command", 2017.

[58] J. Cudeiro and A. Sillito, "Looking back: corticothalamic feedback and early visual processing", 2006.

[59] A. Biasiucci, B. Franceschiello and M. Murray, "Electro-encephalography", 2019.

[60] G. Pires, M. Castelo-Branco and U. Nunes, "Visual P3000-based BCI to steer a Wheelchair: a Bayesian Approach", 2008.

[61] G. Pfurtscheller, C. Guger, G. Muller, G. Krausz and C. Neuper, "Brain oscillations control hand orthosis in a tetraplegic", 2000.

[62] F. Cincotti, D. Mattia, F. Aloise, S. Bufalari, G. Schalk, G. Oriolo, M. Cherubini, G. Marciani and F. Babiloni, "Non-invasive brain-computer interface system: Towards its application as assistive technology", 2008.

[63] J. Odom, M. Bach, C. Barber, M. Brigell, M. Marmor, A. Tormene, G. Holder and Vaegan, "Visual evoked potentials standard", 2004.

[64] A. Norcia, L. Appelbaum, J. Ales, B. Cottereau and B. Rossion, "The steady-state visual evoked potential in vision research: A review", 2015.

[65] S. Morgan, J. Hansen and S. Hillyard, "Selective attention to stimulus location modulates the steady-state visual evoked potential", 1996.

[66] K. Ellis, R. Silberstein and P. Nathan, "Exploring the temporal dynamics of the spatial working memory n-back task using steady state visual evoked potentials (SSVEP)", 2006.

[67] M. Wieser, V. Miskovic and A. Keil, "Steady-state visual evoked potentials as a research tool in social affective neuroscience", 2016.

[68] L. Ljung, "System Identification Toolbox: User's Guide", 2015.

[69] A. Coelho, R. Araújo, D. Jeronymo and C. Suarez, "Discrete Smith Predictor Design and Performance Improvement of PID Tuning", 2015.

[70] MathWorks Documentation: "https://www.mathworks.com/help/control/examples/control-of-processes-with-long-dead-time-the-smith-predictor.html".

[71] A. Gharabaghi, D. Kraus, M. Leão, M. Spuler, A. Walter, M. Bogdan, W. Rosenstiel, G. Naros and U. Ziemann, "Coupling brain-machine interfaces with cortical stimulation for brain-state dependent stimulation: enhancing motor

cortex excitability for neurorehabilitation", 2014.

[72] C. Moritz, S. Perlmutter and E. Fetz, "Direct control of paralysed muscles by cortical neurons", 2008.

[73] E. Pohlmeyer, E. Oby, E. Perreault, A. Solla, K. Kilgore, R. Kirsch and L. Miller, "Toward the restoration of hand use to a paralysed monkey: brain-controlled functional electrical stimulation of forearm muscles", 2009.

[74] G. Garcia-Molina, T. Tsoneva, J. Jasko, B. Steele, A. Aquino, K. Baher, S. Pastoor, S. Pfundtner, L. Ostrowski, B. Miller, N. Papas, B. Riedner, G. Tononi and D. White, "Closed-loop system to enhance slow wave activity during sleep", 2018.

[75] W. Hardle and L. Simar, "Canonical Correlation Analysis", 2007.

[76] A. Ben-Israel and T. Greville, "Generalized inverses: theory and applications", 2003.

Appendices

A

Database description

The database used in this thesis (referring to the reasearch of *Soares et al* [15]):

- Contains 10 experimental subjects, each one performing 6 data acquisition trials;
- Contemplated data from 64 channel EEG equipment from *Brain Products*™;
- The 20 electrodes used (Figure 1) were acquired at 1 kHz, hardware-filtered between 0.1-250 Hz;
- All the signals are normalized so there are no units associated with the EEG signals in the database;
- The database also contemplates calibration trials.

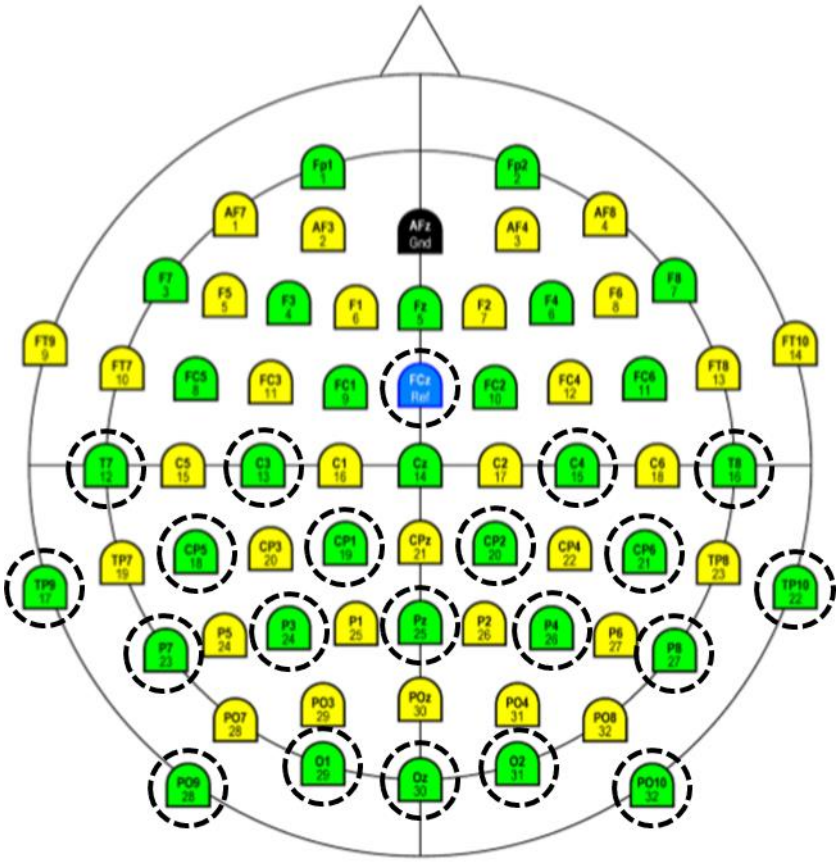

Appendix A Figure 1) *actiCap* 64Ch Standard-2 electrodes used in the data recording of the database [15].

B

Magnitude comparison of different experimental trials estimated models response

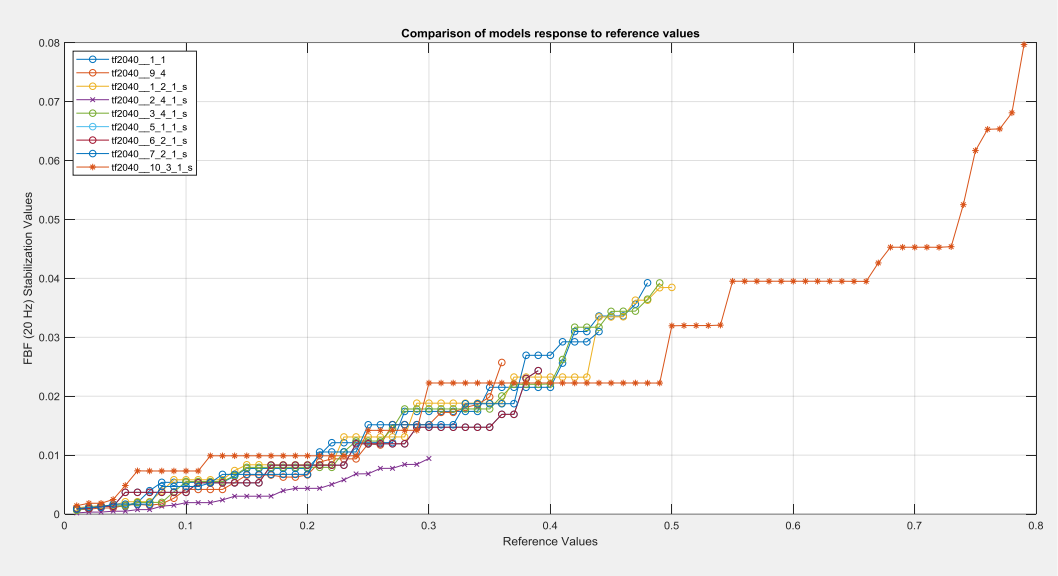

Appendix B Figure 1) Magnitude comparison of different model's FBF stabilization responses with the reference value increase (0.01 between simulations and LEADD= 55 ms).

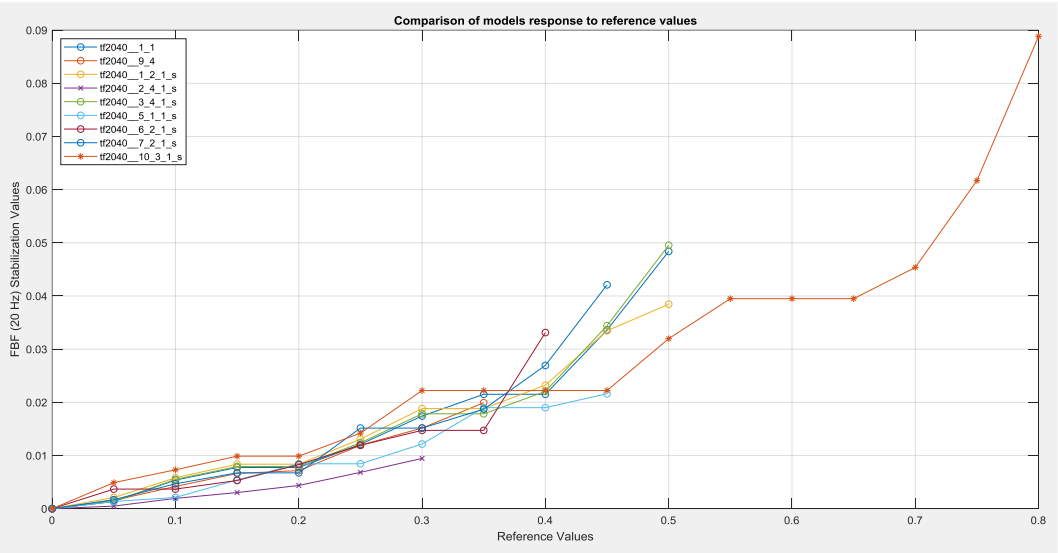

Appendix B Figure 2 **Departamento de Física**) Magnitude comparison of different model's FBF stabilization responses with the reference value increase (0.05 between simulations and LEADD= 55 ms). Given that in this graphic the reference value increase between simulations is 0.05, some of the values present may be related to model's saturation steps.

C

BCI experimental setup montage

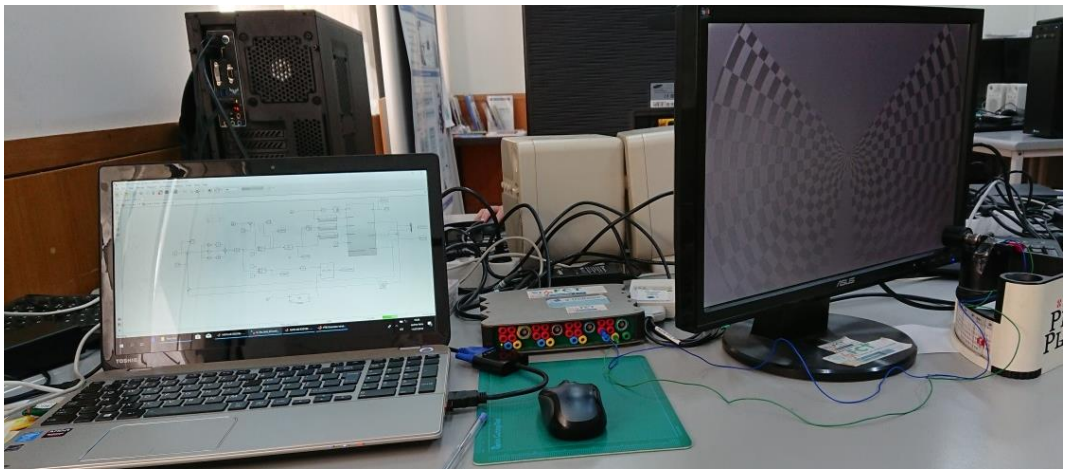

Appendix C Figure 1) System montage using one computer running both *Matlab*™ instances. The photodiode is placed on the lower right corner of the screen, coinciding with a frame identifying square imbued in each stimulation frame.

Appendix C Figure 2) System montage using two computers, each running one *Matlab*™ instance. The computers are connected through an Ethernet cable with an associated data transfer ping (in the millisecond scale).

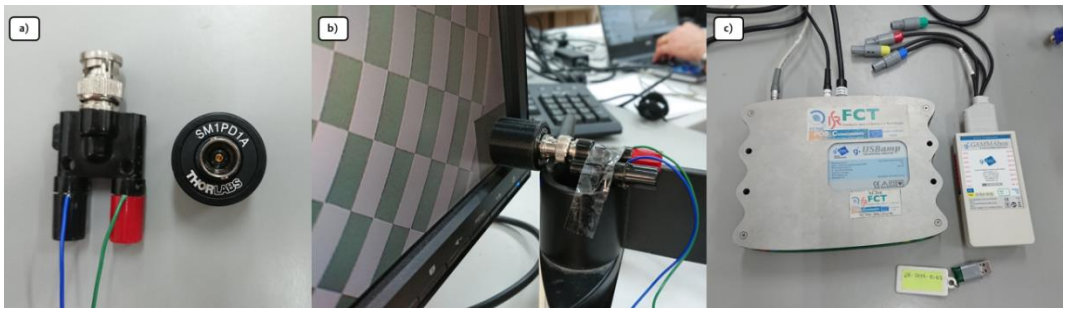

Appendix C Figure 3) Designed system components. a) Photodiode and respective connector cables, enabling *g.USBamp* direct connection; b) Photodiode montage on the screen; c) *g.USBamp* EEG amplifier device, connects to the EEG cap, photodiode and control model.